UC Riverside

UC Riverside Electronic Theses and Dissertations

Title

Investigations of Model Simulations and Satellite Observations for Better Understanding of Climate Change Impacts and Aerosol Processes

Permalink

https://escholarship.org/uc/item/6800p4kp

Author

Park, Sunmin

Publication Date

2017

Peer reviewed|Thesis/dissertation

eScholarship.org Powered by the California Digital Library
University of California

UNIVERSITY OF CALIFORNIA
RIVERSIDE

Investigations of Model Simulations and Satellite Observations for Better Understanding of Climate Change Impacts and Aerosol Processes

A Dissertation submitted in partial satisfaction
of the requirements for the degree of

Doctor of Philosophy

in

Geological Sciences

by

Sunmin Park

December 2017

Dissertation Committee:
Dr. Robert J. Allen, Chairperson
Dr. Richard A. Minnich
Dr. Roya Bahreini

Copyright by
Sunmin Park
2017

The Dissertation of Sunmin Park is approved:

Committee Chairperson

University of California, Riverside

ACKNOWLEDGEMENT

First of all, I would like to thank my adviser Dr. Robert J. Allen, for all of his support and guidance. I do appreciate that you are patient with me and always supportive whenever I face problems related to work. I have learned many things since starting from scratch. Without your support and patience, I would be unable to conduct all the work I have done for my research. I would also like to express my gratitude to Dr. Richard A. Minnich and Dr. Roya Bahreini for all of their advice on my work and mental support.

To the many people who I have met during my Ph.D journey, I appreciate all of your support. To Yenny Lay, I do appreciate you for being with me all the time and supportive when I had a hard time with whatever it was. To Bridget Lee, I thank you for giving me good advice and positive energy all the time. I also would like to thank all my lab members and people in Earth Science Department.

To my baby doggies Kongg, Kuko, and Kongja, I am sure that I couldn't have finished this long five-year journey without you three lovely children. Finally, to my mother, you know how much I appreciate your support and all the love that you have for me. Dad, I know you are always watching me from heaven. I miss you so much. Love you all. Thank you.

To beloved parents Yangsoon Oh and Dongryul Park.

To my lovely babies, Kongg, Kuko, and Kongja.

The work in this dissertation entirely or in part from the following publications:

Park, S., and Allen, R. J. (2015). Understanding influences of convective transport and removal processes on aerosol vertical distribution. Geophysical Research Letters, 42(23).

ABSTRACT OF THE DISSERTATION

Investigations of Model Simulations and Satellite Observations for Better Understanding of Climate Change Impacts and Aerosol Processes

by

Sunmin Park

Doctor of Philosophy, Graduate Program in Geological Sciences
University of California, Riverside, December 2017
Dr. Robert J. Allen, Chairperson

This dissertation focuses on three subjects related to aerosol vertical profile, future climate change impacts on surface aerosol concentration and its effects on premature mortality and drought risk over California (CA). In Chapter 1, I investigate how convective mass flux and precipitation (wet removal) are associated with the aerosol vertical profile over the globe using Cloud-Aerosol Lidar Infrared Pathfinder Satellite Observation (CALIPSO), Modern-Era Retrospective Analysis for Research and Applications (MERRA), European Centre for Medium-Range Weather Forecasts Interim Re-Analysis (ERA-Interim) and Global Precipitation Climatology Project (GPCP). The results indicate that convective mass flux is an important mechanism that influences global aerosol vertical distribution. In the tropics, more convective mass flux is associated with more aerosol above 500 hPa while less aerosol is related to less

convective mass flux. More convective mass flux over the Northern Hemisphere mid-latitude emission sources is associated with more aerosol aloft (downwind). More (less) downward CMF is associated with more (less) aerosol in the lower troposphere and less (more) aerosol in the upper troposphere and vertical dispersivity over NH Pacific.

In Chapter 2, the response of surface fine particulate matter ($PM_{2.5}$) concentration to greenhouse gas (GHG) induced warming at the end of century, and its effects on premature mortality related to respiratory diseases, is estimated. To conduct this work I use simulated $PM_{2.5}$ from seven Atmospheric Chemistry and Climate Model Intercomparison Project (ACCMIP) models and five projected populations by Shared Socioeconomic Pathways (SSPs). Future climate change has a significant impact on surface $PM_{2.5}$ concentration and the corresponding premature mortality. Both surface $PM_{2.5}$ and premature mortality will likely increase at end of the 21st century under business-as-usual warming.

In Chapter 3, I investigate future drought risk over California using the Community Earth System Model Large Ensemble Community Project (CESM-LENS). This model is used because 1. it captures the observed teleconnection between El-Nino and California (CA) precipitation and 2. allows an assessment of the role of natural climate variability. The results suggest that under business-as-usual GHG emissions, drought risk during the 21st century does not significantly increase.

Table of Contents

Chapter 1 Understanding influences of convective transport and removal processes on aerosol vertical distribution 1
1.1 Introduction 2
1.2 Data and Methods 4
1.3 Results 11
References 30

Chapter 2 A likely increase in fine particulate matter and premature mortality under future climate change 34
2.1 Introduction 35
2.2 Methods 37
2.3. Results 47
2.3.1 Changes in surface $PM_{2.5}$ concentration 47
2.3.2 Effects of $PM_{2.5}$ changes on premature mortality 59
References 79

Chapter 3 Investigation of future changes in drought risk over California under a business-as-usual scenario 82
3.1 Introduction 83
3.2 Data and Methods 85
3.3 Results 86
References 94

Chapter 4 Conclusion 97
4.1. Chapter 1: Understanding influences of convective transport and removal processes on aerosol vertical distribution 97
4.2 Chapter 2: A likely increase in fine particulate matter and premature mortality under future climate change 98
4.3 Chapter 3: Investigation of future changes in drought risk over California under a business-as-usual scenario 99
References 102

Chapter 5 Future Work 103
References 108

List of Figures

Figure 1.1 Spatial map of the climatology (7 year average) of CALIPSO level 3 a) aerosol extinction coefficient; b) aerosol vertical dispersivity; and c) average extinction coefficient above 500 hPa. MERRA net CMF from the two boxes in panel a is used to calculate the north Pacific (Figure 1.8) and Atlantic (Figure 1.9) correlations…….. 6

Figure 1.2 Spatial maps of the climatology (7 year average) of a) MERRA net convective mass flux (CMF); b) ERA-Interim net CMF; c) ERA-Interim upward CMF; d) ERA-Interim downward CMF. e) Spatial map of the linear cross correlation between ERA-Interim upwards and downwards CMF. Symbols represent significance at the 95% confidence level. Unit of CMF are kg m^{-2} s^{-1}. Note that a larger downward CMF in ERA-Interim is represented by a larger negative number. …….. 9

Figure 1.3 Spatial map of the linear cross correlation between a) MERRA net CMF and GPCP precipitation; and b) ERA-Interim net CMF and GPCP precipitation. Corresponding correlation of the zonal mean time series between c) MERRA net CMF and GPCP precipitation; and d) ERA-Interim net CMF and GPCP precipitation. Symbols represent significance at the 95% confidence level. …….. 12

Figure 1.4 Spatial maps of the linear cross correlation between aerosol vertical dispersivity, and (a) MERRA net CMF and (b) GPCP precipitation. Corresponding correlation of the zonal mean time series between aerosol vertical dispersivity, and (c) MERRA net CMF and (d) GPCP precipitation. Symbols represent significance at the 95% confidence level. …….. 13

Figure 1.5 Spatial maps of the linear cross correlation between ERA-Interim net CMF and (a) aerosol vertical dispersivity, (b) average extinction coefficient below 500 hPa, and (c) average extinction coefficient greater than or equal to 500 hPa. Symbols represent significance at the 95% confidence level. …….. 15

Figure 1.6 Spatial maps of the linear cross correlation between average extinction coefficient below 500 hPa, and (a) MERRA net CMF and (b) GPCP precipitation. Corresponding correlation of the zonal mean time series between average extinction coefficient below 500 hPa, and (c) MERRA net CMF and (d) GPCP precipitation. Symbols represent significance at the 95% confidence level…… 17

Figure 1.7 Spatial maps of the linear cross correlation between average extinction coefficient greater than or equal to 500 hPa, and (a) MERRA net CMF and (b) GPCP precipitation. Corresponding correlation of the zonal mean time series between average extinction coefficient greater than or equal to 500 hPa, and (c) MERRA net CMF and (d) GPCP precipitation. Symbols represent significance at the 95% confidence level. …….. 19

Figure 1.8 North Pacific spatial maps of the linear cross correlation between aerosol vertical dispersivity and (a) MERRA net CMF, (b) GPCP precipitation over identical grid boxes, and between aerosol vertical dispersivity over the north Pacific and (c) MERRA net CMF, (d) GPCP precipitation over SE Asia (103.9° to 119.1°E, 22.2° to 38.4°N). Symbols represent significance at the 95% confidence level. …….. 22

Figure 1.9 North Atlantic spatial maps of the linear cross correlation between aerosol vertical dispersivity and (a) MERRA net CMF, and (b) GPCP precipitation over identical grid boxes, and between aerosol vertical dispersivity over the north Atlantic and (c) MERRA net CMF, and (d) GPCP precipitation over the eastern United States (-93.8° to -78.6°E, 30.3° to 44.5°N). Symbols represent significance at the 95% confidence level. ……..24

Figure 1.10 Spatial maps of the linear cross correlation between ERA-Interim downward CMF and a) aerosol vertical dispersivity, (b) average extinction coefficient below 500hPa, (c) average extinction coefficient greater than or equal to 500 hPa; and ERA-Interim upward CMF and (d) aerosol vertical dispersivity, (e) average extinction coefficient below 500hPa, (f) average extinction coefficient greater than or equal to 500 hPa. Symbols represent significance at the 95% confidence level. Stronger upward CMF is a larger positive number, but a stronger downward CMF is a larger negative number. Thus, a positive correlation between downward CMF and dispersivity means stronger downdrafts are associated with less dispersivity, and vice versa. …… 28

Figure 2.1 Spatial distribution of exposed population age 30 and above for the year 2100 from the SSP5 population scenario (units: people/km^2). The other SSPs yield similar spatial patterns, but with different magnitudes (Table 2.2). 41

Figure 2.2 Spatial maps of differences in population age 30 and over between present-day (the year 2014) and projected future population using a) SSP1, b) SSP2, c) SSP3, d) SSP4, and e) SSP5 (units: people/km^2). 45

Figure 2.3 Annual mean $PM_{2.5}$ surface concentration change (units: μg/m^3) between 2100 and 2000 from a) GFDL-AM3, b) MIROC-CHEM, c) GISS-E2-R, d) NCAR-CAM3.5, e) HadGEM2, f) CAM4, and g) CAM5..... 51

Figure 2.4 Number of models that yield elevated annual mean $PM_{2.5}$ concentration over the continents at the end of the 21st century..... 52

Figure 2.5 Number of ACCMIP models that agree on an increase in $PM_{2.5}$ at end of the 21st century with a) $PM_{2.5}$ approximated as the sum of six species (Eq. [1] from the manuscript), b) archived $PM_{2.5}$ and c) the difference between the sum of six species and archived $PM_{2.5}$ (a - b). Defining $PM_{2.5}$ as the sum of six species yields larger model agreement on an increase in $PM_{2.5}$ in several regions, including North America and Europe..... 55

Figure 2.6 The $PM_{2.5}$ response difference ($DPM_{2.5}$ estimated as the sum of species minus actual $DPM_{2.5}$) for a) GFDL-AM3, b) MIROC-CHEM, c) GISS-E2-R, d) NCAR-CAM3.5, e) CAM4, and f) CAM5. GFDL-AM3 and GISS-E2-R are based on 8 species (BC + OA + SO_4 + SOA + 0.25*SS + 0.1*Dust + NO_3 + NH_4); the other models are based on 6 species (no NO_3/NH_4), except CAM4 which is based on 5 species (no NO_3/NH_4/SOA). For each model, approximating $PM_{2.5}$ as the sum of species yields discrepancies in the $PM_{2.5}$ response, relative to actual $PM_{2.5}$, in most regions. HadGEM2 results are not shown, since archived $PM_{2.5}$ does not exist for this model. 58

Figure 2.7 Number of models that yield an increase in premature mortality at the end of the 21st century (SSP5 scenario) 60

Figure 2.8 Annual premature mortality (SSP5 scenario) due to both LC and CPD in the year 2100 due to changes in $PM_{2.5}$ concentration from a) GFDL-AM3, b) MIROC-CHEM, c) GISS-E2-R, d) NCAR-CAM3.5, e) HadGEM2, f) CAM4, and g) CAM5 (units: deaths/10000 km^2). The other SSPs yield a similar spatial mortality distribution, but with different magnitudes (Table 2.4 and 2.5). White land areas indicate no exposed population…… 65

Figure 2.9 Global premature mortality based on future projected population (SSPs) by seven models. …… 67

Figure 2.10 Premature mortality based on future projected population (SSPs) over 10 world regions from a) GFDL-AM3, b) MIROC-CHEM, c) GISS-E2-R, d) NCAR-CAM3.5, e) HadGEM2, f) CAM4, and g) CAM5…….. 71

Figure 3.1 CESM-LENS 21st century (2006-2100) ensemble mean annual mean trend of a) precipitation, b) surface water availability (P-E), c) runoff, d) shallow soil moisture, and e) deep soil moisture. Units for precipitation, P-E and runoff is mm $day^{-1}century^{-1}$ and mm $century^{-1}$ for soil moisture. Red (Blue) colors indicates a positive (negative) trend. Boxes over CA represent three sub-regions: southern, central, and northern. Symbols represent trend significance at 95% confidence level…….. 89

Figure 3.2 The number of CESM-LENS 21st century realizations that yield an increase (red) or decrease (blue) in annual mean a) precipitation, b) surface water availability (P-E), c) runoff, d) shallow soil moisture, and e) deep soil moisture……..... 91

Figure 3.3 Estimated California drought risk (%) based on precipitation (PRE), surface water availability (P-E), Runoff, shallow soil moisture (SOIL-shallow) and deep soil moisture (SOIL-Deep). Blue and red colored bars represent the 20 and 21st century, respectively. …….. 92

Figure 5.1 Global mean vertical profiles of extinction coefficient from CALIPSO (black) versus eight GCMs. GCMs include CAM5 (dashed red), GEOSCAM5 (dashed yellow), MERRACAM5 (dashed orange), MIROC5 (dashed green), MIROC5_ESM_CHEM (dashed dark blue), MIROC5_ESM (dashed blue), NorESM1-M (dashed purple), and NorESM1-ME (dashed pink). …… 104

List of Tables

Table 2.1 Models used in this study. The first five model simulations come from ACCMIP; the last two model simulations (CAM4/5) were performed by the authors. Also included is the number of simulation years available for each experiment, the horizontal and vertical resolutions, and the corresponding reference. In most models, $PM_{2.5}$ is based on six species, including black carbon, organic aerosol, sulfate, secondary organic aerosol, sea salt, and dust. However, in CAM4, no secondary organic aerosol is included, so $PM_{2.5}$ is based on five species; in GFDL-AM3 and GISS-E2-R, ammonium sulfate and nitrate are also included, so $PM_{2.5}$ is based on eight species. This implies differences in the composition of $PM_{2.5}$ across some models. Nonetheless, I prefer to focus on actual $PM_{2.5}$, as opposed to the alternative approach whereby $PM_{2.5}$ is approximated by Eq. [1] from the manuscript. I find that this approximation can affect the $PM_{2.5}$ response, and the corresponding model agreement (Figure 2.5 and 2.6). 39

Table 2.2 Future population estimates age 30 and above for the five SSPs in 10 world regions (units: billions of people). The ten world regions are identical to those in Figure S5 from Silva *et al.* [2013]. The mean value column represents the average across the five scenarios..... 43

Table 2.3 Annual mean changes in surface $PM_{2.5}$ concentration ($\mu g/m^3$) by region and model..... 48

Table 2.4 Annual mean premature mortality (deaths/10000 km^2) for both lung cancer (LC) and cardiopulmonary disease (CPD) by region, model, and future-population scenario. Over Australia, <1 indicates a small increase in premature mortality (0 < deaths/10000 km^2 < 1) and <0 indicates a small decrease in premature mortality (-1 < deaths/10000 km^2 < 0) 61

Table 2.5 Total, minimum, and maximum premature mortality (deaths/year) for both lung cancer (LC) and cardiopulmonary diseases (CPD) for a) GFDL-AM3, b) MIROC-CHEM, c) GISS-E2-R, d) NCAR-CAM3.5, e) HadGEM2, f) CAM4, and g) CAM5 by ten regions and five future-population scenarios (SSPs). 72

Table 3.1 Estimated California drought risk (%) in the 20 and 21st century and differences (21st century minus 20th century) between the two centuries. Bold numbers represent significant changes at the 95% confidence level. 93

Chapter 1 Understanding influences of convective transport and removal processes on aerosol vertical distribution

Abstract

The vertical distribution of aerosols is an important component of aerosol radiative forcing. Here, I investigate the effects of convection transport and precipitation on the vertical aerosol distribution using observations and reanalysis data. As expected, convective mass flux is positively correlated with precipitation everywhere. Both positive and negative correlations between convective mass flux, precipitation, and aerosol vertical dispersivity exist, depending on the region. In the tropics, more (less) convective mass flux is associated with more (less) precipitation and more (less) aerosol vertical dispersivity—including more (less) aerosol above 500 hPa. In contrast, a negative relationship exists between aerosol vertical dispersivity and both convective mass flux and precipitation over the Northern Hemisphere mid-latitude ocean. Aerosol vertical dispersivity in this region is related to convective mass flux and precipitation over the emission sources. I conclude that convective transport is an important mechanism controlling the global vertical dispersivity of aerosol.

1.1 Introduction

Aerosol radiative forcing remains one of the largest sources of uncertainty in climate science. Understanding their roles and properties, such as lifetime, chemical and physical processes, and complex spatio-temporal distributions, have been emphasized [*Ramanathan et al.,* 2001; *Bond et al.,* 2013; *Boucher et al.,* 2013]. Part of the reason is a combination of physical and chemical processes controlling aerosol lifetime in the atmosphere (i.e., dry and wet removals), transport patterns, emission sources, and the efficiency of vertical exchange [*Koffi et al.,* 2012; *Storelvmo*. 2012; *Bond et al.,* 2013; *Kipling et al.,* 2013; *Allen and Landuyt,* 2014]. In addition, the free troposphere and the planetary boundary layer can be uncoupled, causing different chemical composition, and thus aerosol properties in different layers [*Guibert et al.,* 2005].

The uncertainty in aerosol radiative forcing is also associated with the vertical aerosol distribution [*Zarzycki and Bond,* 2010; *Bond et al.,* 2013; *Reddy et al.,* 2013; *Samset et al.,* 2013; *Samset and Myhre,* 2015]. The vertical location of black carbon with respect to clouds significantly affects the forcing, increasing or decreasing the forcing when above, or below clouds, respectively [*Zarzycki and Bond,* 2010]. *Bond et al.* [2013] assess the black carbon climate forcing as 1.1 W m^{-2} with a 90% uncertainty range of +0.17 to +2.1 W m^{-2}.

Previous studies have utilized various model simulations and observations to improve our understanding of the aerosol vertical profile and its influence on radiative forcing [*Koch et al.,* 2009; *Yu et al.,* 2010; *Wang et al.,* 2011; *Koffi et al.,* 2012; *Mishra and Shibata.* 2012; *Schwarz et al.,* 2013; *Allen and Landuyt,* 2014; *Hodnebrog et al.,*

2014; *Samset et al.*, 2014; *Wang et al.,* 2014]. Models inadequately reproduce the vertical aerosol profile, placing too much aerosol aloft as compared to observations [*Koch et al.,* 2009; *Koffi et al.,* 2012; *Allen and Landuyt*. 2014]. Excessive aerosol aloft in the models is likely related to transport and removal processes, such as wet removal and convective mass flux [*Vignati et al.,* 2010; *Allen and Landuyt,* 2014]. Using models from the Coupled Model Intercomparison Project version 5 (CMIP5), *Allen and Landuyt* [2014] show that more convective mass flux above 500 hPa is significantly correlated with more black carbon aloft. Moreover, these models may overestimate the amount of convective mass flux, implying a possible cause for their overestimation of aerosol aloft.

Mishra and Shibata [2012] investigate the seasonal variation of aerosol vertical distribution over the central Indo-Gangetic belt (IGB). They find that strong convective activity transports aerosols up to higher altitude during the pre-monsoon season over IGB. *Sun et al.* [2013] report atmospheric instability and precipitation during the monsoon season are major influences on the vertical transport of aerosols over Shijiazhuang, China. Thus, according to previous studies, atmospheric vertical transport and precipitation significantly affect the aerosol vertical distribution at regional scales.

In this study, I utilize observational and reanalysis datasets, including Cloud-Aerosol Lidar Infrared Pathfinder Satellite Observation (CALIPSO), Modern-Era Retrospective Analysis for Research and Applications (MERRA), and Global Precipitation Climatology Project (GPCP) to understand how convective mass flux and precipitation (wet removal) are associated with the aerosol vertical profile over the globe. Section 2 describes the data and methods I employ, and Section 3 discusses our results,

including the importance of convective transport on the vertical dispersivity of aerosols. Conclusions are provided in Chapter 4.

1.2 Data and Methods

Seven years (January 2007 to December 2013) of monthly extinction coefficient at 532nm from CALIPSO [*Winker et al*., 2003] level 3 data product is used. Level 3 data products are derived from the version 3 CALIOP level 2 aerosol profile product and produce day and night segments with all and combined sky condition. For our study, I use both day and night segments from all sky products, screened from cloudy or cloud-free columns, to obtain monthly mean extinction coefficient. I select CALIPSO because it provides the aerosol vertical extinction profile for the entire globe. Data resolution is 2 by 5 degrees with 208 vertical levels. To calculate the average extinction coefficient below/above 500 hPa (and dispersivity), I interpolate extinction coefficient to standard pressure levels at each grid box. Figure 1.1 shows the seven-year climatology of CALIPSO aerosol extinction coefficient, dispersivity, and the average extinction coefficient above 500 hPa.

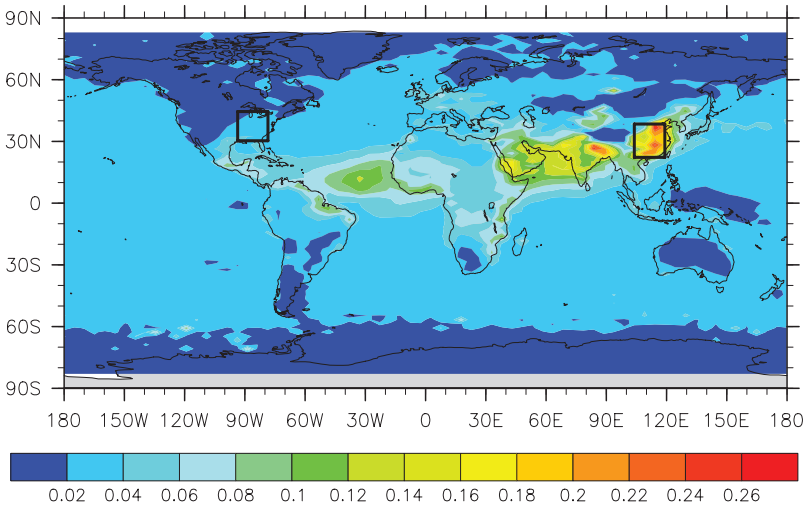
90N
60N
30N
0
30S
60S
90S
180 150W 120W 90W 60W 30W 0 30E 60E 90E 120E 150E 180
0.02 0.04 0.06 0.08 0.1 0.12 0.14 0.16 0.18 0.2 0.22 0.24 0.26

(a)

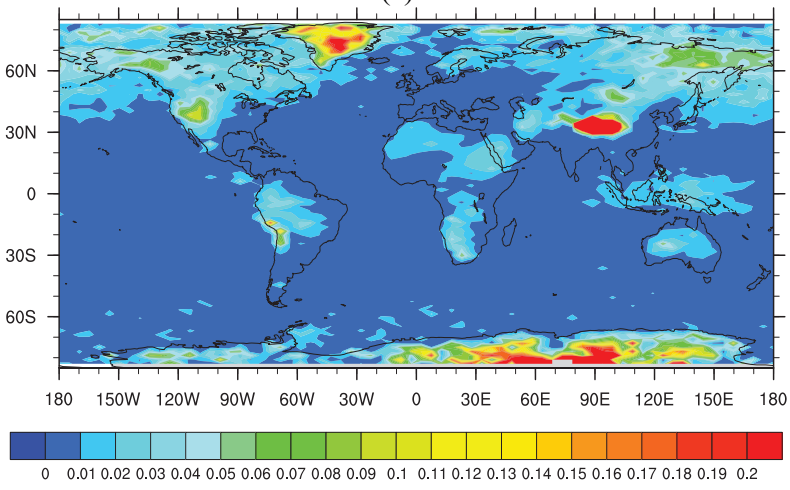
60N
30N
0
30S
60S
180 150W 120W 90W 60W 30W 0 30E 60E 90E 120E 150E 180
0 0.01 0.02 0.03 0.04 0.05 0.06 0.07 0.08 0.09 0.1 0.11 0.12 0.13 0.14 0.15 0.16 0.17 0.18 0.19 0.2

(b)

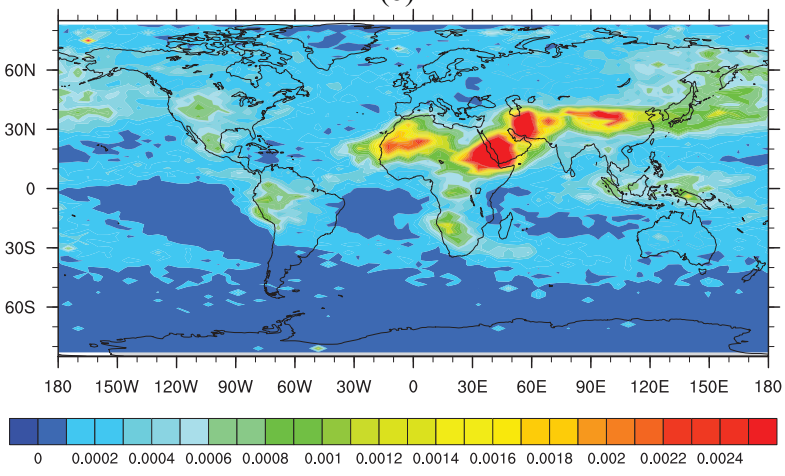
60N
30N
0
30S
60S
180 150W 120W 90W 60W 30W 0 30E 60E 90E 120E 150E 180
0 0.0002 0.0004 0.0006 0.0008 0.001 0.0012 0.0014 0.0016 0.0018 0.002 0.0022 0.0024

(c)

Figure 1.1 Spatial map of the climatology (7 year average) of CALIPSO level 3 a) aerosol extinction coefficient; b) aerosol vertical dispersivity; and c) average extinction coefficient above 500 hPa. MERRA net CMF from the two boxes in panel a is used to calculate the north Pacific (Figure 1.8) and Atlantic (Figure 1.9) correlations.

For convective mass flux data, I use monthly net convective mass flux (CMF) from MERRA [*Rienecker et al.*, 2011]. MERRA is a reanalysis product that uses version 5.2.0 of the Goddard Earth Observing System Data Assimilation System Version 5 (GEOS-5) atmospheric model and data assimilation system (DAS). GEOS5 utilizes moist physics with a large-scale cloud condensate scheme [*Bacmeister et al.*, 2006] and a modified version of relaxed Arakawa-Schubert convective scheme [*Moorthi and Suarez,* 1992]. I use MERRA because it provides 3-D long-term (from 1979 to the present) globally gridded CMF. The spatial resolution is 1.25° by 1.25°, with 72 vertical levels.

I also utilize the ECMWF Interim Re-Analysis (ERA-Interim) [*Uppala et al.* 2005; *Dee et al*., 2011], which archives both upward and downward CMF. ERA-Interim is based on the Integrated Forecast System version 31r2; the atmospheric model uses the *Tiedtke* [1989] bulk mass flux convection scheme, which includes modifications to improve deep convective triggering [*Gregory et al*., 2000; *Bechtold et al*., 2004] and the distinction between shallow, deep and mid-level convection [*Dee et al*., 2011]. I use 12 hourly upward and downward convective mass fluxes, with 60 vertical levels and 1° by 1° horizontal resolution. Monthly averages of both variables are calculated, and then I add upward (positive number) and downward (negative number) convective mass fluxes to obtain net CMF.

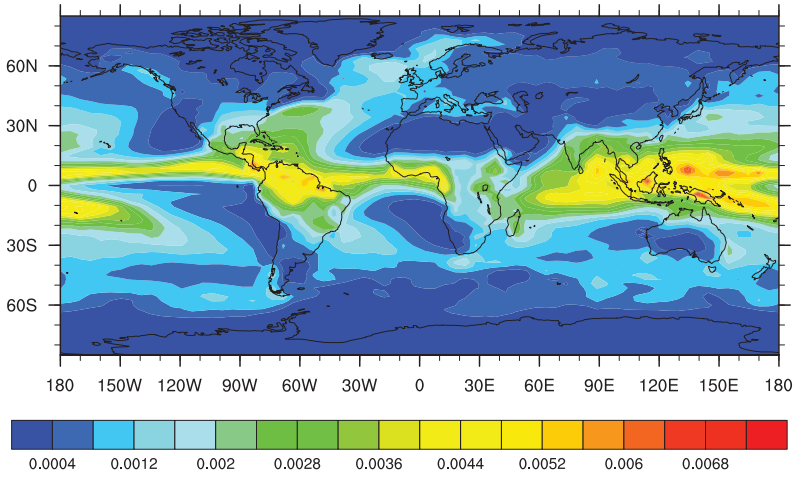
60N
30N
0
30S
60S
180 150W 120W 90W 60W 30W 0 30E 60E 90E 120E 150E 180
0.0004 0.0012 0.002 0.0028 0.0036 0.0044 0.0052 0.006 0.0068

(a)

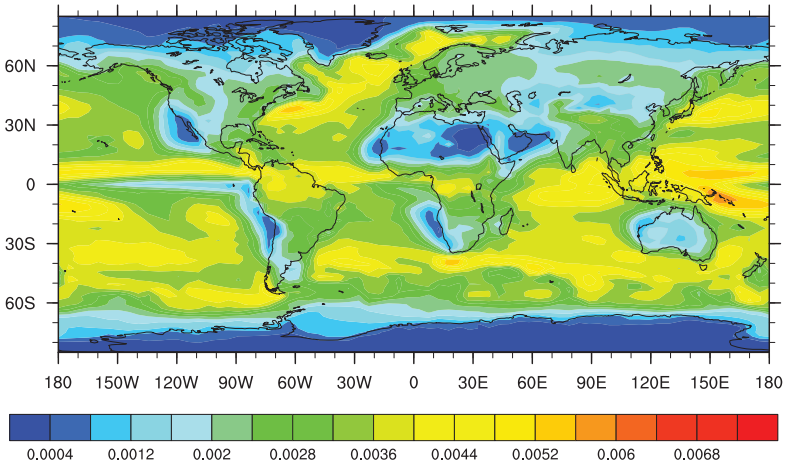
60N
30N
0
30S
60S
180 150W 120W 90W 60W 30W 0 30E 60E 90E 120E 150E 180
0.0004 0.0012 0.002 0.0028 0.0036 0.0044 0.0052 0.006 0.0068

(b)

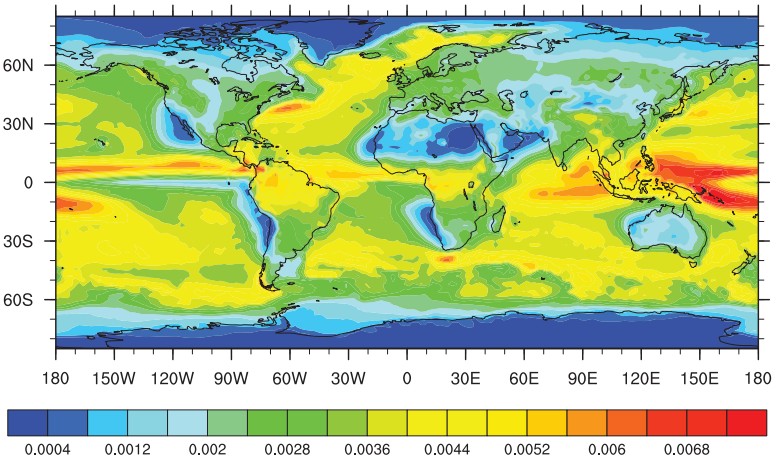
60N
30N
0
30S
60S
180 150W 120W 90W 60W 30W 0 30E 60E 90E 120E 150E 180
0.0004 0.0012 0.002 0.0028 0.0036 0.0044 0.0052 0.006 0.0068

(c)

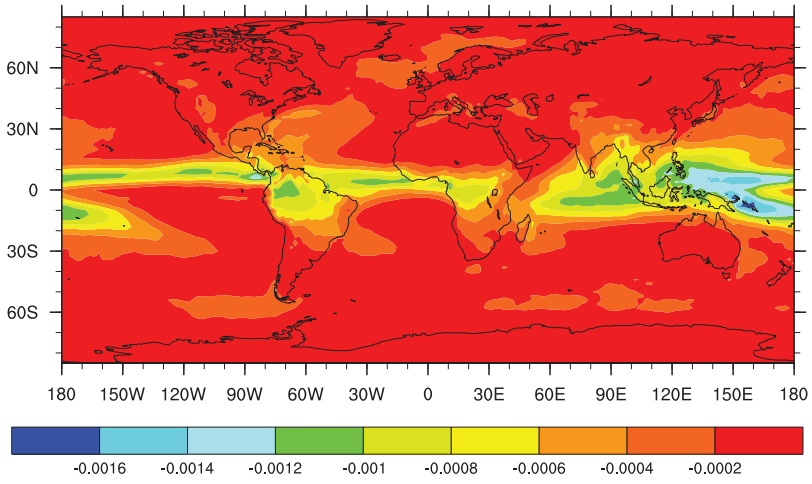

(d)

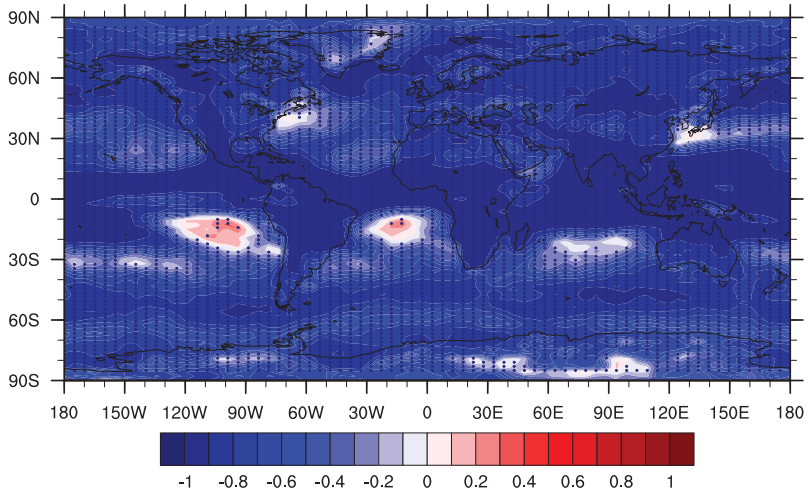

(e)

Figure 1.2 Spatial maps of the climatology (7 year average) of a) MERRA net convective mass flux (CMF); b) ERA-Interim net CMF; c) ERA-Interim upward CMF; d) ERA-Interim downward CMF. e) Spatial map of the linear cross correlation between ERA-Interim upwards and downwards CMF. Symbols represent significance at the 95% confidence level. Unit of CMF are kg m^{-2} s^{-1}. Note that a larger downward CMF in ERA-Interim is represented by a larger negative number.

Both MERRA and ERA-Interim yield similar spatial patterns of net CMF, with ERA-Interim generally yielding larger values (Figure 1.2a and b). I also note that convective updrafts and downdrafts are tightly coupled—the global average annual mean correlation based on ERA-Interim is -0.9, indicating stronger updrafts are associated with stronger downdrafts (Figure 1.2e). Furthermore, net CMF is dominated by upward convection, as updrafts are about an order of magnitude larger than downdrafts (Figure 1.2c and d).

NCAR Climate Data Guide provides monthly Global Precipitation Climatology Project (GPCP) precipitation. GPCP precipitation data is produced by a combination of satellites including SSM/I, AIRS, and others [*Huffman et al*., 2009], rain gauge stations, and sounding observations with 2.5° by 2.5° resolution from 1979 to the present [*Adler et al*., 2003].

I perform cross correlations between column average CMF, precipitation, average extinction coefficient, both below and greater than or equal to 500 hPa (herein defined as the lower and upper troposphere, respectively), and aerosol vertical dispersivity. All data is spatially interpolated to the horizontal resolution of CALIPSO (2° by 5°). A 2-tailed t-test is used to assess the statistical significance of all correlations. Unless otherwise noted, correlations are evaluated on a grid box by grid box basis.

I use the following terminology throughout this paper: aerosol aloft is defined as the average extinction coefficient greater than or equal to 500 hPa. Aerosol vertical dispersivity is defined as the aerosol aloft relative to average column amount. Vertical dispersivity can therefore increase in two ways: either the amount of aerosol aloft

increases relative to the column amount, or the column amount decreases relative to the amount aloft.

1.3 Results

I find significant, positive correlations between CMF and precipitation throughout most of the globe (Figure 1.3). In particular, precipitation and CMF are strongly related to each other in the tropics, where correlations exceed 0.8. More (less) CMF is associated with more (less) precipitation. This relationship is expected, and consistent with moist adiabatic and cloud microphysical processes.

Figure 1.4 shows the correlation between aerosol vertical dispersivity versus MERRA net CMF (Figure 1.4a) and GPCP precipitation (Figure 1.4b). Both panels indicate a positive correlation, particularly over the tropical region. Figure 1.4c and d shows the corresponding correlations of the zonal mean time series, which approach 0.8 in the tropics. Similar results are obtained with ERA-Interim net CMF (Figure 1.5a). Thus, more (less) CMF and precipitation are associated with more (less) vertical dispersivity in the tropics.

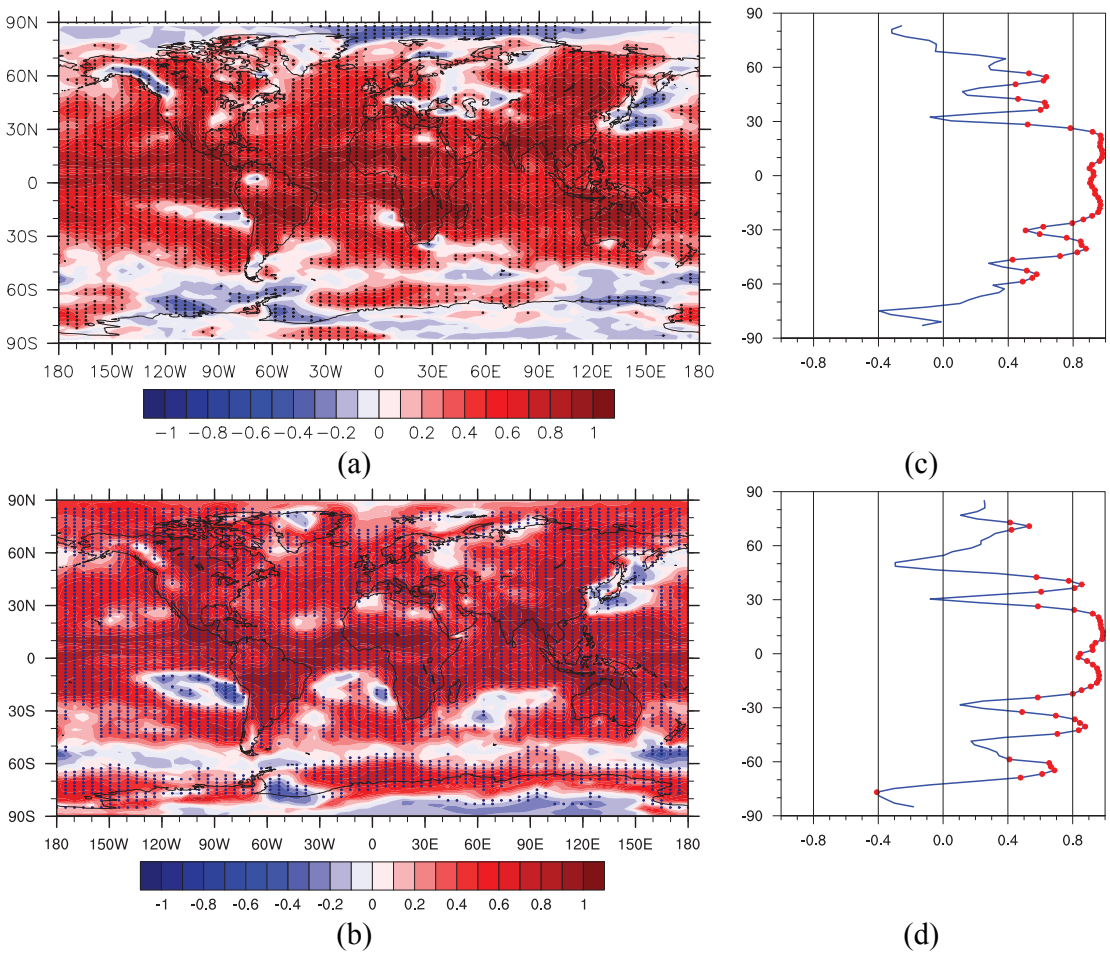

Figure 1.3 Spatial map of the linear cross correlation between a) MERRA net CMF and GPCP precipitation; and b) ERA-Interim net CMF and GPCP precipitation. Corresponding correlation of the zonal mean time series between c) MERRA net CMF and GPCP precipitation; and d) ERA-Interim net CMF and GPCP precipitation. Symbols represent significance at the 95% confidence level.

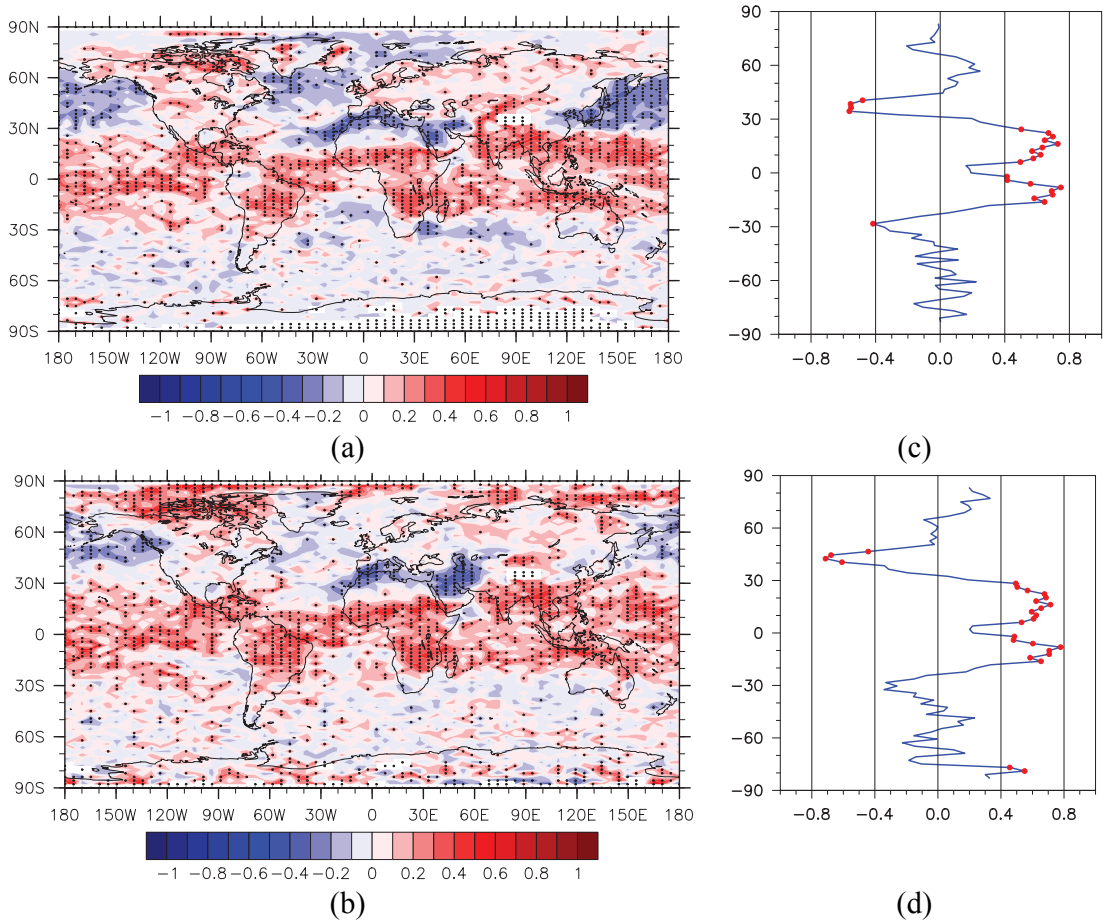

Figure 1.4 Spatial maps of the linear cross correlation between aerosol vertical dispersivity, and (a) MERRA net CMF and (b) GPCP precipitation. Corresponding correlation of the zonal mean time series between aerosol vertical dispersivity, and (c) MERRA net CMF and (d) GPCP precipitation. Symbols represent significance at the 95% confidence level.

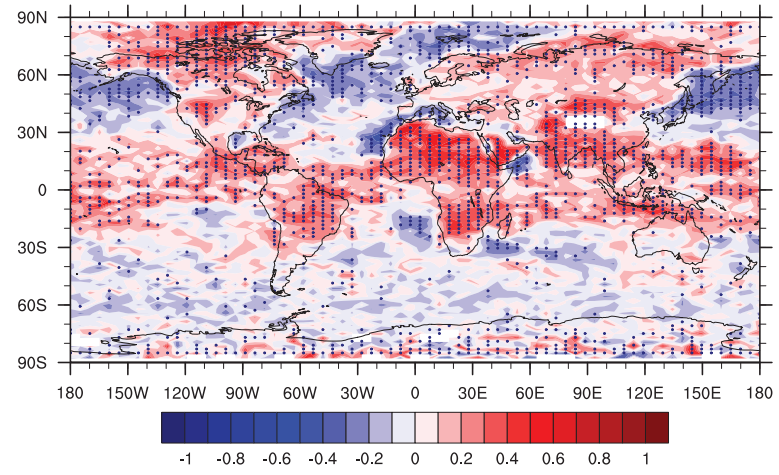
90N
60N
30N
0
30S
60S
90S
180 150W 120W 90W 60W 30W 0 30E 60E 90E 120E 150E 180
-1 -0.8 -0.6 -0.4 -0.2 0 0.2 0.4 0.6 0.8 1

(a)

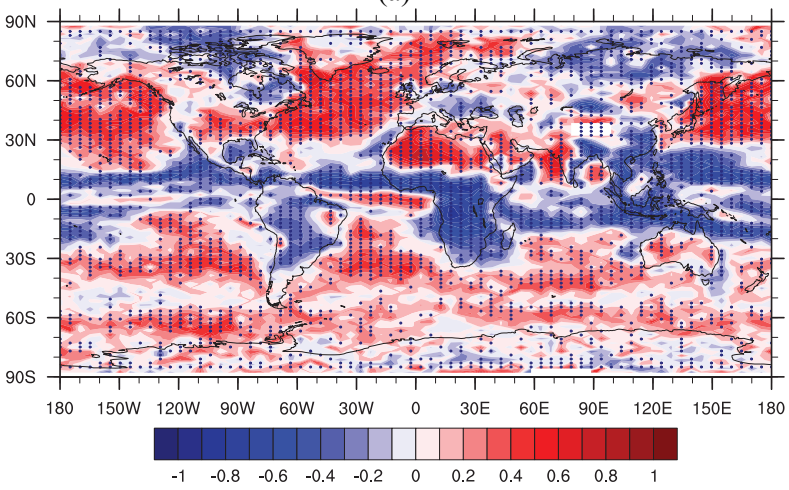
90N
60N
30N
0
30S
60S
90S
180 150W 120W 90W 60W 30W 0 30E 60E 90E 120E 150E 180
-1 -0.8 -0.6 -0.4 -0.2 0 0.2 0.4 0.6 0.8 1

(b)

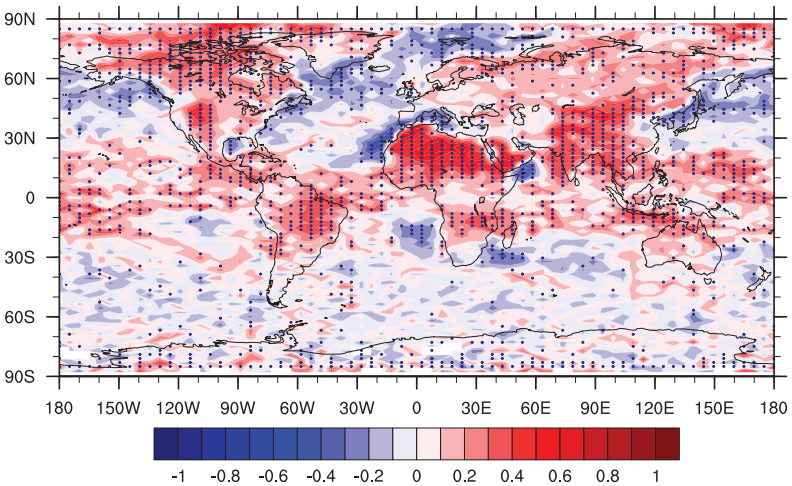
90N
60N
30N
0
30S
60S
90S
180 150W 120W 90W 60W 30W 0 30E 60E 90E 120E 150E 180
-1 -0.8 -0.6 -0.4 -0.2 0 0.2 0.4 0.6 0.8 1

(c)

Figure 1.5 Spatial maps of the linear cross correlation between ERA-Interim net CMF and (a) aerosol vertical dispersivity, (b) average extinction coefficient below 500 hPa, and (c) average extinction coefficient greater than or equal to 500 hPa. Symbols represent significance at the 95% confidence level.

The relationship between MERRA net CMF and precipitation versus average extinction coefficient in the lower troposphere (below 500 hPa) exhibits a significant negative correlation over the tropics (Figure 1.6). Similar results are obtained with ERA-Interim net CMF (Figure 1.5b). This result indicates that more (less) CMF and precipitation are related to less (more) aerosol in the lower troposphere. Precipitation is an important process by which aerosols are removed from the atmosphere [e.g., *Grandey et al*., 2014]. Thus, less aerosol in the lower troposphere is related to more CMF because more CMF is associated with more precipitation (Figure 1.3), and wet removal. I note that more CMF by itself (without an increase in precipitation) should also lead to less aerosol in the lower troposphere, due to enhanced vertical transport of aerosol out of the boundary layer.

I also analyze the relationship between CMF and precipitation versus average total column extinction coefficient. It shows a similar relationship as compared to the relationship between CMF and precipitation versus average extinction coefficient in the lower troposphere. This is consistent with the bulk of aerosols residing below 500hPa, which dominates the total column average.

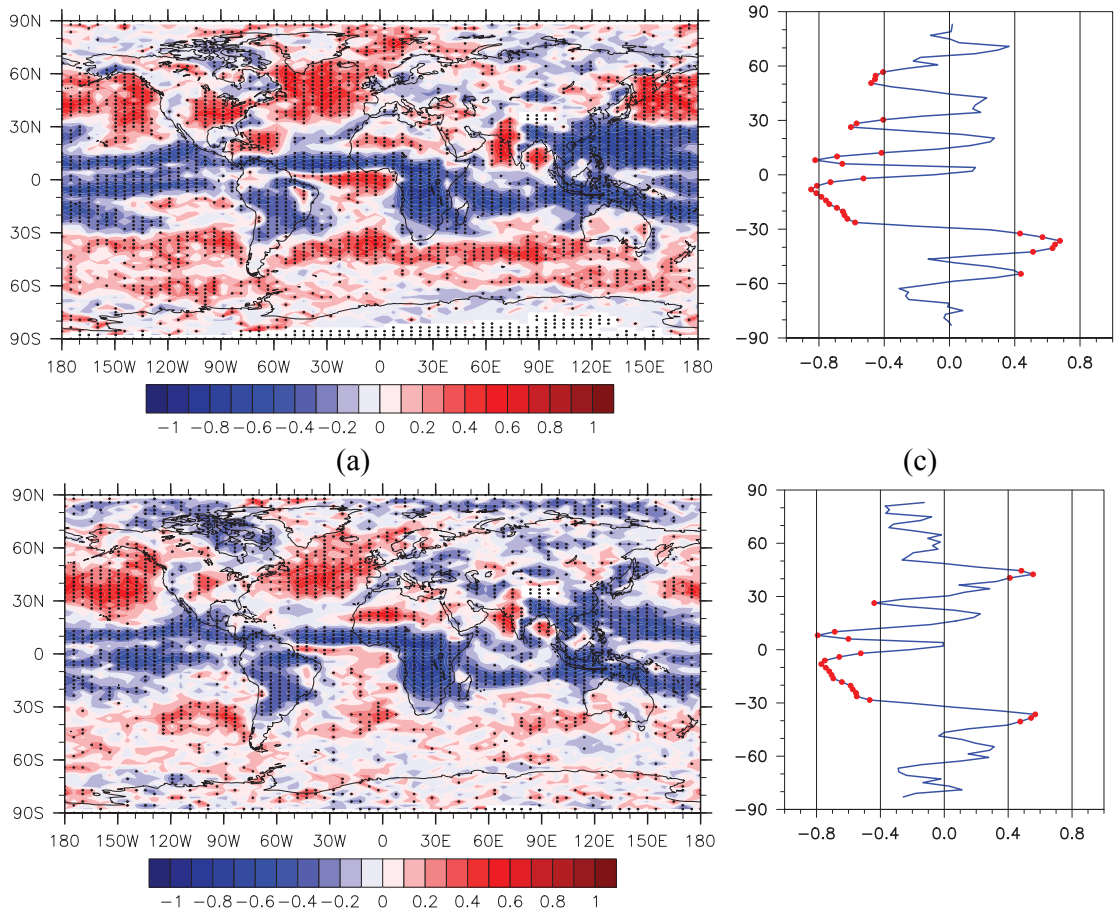

Figure 1.6 Spatial maps of the linear cross correlation between average extinction coefficient below 500 hPa, and (a) MERRA net CMF and (b) GPCP precipitation. Corresponding correlation of the zonal mean time series between average extinction coefficient below 500 hPa, and (c) MERRA net CMF and (d) GPCP precipitation. Symbols represent significance at the 95% confidence level.

Figure 1.7 shows the relationship between CMF and precipitation versus average extinction coefficient in the upper troposphere (greater than or equal to 500 hPa). A similar, but weaker relationship exists as compared to the corresponding relationships with vertical dispersivity (Figure 1.5c shows similar results with ERA-Interim net CMF). A positive relationship over the tropics implies that more (less) CMF is associated with more (less) aerosols aloft.

These results suggest that more CMF is an important mechanism that transports aerosols to higher altitudes. This is despite the increase in precipitation and wet removal associated with more CMF, which is associated with less aerosol in the lower troposphere (Figure 1.6a). Our results therefore suggest that more CMF is associated with enhanced vertical dispersivity by reducing the aerosol extinction column amount (i.e., below 500 hPa), and by increasing the aerosol extinction above 500 hPa. More convection is thus associated with an increase in aerosol aloft.

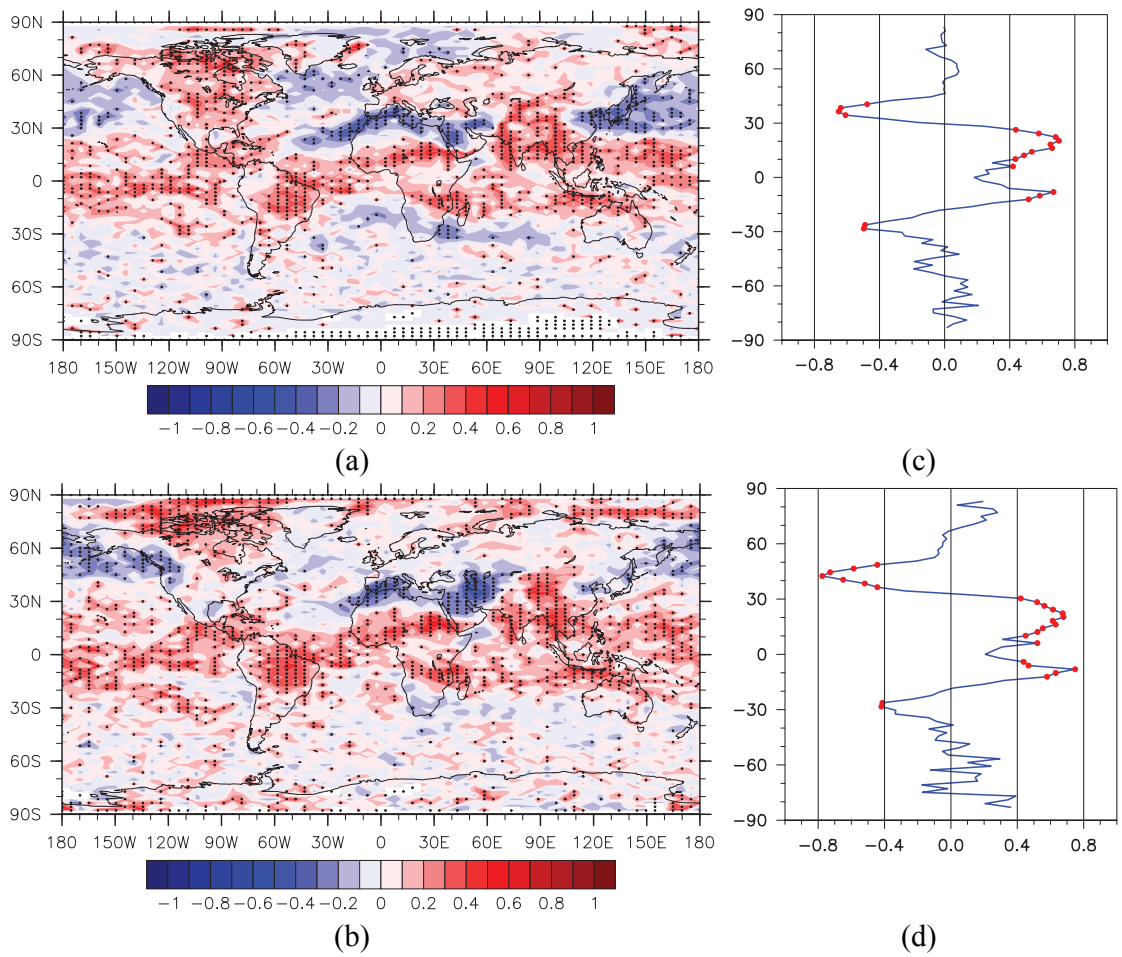

Figure 1.7 Spatial maps of the linear cross correlation between average extinction coefficient greater than or equal to 500 hPa, and (a) MERRA net CMF and (b) GPCP precipitation. Corresponding correlation of the zonal mean time series between average extinction coefficient greater than or equal to 500 hPa, and (c) MERRA net CMF and (d) GPCP precipitation. Symbols represent significance at the 95% confidence level.

Contrary to the results over the tropics, I find opposite correlations over the ocean between 30˚-60˚N, particularly over the Pacific. In this region, more (less) CMF and precipitation are associated with less (more) vertical dispersivity, including less (more) average extinction coefficient in the upper troposphere and more (less) average extinction coefficient in the lower troposphere.

To understand the opposite correlations over the NH mid-latitude oceans, I conduct two another analyses that no longer involve correlations on a grid box by grid box basis. I take aerosol vertical dispersivity from the North Atlantic and Pacific oceans and correlate it with CMF over the two biggest, and upwind, emission sources (Figure 1.1a indicates the two locations, indicated with black boxes over southeast Asia and the eastern United States).

Correlations between MERRA net CMF and precipitation versus vertical dispersivity change from negative to positive over the north Pacific (Figure 1.8) and Atlantic (Figure 1.9). I also find that more CMF over these emissions sources is associated with more aerosol aloft over the Atlantic and Pacific Oceans. These results suggest that CMF over these emissions sources play an important role in controlling the aerosol vertical dispersivity—and the aerosol aloft—downwind, over the NH mid-latitude oceans.

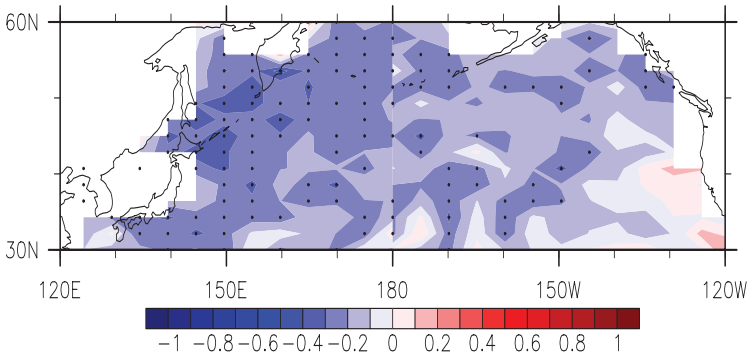
60N
30N
120E
150E
180
150W
120W
−1 −0.8 −0.6 −0.4 −0.2 0 0.2 0.4 0.6 0.8 1

(a)

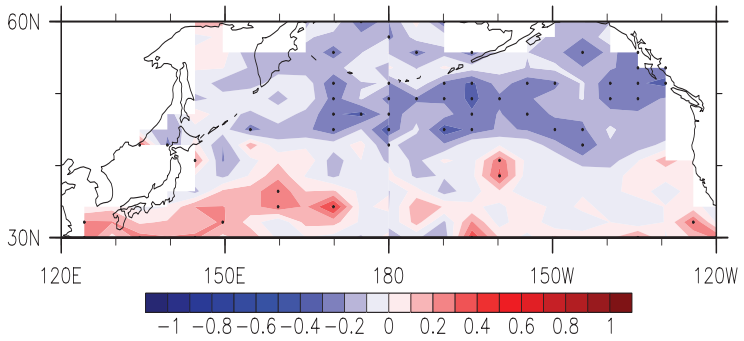
60N
30N
120E
150E
180
150W
120W
−1 −0.8 −0.6 −0.4 −0.2 0 0.2 0.4 0.6 0.8 1

(b)

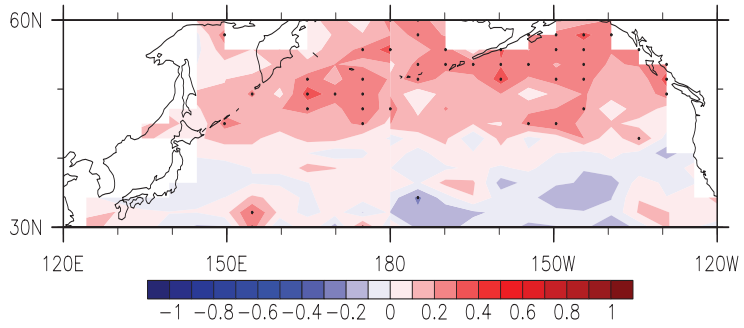
60N
30N
120E
150E
180
150W
120W
−1 −0.8 −0.6 −0.4 −0.2 0 0.2 0.4 0.6 0.8 1

(c)

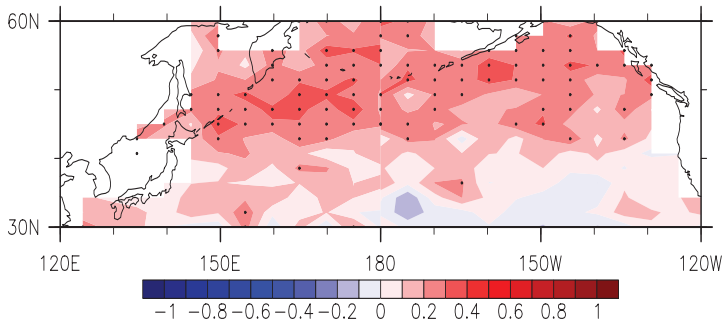
60N
30N
120E
150E
180
150W
120W
−1 −0.8 −0.6 −0.4 −0.2 0 0.2 0.4 0.6 0.8 1

(d)

Figure 1.8 North Pacific spatial maps of the linear cross correlation between aerosol vertical dispersivity and (a) MERRA net CMF, (b) GPCP precipitation over identical grid boxes, and between aerosol vertical dispersivity over the north Pacific and (c) MERRA net CMF, (d) GPCP precipitation over SE Asia (103.9° to 119.1°E, 22.2° to 38.4°N). Symbols represent significance at the 95% confidence level.

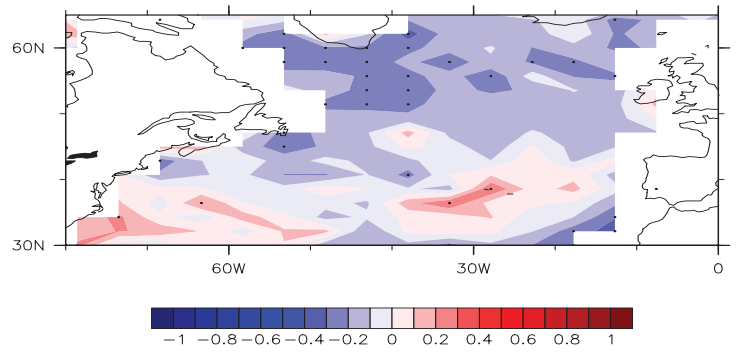
60N
30N
60W
30W
0
−1 −0.8 −0.6 −0.4 −0.2 0 0.2 0.4 0.6 0.8 1

(a)

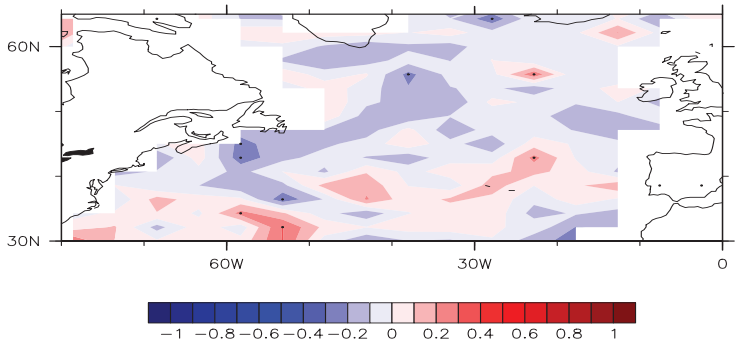
60N
30N
60W
30W
0
−1 −0.8 −0.6 −0.4 −0.2 0 0.2 0.4 0.6 0.8 1

(b)

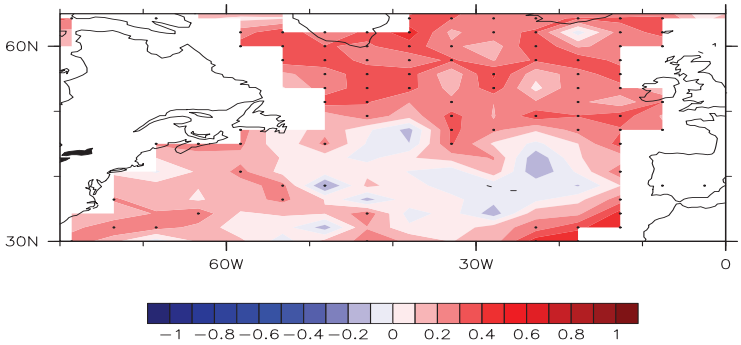
60N
30N
60W
30W
0
−1 −0.8 −0.6 −0.4 −0.2 0 0.2 0.4 0.6 0.8 1

(c)

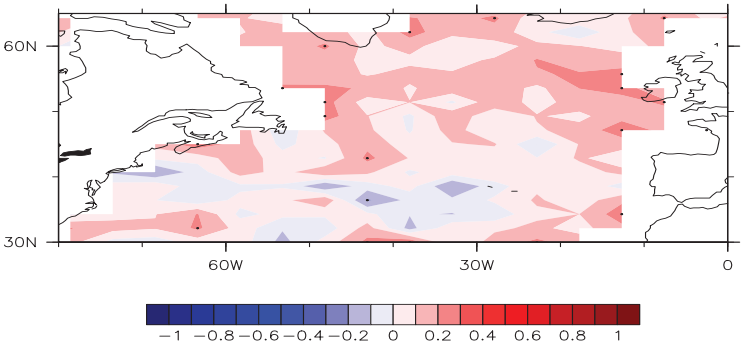
60N
30N
60W
30W
0
−1 −0.8 −0.6 −0.4 −0.2 0 0.2 0.4 0.6 0.8 1

(d)

Figure 1.9 North Atlantic spatial maps of the linear cross correlation between aerosol vertical dispersivity and (a) MERRA net CMF, and (b) GPCP precipitation over identical grid boxes, and between aerosol vertical dispersivity over the north Atlantic and (c) MERRA net CMF, and (d) GPCP precipitation over the eastern United States (-93.8° to -78.6°E, 30.3° to 44.5°N). Symbols represent significance at the 95% confidence level.

A question still remains—why are the grid box by grid box relationships reversed over the NH mid-latitude oceans? Figure 1.10d, e, and f shows that the correlation between ERA-Interim upward CMF and aerosol vertical dispersivity, aerosol aloft, etc. are nearly identical to those based on net CMF (Figure 1.5), including the opposite correlations over the NH mid-latitude oceans. This is because net CMF is dominated by upward convection (Figure 1.2). However, positive correlations between ERA-Interim downward CMF and both aerosol vertical dispersivity and average extinction coefficient above 500 hPa exist (Figure 1.10a and 1.10c). Similarly, negative correlations exist between downward CMF and average extinction coefficient in the lower troposphere (Figure 1.10b). These results indicate that more (less) downward CMF is associated with more (less) aerosol in the lower troposphere and less (more) aerosol in the upper troposphere and vertical dispersivity.

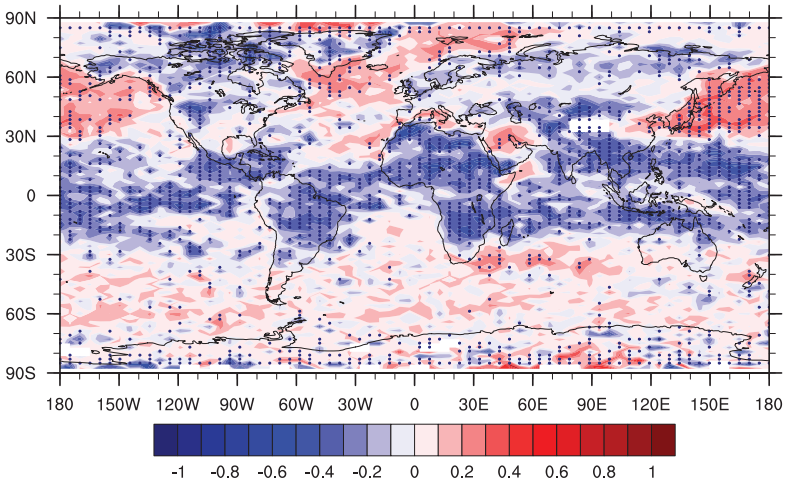
90N
60N
30N
0
30S
60S
90S
180 150W 120W 90W 60W 30W 0 30E 60E 90E 120E 150E 180
-1 -0.8 -0.6 -0.4 -0.2 0 0.2 0.4 0.6 0.8 1

(a)

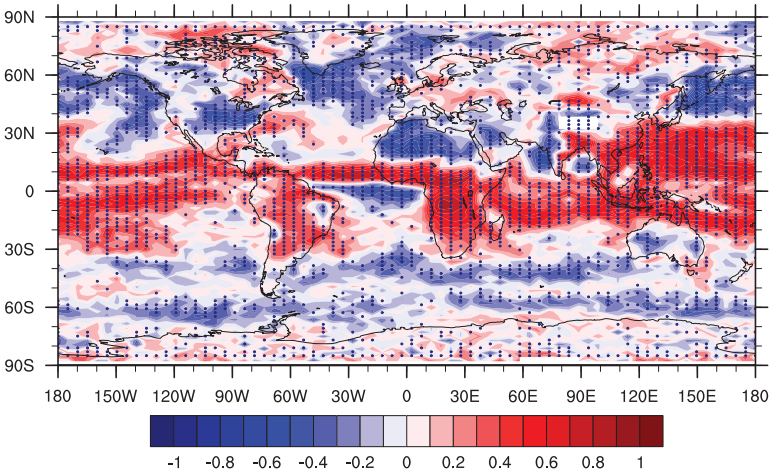
90N
60N
30N
0
30S
60S
90S
180 150W 120W 90W 60W 30W 0 30E 60E 90E 120E 150E 180
-1 -0.8 -0.6 -0.4 -0.2 0 0.2 0.4 0.6 0.8 1

(b)

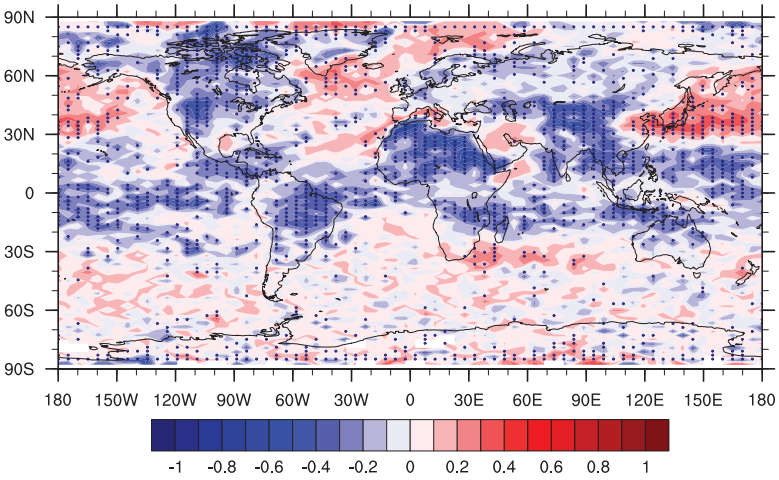
90N
60N
30N
0
30S
60S
90S
180 150W 120W 90W 60W 30W 0 30E 60E 90E 120E 150E 180
-1 -0.8 -0.6 -0.4 -0.2 0 0.2 0.4 0.6 0.8 1

(c)

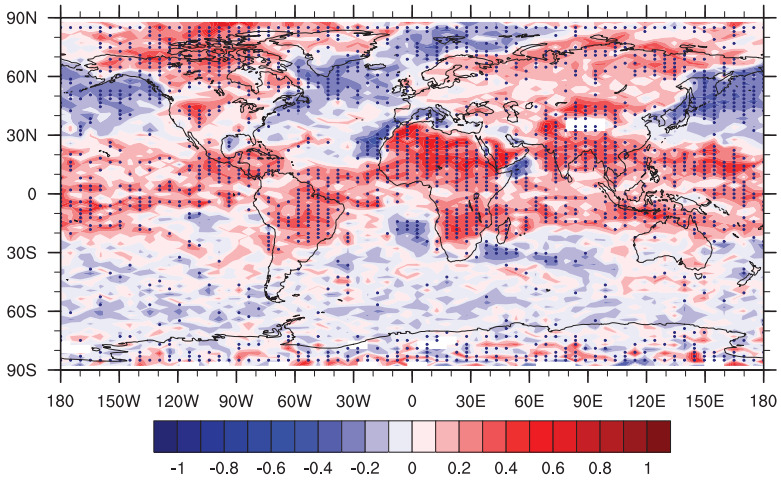
90N
60N
30N
0
30S
60S
90S
180 150W 120W 90W 60W 30W 0 30E 60E 90E 120E 150E 180
-1 -0.8 -0.6 -0.4 -0.2 0 0.2 0.4 0.6 0.8 1

(d)

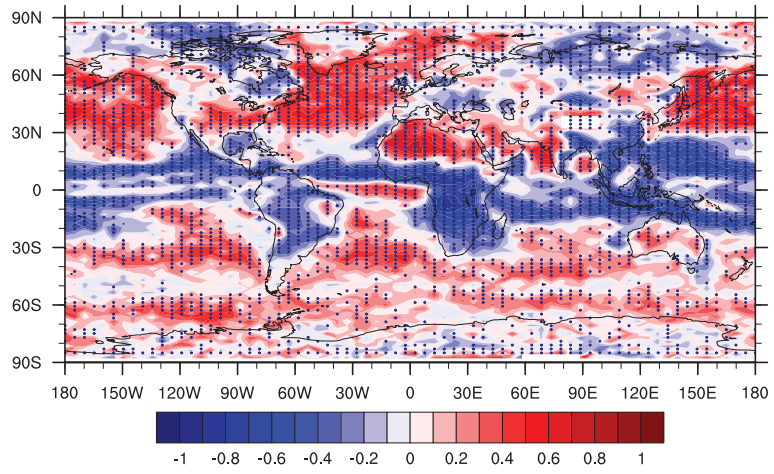
90N
60N
30N
0
30S
60S
90S
180 150W 120W 90W 60W 30W 0 30E 60E 90E 120E 150E 180
-1 -0.8 -0.6 -0.4 -0.2 0 0.2 0.4 0.6 0.8 1

(e)

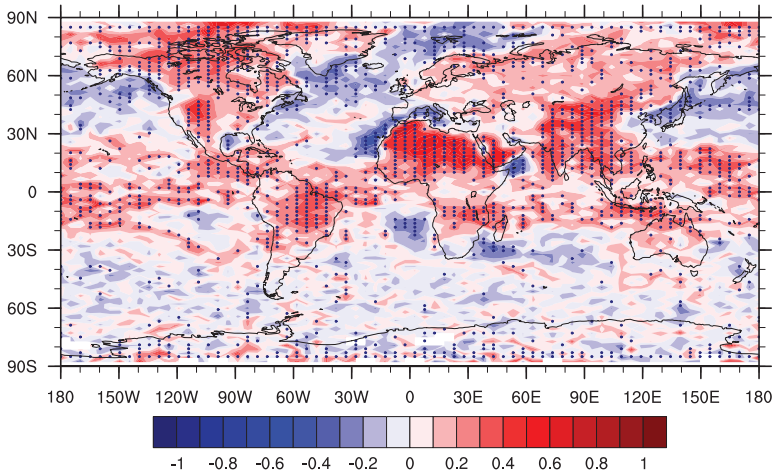
90N
60N
30N
0
30S
60S
90S
180 150W 120W 90W 60W 30W 0 30E 60E 90E 120E 150E 180
-1 -0.8 -0.6 -0.4 -0.2 0 0.2 0.4 0.6 0.8 1

(f)

Figure 1.10 Spatial maps of the linear cross correlation between ERA-Interim downward CMF and a) aerosol vertical dispersivity, (b) average extinction coefficient below 500hPa, (c) average extinction coefficient greater than or equal to 500 hPa; and ERA-Interim upward CMF and (d) aerosol vertical dispersivity, (e) average extinction coefficient below 500hPa, (f) average extinction coefficient greater than or equal to 500 hPa. Symbols represent significance at the 95% confidence level. Stronger upward CMF is a larger positive number, but a stronger downward CMF is a larger negative number. Thus, a positive correlation between downward CMF and dispersivity means stronger downdrafts are associated with less dispersivity, and vice versa.

Consistent with (1) large emissions from SE Asia and the eastern US and (2) the importance of local convection in lofting these aerosols and subsequent downwind transport over the NH mid-latitude oceans (Figure 1.8)—these ocean regions, particularly the Pacific, feature relatively large aerosol vertical dispersivities and average extinction coefficient greater than or equal to 500 hPa (Figure 1.1b and c). Because convection is associated with both updrafts and downdrafts, and these are tightly coupled (Figure 1.2e), this leads to the opposite correlations between net CMF and dispersivity over the NH mid-latitude oceans. The dominant effect of convection over the NH mid-latitude oceans is for the convective downdrafts to transport aerosol that has already been lofted to lower altitudes.

References

Adler, R. F., Gu, G., and Huffman, G. J. (2003), The version-2 global precipitation climatology project (GPCP) monthly precipitation analysis (1979-present), *J. Hydrometeorol.,* 4, 1147-1167, doi: http://dx.doi.org/10.1175/1525-7541(2003)004<1147:TVGPCP>2.0.CO;2.

Allen, R. J., and Landuyt, W. (2014), The vertical distribution of black carbon in CMIP5 models: Comparison to observations and the importance of convective transport. *J. Geophys. Res. Atmos., 119*(8), 4808-4835, doi: 10.1002/2014JD021595.

Bacmeister, J. T., Suarez, M. J. and Franklin R. Robertson, (2006) Rain Reevaporation, Boundary Layer–Convection Interactions, and Pacific Rainfall Patterns in an AGCM. *J. Atmos. Sci.*, 63, 3383–3403. doi: http://dx.doi.org/10.1175/JAS3791.1.

Bechtold, P., Chaboureau, J.-P., Beljaars, A., Betts, A. K., Köhler, M., Miller, M. and Redelsperger, J.-L. (2004), The simulation of the diurnal cycle of convective precipitation over land in a global model. Q.J.R. Meteorol. Soc., 130: 3119–3137. doi:10.1256/qj.03.103.

Bond, T. C. et al., (2013), Bounding the role of black carbon in the climate system: A scientific assessment. J. Geophys. Res. Atmos., 118, 5380-5552, doi: 10.1002/jgrd.50171.

Boucher, O., et al. (2013), Clouds and aerosols, in Climate Change 2013: The Physical Science Basis. Contribution of Working Group I to the Fifth Assessment Report of the Intergovernmental Panel on Climate Change, edited by T. F. Stocker et al., Cambridge Univ. Press, Cambridge, U. K., and New York.

Dee, D. P. et al., (2011), The ERA-Interim reanalysis: configuration and performance of the data assimilation system. Q.J.R. Meteorol. Soc., 137: 553–597. doi:10.1002/qj.828.

Grandey, B. S., A. Gururaj, P. Stier, and T. M. Wagner (2014), Rainfall-aerosol relationships explained by wet scavenging and humidity, Geophys. Res. Lett., 41, 5678–5684, doi:10.1002/2014GL060958.

Gregory, D., Morcrette, J.-J., Jakob, C., Beljaars, A. C. M. and Stockdale, T. (2000), Revision of convection, radiation and cloud schemes in the ECMWF integrated forecasting system. Q.J.R. Meteorol. Soc., 126: 1685–1710. doi:10.1002/qj.49712656607.

Guiberta, S., Matthias, V., Schulz, M., Bösenberg, J., Eixmann, R., Mattis, I., Pappalardo, G., Perrone, M. R., Spinelli, N., Vaughan, G. (2005), The vertical distribution of aerosol over Europe—Synthesis of one year of EARLINET aerosol lidar

measurements and aerosol transport modeling with LMDzT-INCA. Atmos. Environ, 39, 2933-2943, doi: 10.1016/j.atmosenv.2004.12.046.

Hodnebrog, Ø., Myhre, G., and Samset, B. H. (2014). How shorter black carbon lifetime alters its climate effect. *Nature communications*, 5, doi: 10.1038/ncomms6065.

Huffman, G. J., R. F. Adler, D. T. Bolvin, and G. Gu (2009), Improving the global precipitation record: GPCP Version 2.1, Geophys. Res. Lett., 36, L17808, doi:10.1029/2009GL040000.

Kipling, Z., Stier, P., Schwarz, J.P., Perring, A.E., Spackman, J.R., Mann, G.W., Johnson, C.E. & Telford, P.J. 2013, "Constraints on aerosol processes in climate models from vertically-resolved aircraft observations of black carbon", Atmospheric Chemistry and Physics, 13(12), 5969. doi:http://dx.doi.org/10.5194/acp-13-5969-2013.

Koch, D., et al. (2009), Evaluation of black carbon estimates in global aerosol models. *Atmos. Chem. Phys*, 9, 9001-9026, doi: 10.5194/acp-9-9001-2009.

Koffi, B., et al. (2012), Application of CALIOP layer product to evaluate the vertical distribution of aerosols estimated by global models: AeroCom phase I results, J. Geophys. Res., 117, D10201, 2012 doi: 10.1029/2011JD016858.

Mishra, A. K., and Shibata, T. (2012), Climatological aspects of seasonal variation of aerosol vertical distribution over central Indo-Gangetic belt (IGB) inferred by the space-borne lidar CALIOP. *Atmos. Envir.*, 46, 365-375, doi: 10.1016/j.atmosenv.2011.09.052.

Moorthi, S., and M.J. Suarez (1992), Relaxed Arakawa-Schubert, A Parameterization of Moist Convection for General-Circulation Models. *Mon. Wea. Rev*. 120, 978-1002, doi: http://dx.doi.org/10.1175/1520-0493(1992)120<0978:RASAPO>2.0.CO;2.

Ramanathan, V. C., Crutzen, P. J., Kiehl., J. T. Rosenfeld., D. (2001). Aerosols, climate, and the hydrological cycle. *Science*, 294(5549), 2119-2124, doi: 10.1126/science.1064034.

Reddy, K., Phani Kumar, D. V., Nazeer Ahammed, Y., and Naja., M. (2013), Aerosol vertical profiles strongly affect their radiative forcing uncertainties: study by using ground-based lidar and other measurements. *Remote. Sens. Lett*, 4(10), 1018-1027, doi: 10.1080/2150704X.2013.828182.

Rienecker, M. M., et al. (2011), MERRA: NASA's Modern-Era Retrospective Analysis for Research and Applications, *J. Climate*, 24, 3624–3648, doi: http://dx.doi.org/10.1175/JCLI-D-11-00015.1.

Samset, B. H., et al. (2013), Black carbon vertical profiles strongly affect its radiative forcing uncertainty, *Atmos. Chem. Phys*., 13, 2423-2434, doi: 10.5194/acp-13-2423-2013.

Samset, B. H., et al. (2014), Modelled black carbon radiative forcing and atmospheric lifetime in AeroCom Phase II constrained by aircraft observations, Atmos. Chem. Phys., 14, 12465-12477, doi: :10.5194/acp-14-12465-2014.

Samset, B. H., and G. Myhre (2015), Climate response to externally mixed black carbon as a function of altitude, J. Geophys. Res. Atmos., 120, 2913–2927, doi: 10.1002/2014JD022849.

Schwarz, J. P., B. H. Samset, A. E. Perring, J. R. Spackman, R. S. Gao, P. Stier, M. Schulz, F. L. Moore, E. A. Ray, and D. W. Fahey (2013), Global-scale seasonally resolved black carbon vertical profiles over the Pacific, Geophys. Res. Lett., 40, 5542–5547, doi:10.1002/2013GL057775.

Storelvmo, T. (2012). Uncertainties in aerosol direct and indirect effects attributed to uncertainties in convective transport parameterizations. *Atmos. Res*, *118*, 357-369, doi:10.1016/j.atmosres.2012.06.022.

Sun, X., Yin, Yan., Sun, Yuwen., Sun., Yun., Liu, Wei., Han., Yang. (2013). Seasonal and vertical variations in aerosol distribution over Shijiazhuang, China. *Atmos. Envir.*, 81, 245-252, doi: 10.1016/j.atmosenv.2013.08.009.

Tiedtke, M. (1989), A comprehensive mass flux convection scheme for cumulus parameterization in a large-scale model. *Mon. Weather Rev.,* 117, 1779-1800.

Uppala, S. M., et al., (2005), The ERA-40 re-analysis, *Q. J. R. Meteorol. Soc*., 131, 2961-3012.

Vignati, E., Karl, M., Krol, M., Wilson, J., Stier, P., and Cavalli., F. (2010), Sources of uncertainties in modelling black carbon at the global scale, Atmos. Chem. Phys., 10(6), 2595–2611, doi: 10.5194/acp-10-2595-2010.

Wang Q., et al. (2011), Source of carbonaceous aerosols and deposited black carbon in the Arctic in winter-spring: implication for radiative forcing, Atmos. Chem. Phys, 11, 12453-12473, doi: 10.5194/acp-11-12453-2011.

Wang, Q., Jacob, D. J., Fisher, J. A., Mao, J., Leibensperger, E. M., Carouge, C. C., Le Sager, P., Kondo, Y., Jimenez, J. L., Cubison, M. J., and Doherty, S. J. (2014), Global Budget and radiative forcing black carbon aerosol: Constraints from pole-to-pole (HIPPO) observation across the Pacific, *J. Geophys. Res,* 119, 195-206, doi: 10.1002/2013JD020824.

Winker, D. M., J. Pelon, and M. P. McCormick (2003), The CALIPSO mission: Spaceborne lidar for observation of aerosols and clouds, *Proc. SPIE.*, 4893, 1–11, doi: 10.1117/12.466539.

Yu, H., et al., (2010), Global view of aerosol vertical distributions from CALIPSO lidar measurements and GOCART simulations: Regional and seasonal variations. *J. Geophys. Res*, 115(D4). doi: 10.1029/2009JD013364.

Zarzycki, C. M., and Bond, T. C. (2010), How much can the vertical distribution of black carbon affect its global direct radiative forcing?, *Geophys. Res. Lett.*, *37*(20), doi:10.1029/2010GL044555.

Chapter 2 A likely increase in fine particulate matter and premature mortality under future climate change

Abstract

Climate change modulates the concentration of fine particulate matter ($PM_{2.5}$) via modifying atmospheric circulation, temperature, and the hydrological cycle. Furthermore, $PM_{2.5}$ is associated with respiratory diseases and premature mortality. Here, seven models are used to assess the response of $PM_{2.5}$ to end of the 21st century climate change under Representative Concentration Pathway 8.5, and the corresponding impact on premature mortality. The majority of models yield an increase in both $PM_{2.5}$ and premature mortality associated with lung cancer and cardiopulmonary disease in all world regions except Africa. These results are robust across five different future population projections, although the magnitude of premature deaths can vary by up to a factor of two. Much larger uncertainty is related to uncertainty in model physics and the representation of aerosol processes. Our results suggest that future emission reductions are necessary to avoid the likely health risks associated with increasing $PM_{2.5}$ in a warmer world.

2.1 Introduction

Air pollutant concentrations vary depending on diverse factors including emissions, weather, and climate change [*Jacob and Winner,* 2009*; Mickley et al.,* 2004; *Westervelt et al.,* 2016]. It is important to understand how aerosol burden changes in the future under diverse emission scenarios to improve air pollution policy decision-making. Recent studies suggest that future climate change related to continued greenhouse gas (GHGs) emissions has significant effects on aerosol burden and air pollutant concentration, independent of any changes in emissions [*Allen et al.,* 2016; *Kloster et al.,* 2010; *Shen et al.,* 2016; *Westervelt et al.,* 2016].

Westervelt et al. [2016] finds that climate change yields an increase in $PM_{2.5}$ in all but one of the Representative Concentration Pathways (RCPs), and relates this to local temperature increases. Similarly, *Allen et al.* [2016] shows that GHG-induced warming yields increases in surface concentration and burden of both anthropogenic and natural aerosols. Anthropogenic aerosols, including black carbon (BC), primary organic matter (POM), and sulfate (SO_4), generally increase more than natural aerosols, such as dust and sea salt. In addition, the increase in anthropogenic aerosols primarily occurs over the Northern Hemisphere mid-latitude continents during summertime, which they relate to a corresponding decrease in aerosol wet removal driven by reduction in large-scale precipitation.

An increase in air pollutant concentration, especially fine particulate matter ($PM_{2.5}$), is associated with an increase in premature mortality [*Lelieveld et al.,* 2015; *Nawahda et al.,* 2012; *Silva et al.,* 2013]. Hence, previous studies have focused on how

future climate change affects $PM_{2.5}$ concentrations, and the corresponding impacts on mortality [*Fang et al.,* 2013; *Silva et al.,* 2013; *Silva et al.,* 2016; *Silva et al.,* 2017].

Fang et al. [2013] examines the effects of climate change due to GHGs on $PM_{2.5}$ air quality over the 21st century using a global coupled chemistry-climate model. The results show that global annual premature mortality increases by almost 100,000 deaths. *Silva et al.* [2017] estimates future premature mortality related to four diseases under future climate change using an ensemble of global chemistry climate models. Their multi-model average results indicate an increase in global premature mortality in both 2030 and 2100 at 55,600 (-34,300 to 164,000) and 215,000 (-76,100 to 595,000) deaths/year, respectively. In addition, all world regions yield an increase in premature deaths, except Africa.

Here I assess changes in $PM_{2.5}$ concentration due to climate change at the end of the 21st century using five state-of-the-art chemistry-climate models that participated in the Atmospheric Chemistry and Climate Model Inter-comparison Project (ACCMIP) and in-house Community Atmosphere Model versions 4 and 5 (CAM4/5) simulations. In addition, premature mortality related to lung cancer (LC) and cardiopulmonary disease (CPD) are estimated using $PM_{2.5}$ changes and five different future population projections for the end of the 21st century.

Our study differs from previous studies [*Fang et al.,* 2013; *Silva et al.,* 2013] in that I use several different global chemistry-climate models. *Post et al.* [2012] and *Silva et al.* [2013] suggest that using a single model may yield significant uncertainty; therefore, multiple models are required to determine how robust the effects of climate

change are on $PM_{2.5}$ concentration. I therefore focus on model agreement, and emphasize changes in which the majority of models agree (i.e., at least four of the seven models). Although our analysis is similar to *Silva et al.* [2017], including the evaluation of ACCMIP models, three major distinctions include: 1. I focus on archived $PM_{2.5}$ from all ACCMIP models, except HadGEM2 (which lacks archived $PM_{2.5}$); 2. I use five different estimates of future population to quantify uncertainty in premature deaths due to uncertainty in future population projections; and 3. I conduct our own in-house CAM4/5 simulations using an experimental design analogous to that used in ACCMIP, and evaluate the corresponding changes in $PM_{2.5}$ and premature deaths. This paper is organized as follows. Section 2 describes the data and methods I use, and Section 3 discusses our results, including an evaluation of climate driven changes in $PM_{2.5}$ concentration and associated premature mortality. Conclusions are provided in Chapter 4.

2.2 Methods

I use $PM_{2.5}$ mass mixing ratio from the Atmospheric Chemistry and Climate Model Intercomparison Project (ACCMIP) [*Lamarque et al., 2013*] and CAM4/5 simulations to evaluate changes in $PM_{2.5}$ concentration due to GHG-induced climate change at the end of the 21st century. Two time-slice experiments, representing climate in the year 2000 and 2100, are used. Both feature identical aerosol emissions from the year 2000; the end of the 21st century simulation uses sea surface temperatures, sea-ice concentrations and GHGs based on RCP8.5, a business-as-usual scenario with maximum warming. CAM4/5 simulations are conducted using an analogous experimental design as

ACCMIP, with sea surface temperature and sea-ice concentration anomalies from the ensemble mean of 18 Coupled Model Intercomparison Project version 5 (CMIP5) RCP8.5 models (2090-2099 relative to 2006-2015) and RCP8.5 GHGs based on the 2090-2099 mean.

Annual mean $PM_{2.5}$ values are calculated using monthly average data from each model. Comparison of the two experiments (2100 minus 2000) yields the change in $PM_{2.5}$ concentration at the end of the 21st century under GHG-induced climate change. I use each model's lowest vertical level to represent surface concentration.

Five ACCMIP models (Table 2.1) archived the necessary data, including archived $PM_{2.5}$ mass mixing ratios, or individual aerosol species' mass mixing ratios that can be used to approximate $PM_{2.5}$. Since the Hadley Centre Global Environmental Model version 2 (HadGEM2) [*Collins et al.,* 2011] lacks archived $PM_{2.5}$, I estimate it using Eq. [1] [*Silva et al.,* 2013] and six reported aerosol species: black carbon (BC), organic aerosol (OA), sulfate (SO_4), secondary organic aerosol (SOA), sea salt (SS), and dust. CAM4/5 $PM_{2.5}$ mass mixing ratio is obtained by summing all non-coarse mode aerosol species. For CAM5, this includes the non-coarse mode components of the six aerosol species above; for CAM4, five of the six species are used, as CAM4 lacks SOA.

$$\text{Estimated } PM_{2.5} = BC + OA + SO_4 + SOA + 0.25*SS + 0.1*Dust \qquad \text{Eq. [1]}$$

Table 2.1 Models used in this study. The first five model simulations come from ACCMIP; the last two model simulations (CAM4/5) were performed by the authors. Also included is the number of simulation years available for each experiment, the horizontal and vertical resolutions, and the corresponding reference. In most models, $PM_{2.5}$ is based on six species, including black carbon, organic aerosol, sulfate, secondary organic aerosol, sea salt, and dust. However, in CAM4, no secondary organic aerosol is included, so $PM_{2.5}$ is based on five species; in GFDL-AM3 and GISS-E2-R, ammonium sulfate and nitrate are also included, so $PM_{2.5}$ is based on eight species. This implies differences in the composition of $PM_{2.5}$ across some models. Nonetheless, I prefer to focus on actual $PM_{2.5}$, as opposed to the alternative approach whereby $PM_{2.5}$ is approximated by Eq. [1] from the manuscript. I find that this approximation can affect the $PM_{2.5}$ response, and the corresponding model agreement (Figure 2.5 and 2.6).

Model	$PM_{2.5}$ Data Available		Resolution			References
	Present	Future	Lon	Lat	Lev	
GFDL-AM3	2002-2010	2101- 2110	144	90	48	Donner et al 2011
MIROC-CHEM	2000-2004	2100-2104	128	63	80	Watanabe et al 2011
GISS-E2-R*	1995-2005	2100	144	90	40	Shindell et al 2013
NCAR-CAM3.5	2002-2009	2102-2109	144	96	26	Lamarque et al 2012
HadGEM2	2000-2009	2100-2109	192	145	38	Collins et al 2011
CAM4	2000-2009	2100-2109	144	96	26	Neale Richard B 2010
CAM5	2000-2009	2100-2109	144	96	26	Neale Richard B 2010

* Note that the future $PM_{2.5}$ mass mixing ratio from the GISS model is available in only one year, whereas present-day data is available for multiple years. I find that the change in $PM_{2.5}$ depends on what years I select for the present-day simulation. For instance, a decrease in $PM_{2.5}$ occurs over North America when I select the year 1995 or 2000. On the contrary, $PM_{2.5}$ concentration increases over the same region when I select the year 2005. In this study, I use the mean of 11 years of present-day data to obtain present-day $PM_{2.5}$ concentration, which should yield a better estimate of the present-day GISS-E2-R climatology.

Thus, in most models, $PM_{2.5}$ is based on six species. However, in CAM4, no SOA is included, so $PM_{2.5}$ is based on five species. In GFDL-AM3 and GISS-E2-R, ammonium sulfate (NH_4) and nitrate (NO_3) are also included, so $PM_{2.5}$ is based on eight species. This implies differences in the composition of $PM_{2.5}$ across some models. I prefer to focus on actual $PM_{2.5}$, as opposed to the alternative approach whereby $PM_{2.5}$ is approximated by Eq. [1] for all models [e.g., *Silva et al.,* 2017]. Although the use of Eq. [1] supplies $PM_{2.5}$ with uniform composition across all models, it is an approximation to the actual $PM_{2.5}$, and as such, differences can arise. I find, for example, that this approximation can affect the $PM_{2.5}$ response, and the corresponding model agreement (Section 3.1).

I estimate premature mortality associated with changes in $PM_{2.5}$ concentration due to climate change using health impact functions Eq. [2] [*Anenberg et al.,* 2010; *Silva et al.,* 2013].

$$\Delta Mort = Mort_{base}(1-e^{-\beta\Delta\chi})Pop \qquad \text{Eq. [2]}$$

where $Mort_{base}$ is the baseline mortality rate, β is concentration-response factor (CRF), Δx is the change in $PM_{2.5}$ concentration between the present and future climate, and *Pop* is the exposed population in the year 2100 (Figure 2.1). Baseline mortality rate and β values are obtained from *Silva et al.* [2013]. β is estimated from the slope of the log linear relation between $PM_{2.5}$ concentration and relative risk (RR) [*Anenberg et al.,* 2010;

Krewski et al., 2009; *Silva et al.,* 2013]. Moreover, estimation of β considers the population age 30 and above [*Krewski et al.,* 2009; *Silva et al.,* 2013].

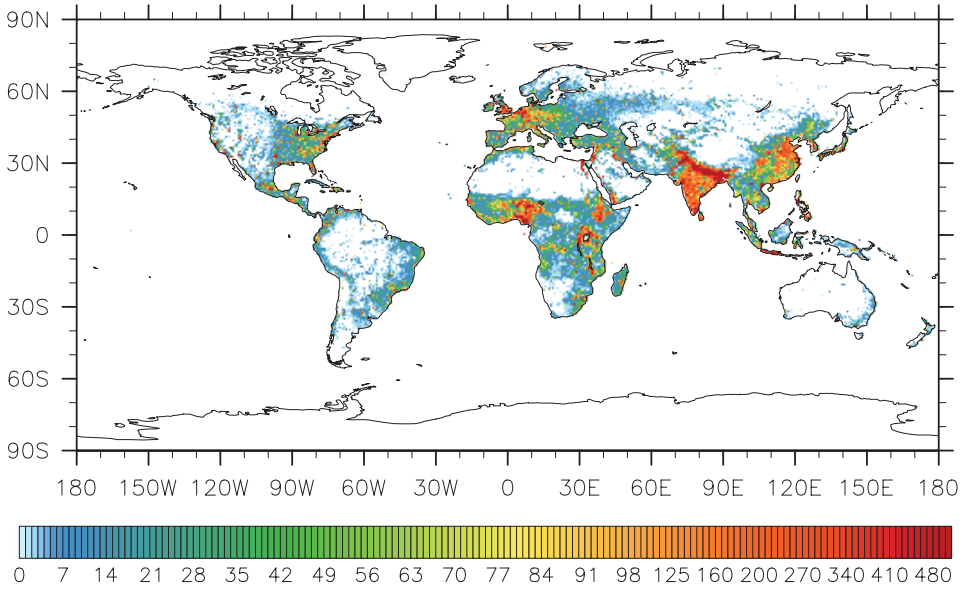

Figure 2.1 Spatial distribution of exposed population age 30 and above for the year 2100 from the SSP5 population scenario (units: people/km^2). The other SSPs yield similar spatial patterns, but with different magnitudes (Table 2.2).

To calculate premature mortality associated with future changes in $PM_{2.5}$, an estimate of future (year 2100) population age 30 and above is required. Three datasets are used to estimate this quantity: present-day (2014) population for all ages from LandScan [*Bhaduri et al.,* 2012]; country-level present-day total population age 30 and over from United Nation's (UN) Department of Economic and Social Affairs (data available at https://esa.un.org/unpd/wpp/Download/Standard/Population/); and country-level projected (year 2100) total population age 30 and over from the Shared Socioeconomic

Pathways (SSPs) scenario database. LandScan present-day population for all ages is provided at < 1km^2 spatial resolution. However, the UN and SSP population datasets provide country-level estimates. Therefore I unify all population datasets to a spatial resolution of 0.5º by 0.5º using ArcGIS 10.3 resample tool.

The SSPs characterize five possible future development pathways derived from different assumptions on society's capability to mitigate and/or adapt to climate change [*O'Neill et al.,* 2014; *Samir and Wolfgang*. 2017]. These include sustainability (SSP1), middle of the road (SSP2), fragmentation (SSP3), inequality (SSP4), and conventional development (SSP5). The SSP5 scenario represents the development of fossil fuels, which is similar to RCP8.5. The SSP populations are projected with alternative fertility, mortality, migration, and education levels, which is dependent on the country [*Samir and Wolfgang*. 2017].

Table 2.2 Future population estimates age 30 and above for the five SSPs in 10 world regions (units: billions of people). The ten world regions are identical to those in Figure S5 from Silva *et al.* [2013]. The mean value column represents the average across the five scenarios.

Scenario / Regions	SSP1	SSP2	SSP3	SSP4	SSP5	Mean
North America	0.51	0.53	0.46	0.46	0.64	0.52
South America	0.28	0.33	0.41	0.27	0.27	0.31
Europe	0.57	0.56	0.36	0.46	0.75	0.54
Africa	1.34	1.53	1.81	1.76	1.30	1.55
Middle East	0.64	0.79	1.02	0.87	0.62	0.79
Former Soviet Union	0.16	0.19	0.21	0.15	0.17	0.18
India	1.55	1.87	2.40	1.47	1.54	1.76
East Asia	0.71	0.74	0.79	0.58	0.73	0.71
South East Asia	0.35	0.39	0.46	0.34	0.34	0.38
Australia	0.03	0.03	0.02	0.03	0.04	0.03
Total	6.1	7.0	7.9	6.4	6.4	6.8

The total future population age 30 and above from each scenario ranges between approximately 6.1 and 7.9 billion with SSP1 and SSP3, respectively (Table 2.2). Moreover, among ten world regions, the largest (smallest) increase in future population age 30 and above, averaged over the five scenarios, occurs in India (Australia) at 1.76 (0.03 billion). Figure 2.2 shows the change in population age 30 and above (2100 minus present day) for each SSP. Notable population increases exist in all SSPs in several regions, including western/central Africa and India. In contrast, Eastern Europe and China show decreases in future population age 30 and above. Furthermore, the largest population increase occurs over India, particularly based on SSP3.

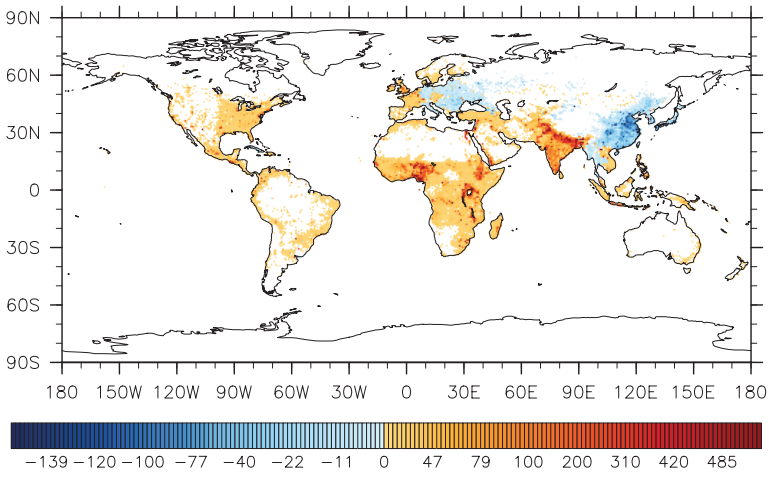
90N
60N
30N
0
30S
60S
90S
180 150W 120W 90W 60W 30W 0 30E 60E 90E 120E 150E 180
−139 −120 −100 −77 −40 −22 −11 0 47 79 100 200 310 420 485

(a)

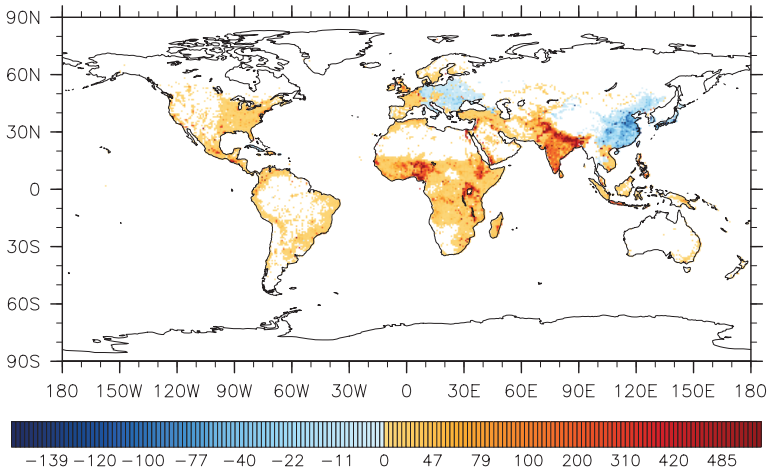
90N
60N
30N
0
30S
60S
90S
180 150W 120W 90W 60W 30W 0 30E 60E 90E 120E 150E 180
−139 −120 −100 −77 −40 −22 −11 0 47 79 100 200 310 420 485

(b)

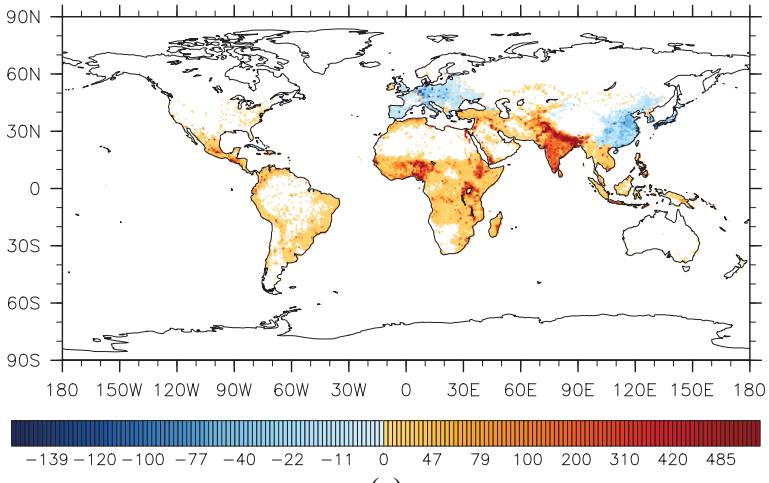
90N
60N
30N
0
30S
60S
90S
180 150W 120W 90W 60W 30W 0 30E 60E 90E 120E 150E 180
−139 −120 −100 −77 −40 −22 −11 0 47 79 100 200 310 420 485

(c)

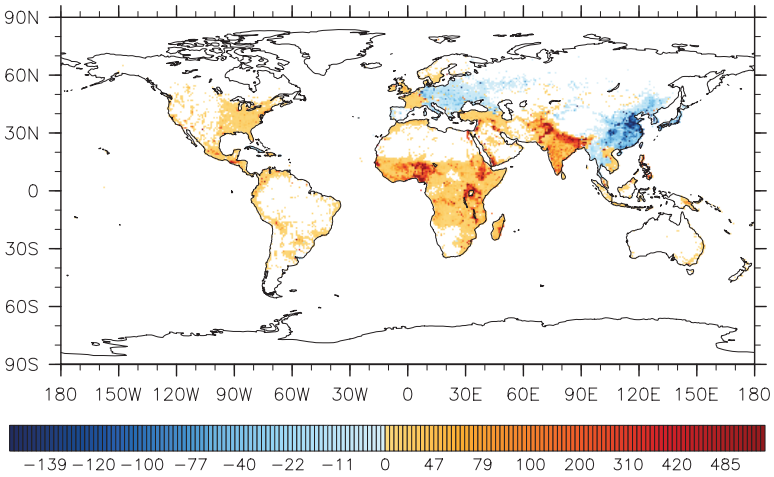

(d)

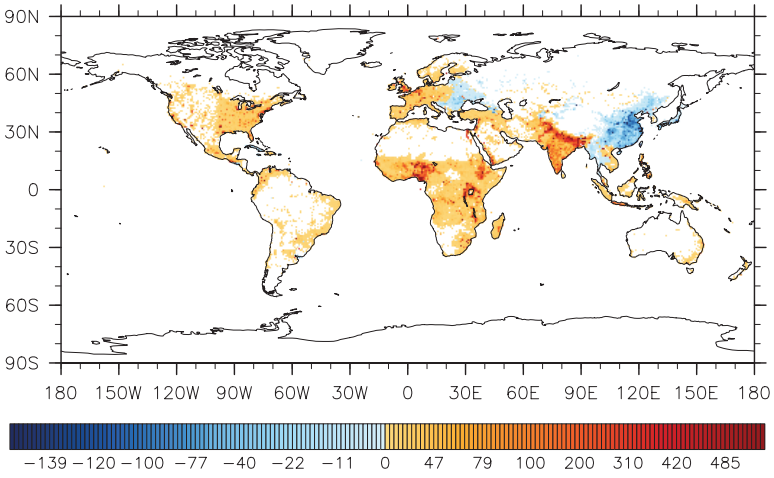

(e)

Figure 2.2 Spatial maps of differences in population age 30 and over between present-day (the year 2014) and projected future population using a) SSP1, b) SSP2, c) SSP3, d) SSP4, and e) SSP5 (units: people/km^2).

Our approach has two assumptions: 1) the ratio of population age 30 and above to total population is uniformly distributed within each country, and 2) the spatial distribution of future population is identical to the present-day spatial distribution within each country. I note that these assumptions are over simplifications, since world population forecasts indicate an increase in the percentage of urban population (so the spatial distribution of future population in urban areas will not be the same as present-day). I also note that most anthropogenic aerosol emissions—major components of $PM_{2.5}$—occur in urban areas. Furthermore, world population forecasts indicate an increase in life expectancy and median age, implying a larger proportion of people age 30 and above in the future, relative to the present-day. Both of these factors likely imply that I may underestimate the human health risks associated with future changes in $PM_{2.5}$ in a warmer world.

I first calculate the country-level ratio of population 30 and above in the present-day, by dividing population age 30 and above by the total population within each country. This ratio is multiplied by the present–day all ages population in each grid box for each country (first assumption), yielding the present-day population age 30 and above in each grid box using ArcGIS 10.3 raster calculator tools. I obtain the ratio of population age 30 and above in the present-day for each grid box by dividing population age 30 and above in each grid box by the total population age 30 and above within each country. Finally, I multiply the ratio to the projected future population age 30 and above to quantify the future population age 30 and above in each grid box (second assumption). I show the estimated future spatial distribution of population age 30 and above based on SSP5

(Figure 2.1). Note that the increase in population implies more people will be exposed to $PM_{2.5}$.

2.3. Results

2.3.1 Changes in surface $PM_{2.5}$ concentration

The majority of models (at least five of the seven) yield an increase in global annual mean surface $PM_{2.5}$ attributable to GHG-induced warming (Table 2.3). In fact, six of the seven models yield an increase in global mean $PM_{2.5}$, with a model mean increase of 0.43 $\mu g/m^3$ and a range from -0.25 $\mu g/m^3$ (CAM4) to 1.71 $\mu g/m^3$ (MIROC-CHEM). Moreover, five of the seven models indicate an increase in $PM_{2.5}$ in nine of the ten world regions (Africa being the exception). The largest increase in $PM_{2.5}$, averaged over the seven models, occurs over India at 1.5 $\mu g/m^3$, with six of the seven models agreeing on the increase. Similarly, the largest decrease in $PM_{2.5}$ occurs over Africa at -0.9 $\mu g/m^3$, with five of the seven models agreeing on the decrease.

A relatively large increase in $PM_{2.5}$ (more than 3 $\mu g/m^3$) occurs over several areas (Figure 2.3), including western Australia, northern Africa, North America, India, and East China. Most of the decrease in $PM_{2.5}$ concentration occurs over the oceans and parts of Africa—particularly in five models including GISS-E2-R, NCAR-CAM3.5, HadGEM2, CAM4, and CAM5.

Table 2.3 Annual mean changes in surface $PM_{2.5}$ concentration ($\mu g/m^3$) by region and model.

	NAI	GFDL-AM3	MIROC-CHEM	GISS-E2-R	NCAR-CAM3.5	HadGEM2	CAM4	CAM5
North America	6	0.67	0.37	0.19	0.55	0.07	0.54	-0.11
South America	6	0.31	1.02	0.80	-0.82	0.46	0.97	0.18
Europe	5	0.50	0.02	-0.23	0.19	0.33	-0.10	0.20
Africa	2	0.48	1.52	-1.77	-2.27	-1.67	-2.07	-0.35
Middle East	5	1.21	2.99	2.99	0.69	-1.48	-3.38	0.22
Former Soviet Union	6	0.44	0.41	0.92	-0.29	0.07	0.70	0.25
India	6	1.19	8.00	2.50	0.95	-2.80	0.27	0.26
East Asia	5	1.08	1.08	-0.13	1.04	0.28	0.13	-0.05
South East Asia	5	0.93	0.56	-0.27	0.71	0.18	0.32	-0.30
Australia	6	0.40	1.12	0.09	1.13	5.65	0.15	-0.14
Mean Over 10 World Regions	6	0.72	1.71	0.51	0.19	0.11	-0.25	0.02

* NAI: Number of models that agree on an increase in annual $PM_{2.5}$ concentration

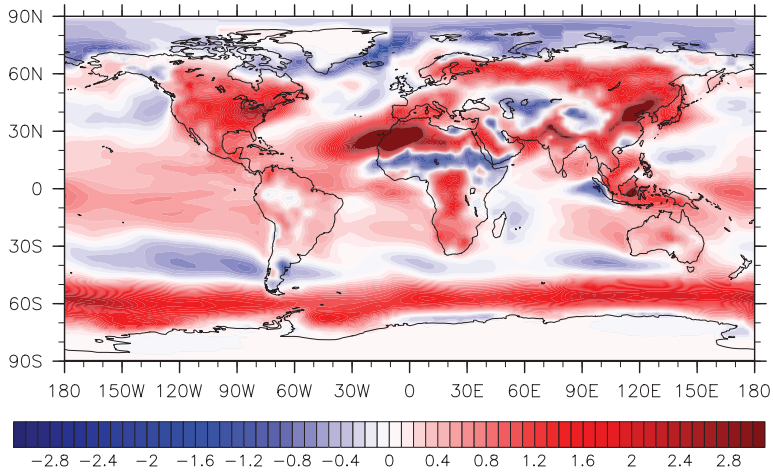
90N
60N
30N
0
30S
60S
90S
180 150W 120W 90W 60W 30W 0 30E 60E 90E 120E 150E 180
−2.8 −2.4 −2 −1.6 −1.2 −0.8 −0.4 0 0.4 0.8 1.2 1.6 2 2.4 2.8

(a)

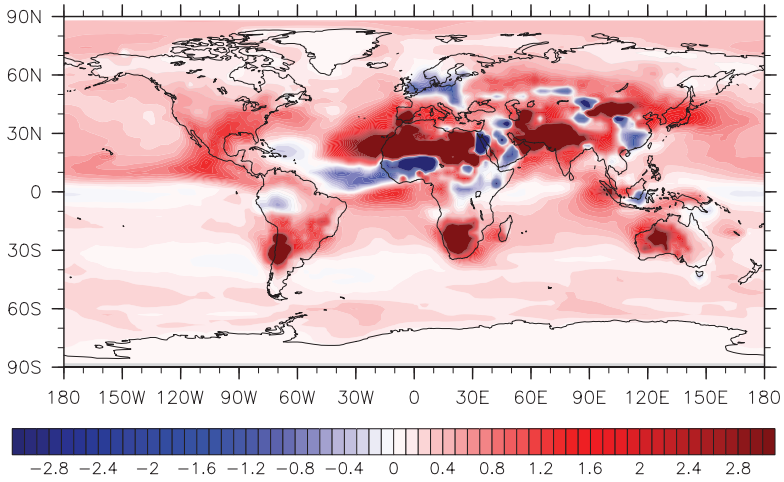
90N
60N
30N
0
30S
60S
90S
180 150W 120W 90W 60W 30W 0 30E 60E 90E 120E 150E 180
−2.8 −2.4 −2 −1.6 −1.2 −0.8 −0.4 0 0.4 0.8 1.2 1.6 2 2.4 2.8

(b)

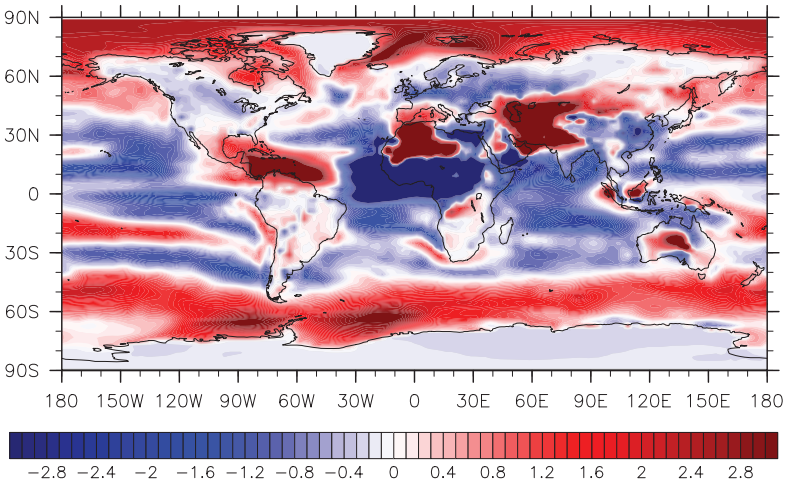
90N
60N
30N
0
30S
60S
90S
180 150W 120W 90W 60W 30W 0 30E 60E 90E 120E 150E 180
−2.8 −2.4 −2 −1.6 −1.2 −0.8 −0.4 0 0.4 0.8 1.2 1.6 2 2.4 2.8

(c)

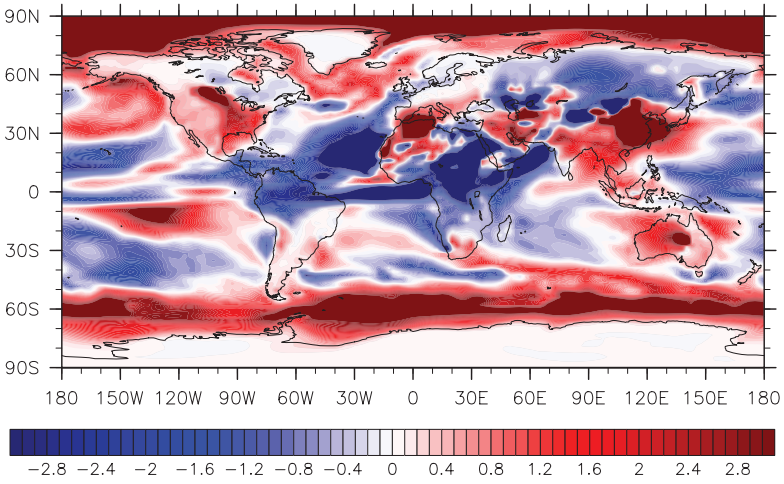
90N
60N
30N
0
30S
60S
90S
180 150W 120W 90W 60W 30W 0 30E 60E 90E 120E 150E 180
−2.8 −2.4 −2 −1.6 −1.2 −0.8 −0.4 0 0.4 0.8 1.2 1.6 2 2.4 2.8

(d)

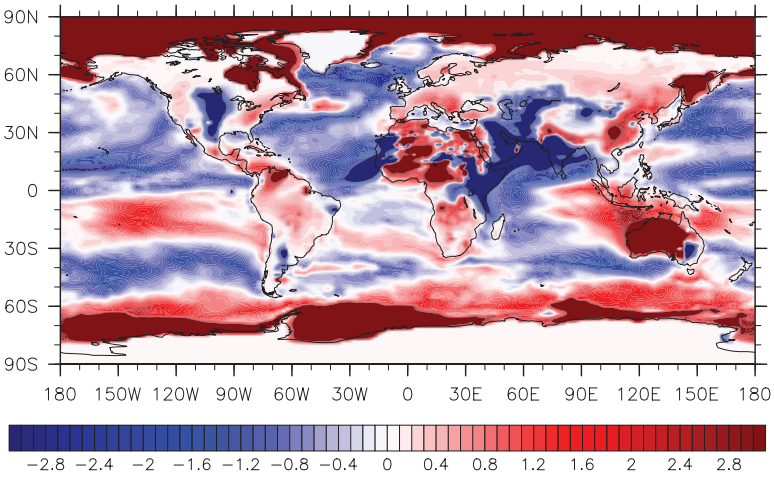
90N
60N
30N
0
30S
60S
90S
180 150W 120W 90W 60W 30W 0 30E 60E 90E 120E 150E 180
−2.8 −2.4 −2 −1.6 −1.2 −0.8 −0.4 0 0.4 0.8 1.2 1.6 2 2.4 2.8

(e)

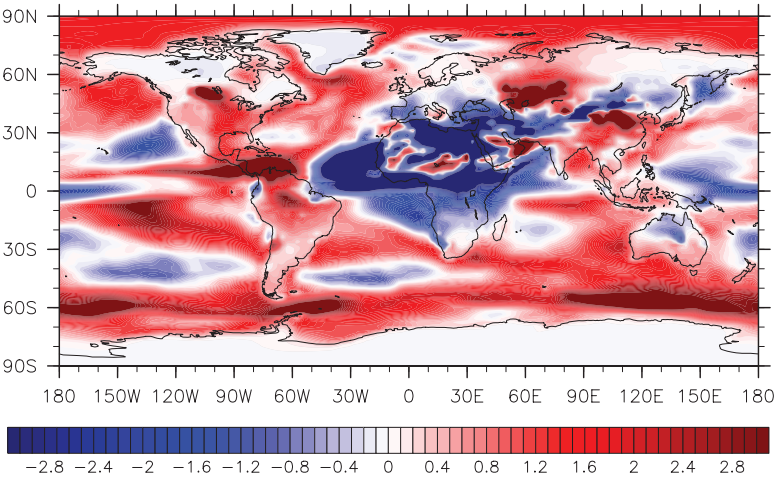
90N
60N
30N
0
30S
60S
90S
180 150W 120W 90W 60W 30W 0 30E 60E 90E 120E 150E 180
−2.8 −2.4 −2 −1.6 −1.2 −0.8 −0.4 0 0.4 0.8 1.2 1.6 2 2.4 2.8

(f)

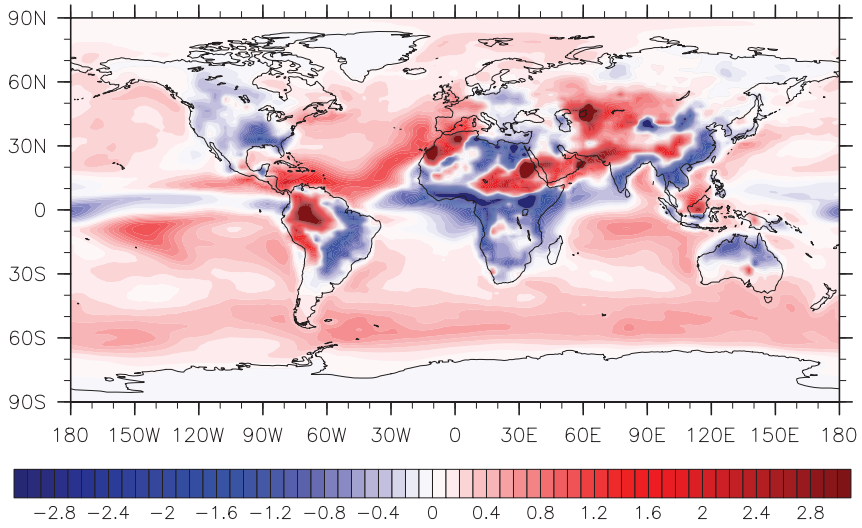

(g)

Figure 2.3 Annual mean $PM_{2.5}$ surface concentration change (units: $\mu g/m^3$) between 2100 and 2000 from a) GFDL-AM3, b) MIROC-CHEM, c) GISS-E2-R, d) NCAR-CAM3.5, e) HadGEM2, f) CAM4, and g) CAM5.

Figure 2.4 shows the number of models that agree on an increase in annual mean $PM_{2.5}$ concentration over the continents at the end of the 21st century. Most land areas show at least four models agree on an increase in $PM_{2.5}$. Moreover, at least five models agree on elevated $PM_{2.5}$ over many locations, such as northern India, Western Europe, Australia, and the eastern United States. These results suggest that business-as-usual GHG-induced warming is likely associated with an increase in surface $PM_{2.5}$ concentration over most land regions.

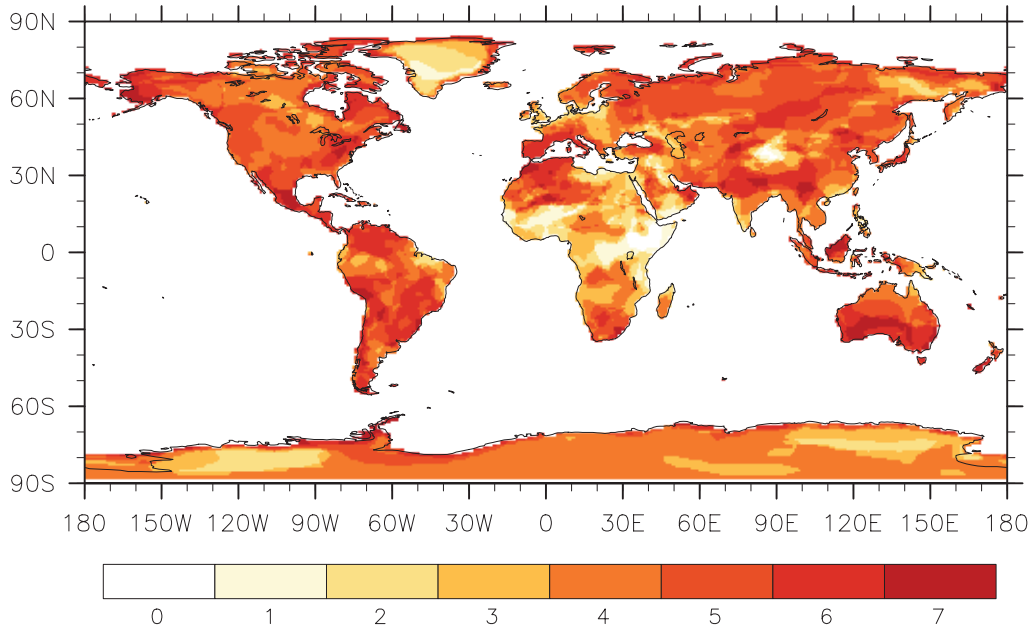

Figure 2.4 Number of models that yield elevated annual mean $PM_{2.5}$ concentration over the continents at the end of the 21st century.

Although our $PM_{2.5}$ results are similar to *Silva et al.* [2017], subtle differences do exist, including a slight reduction in model agreement based on our analysis, relative to *Silva et al.* [2017]. Part of this difference is due to our use of two additional models (CAM4/5). CAM5, for example, yields decreases in $PM_{2.5}$ over several regions, including North America, Africa, East Asia, Southeast Asia, and Australia (Table 2.3).

Another source of the difference between these two analyses appears to be related to the definition of $PM_{2.5}$. As previously noted, I use actual (i.e., archived) $PM_{2.5}$ in all but one model. The exception is HadGEM2 (which lacks archived $PM_{2.5}$), where Eq. [1] is used to approximate $PM_{2.5}$. *Silva et al.* [2017] use Eq. [1], with the addition of ammonium sulfate, for all five ACCMIP models. I reproduce $PM_{2.5}$ model agreement—using only the ACCMIP models that *Silva et al.* [2017] use—based on approximating $PM_{2.5}$ as the sum of six species [Eq. 1] (ammonium sulfate is not included, despite its inclusion in *Silva et al.* [2017], since this data is not publically available for all models). When approximated as the sum of six species, I find that more ACCMIP models agree on an increase in $PM_{2.5}$ over several regions, including North America, western and central Africa, and Europe (Figure 2.5).

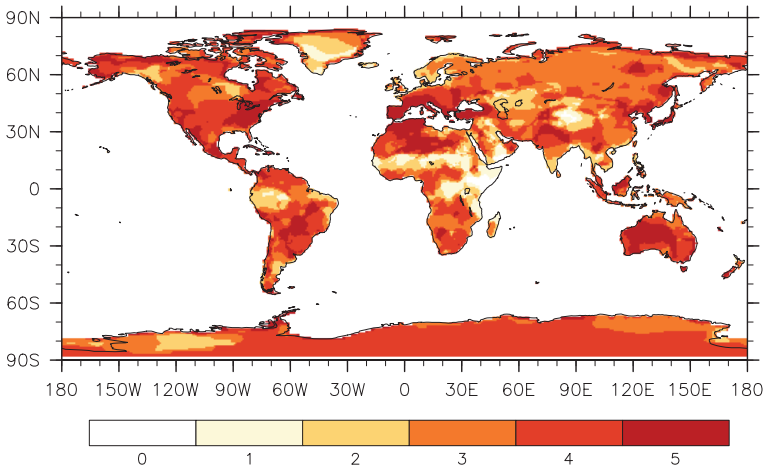
90N
60N
30N
0
30S
60S
90S
180 150W 120W 90W 60W 30W 0 30E 60E 90E 120E 150E 180
0 1 2 3 4 5

(a)

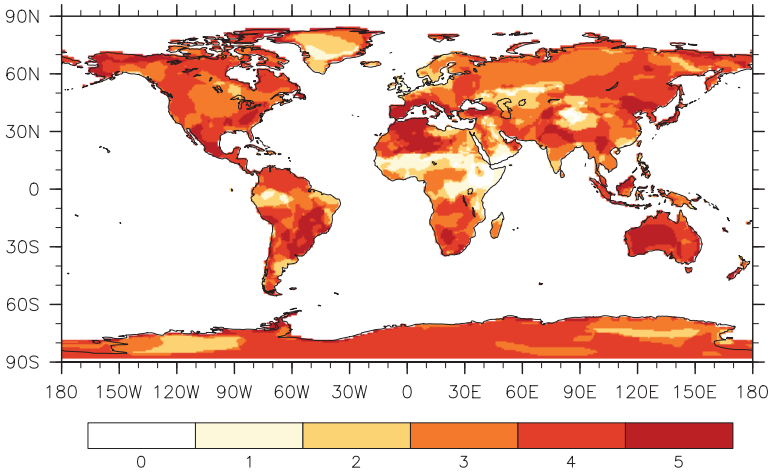
90N
60N
30N
0
30S
60S
90S
180 150W 120W 90W 60W 30W 0 30E 60E 90E 120E 150E 180
0 1 2 3 4 5

(b)

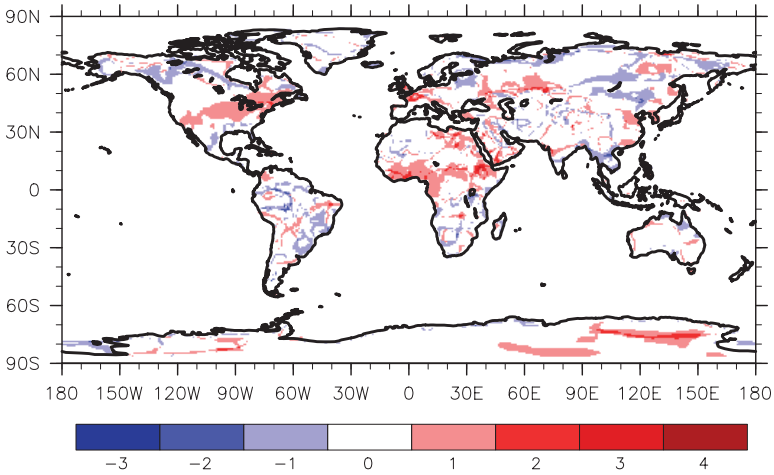
90N
60N
30N
0
30S
60S
90S
180 150W 120W 90W 60W 30W 0 30E 60E 90E 120E 150E 180
−3 −2 −1 0 1 2 3 4

(c)

Figure 2.5 Number of ACCMIP models that agree on an increase in $PM_{2.5}$ at end of the 21st century with a) $PM_{2.5}$ approximated as the sum of six species (Eq. [1] from the manuscript), b) archived $PM_{2.5}$ and c) the difference between the sum of six species and archived $PM_{2.5}$ (a - b). Defining $PM_{2.5}$ as the sum of six species yields larger model agreement on an increase in $PM_{2.5}$ in several regions, including North America and Europe.

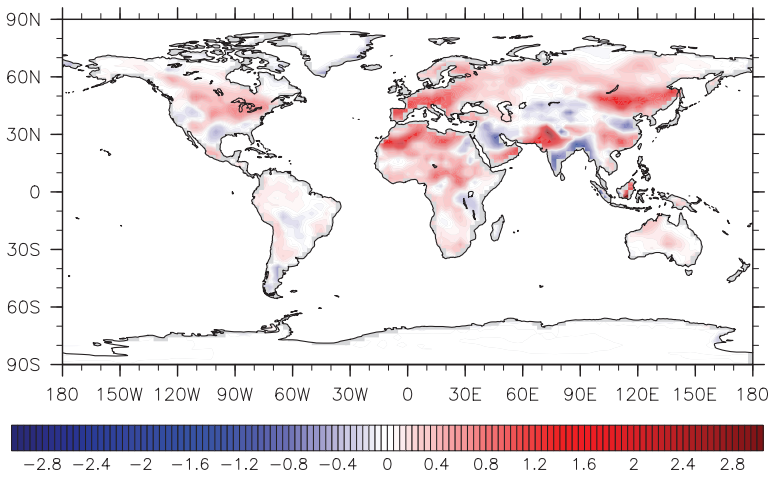
90N
60N
30N
0
30S
60S
90S
180 150W 120W 90W 60W 30W 0 30E 60E 90E 120E 150E 180
−2.8 −2.4 −2 −1.6 −1.2 −0.8 −0.4 0 0.4 0.8 1.2 1.6 2 2.4 2.8

(a)

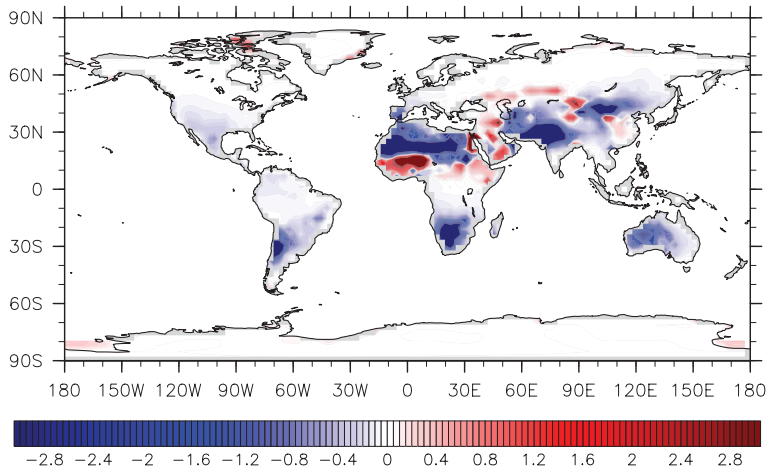
90N
60N
30N
0
30S
60S
90S
180 150W 120W 90W 60W 30W 0 30E 60E 90E 120E 150E 180
−2.8 −2.4 −2 −1.6 −1.2 −0.8 −0.4 0 0.4 0.8 1.2 1.6 2 2.4 2.8

(b)

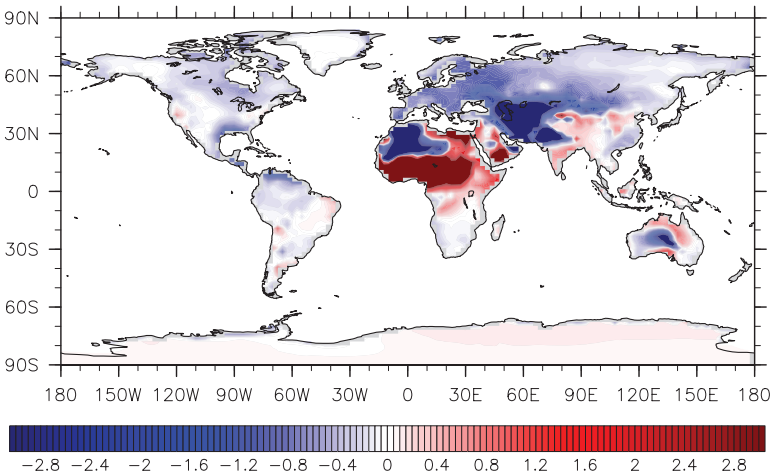
90N
60N
30N
0
30S
60S
90S
180 150W 120W 90W 60W 30W 0 30E 60E 90E 120E 150E 180
−2.8 −2.4 −2 −1.6 −1.2 −0.8 −0.4 0 0.4 0.8 1.2 1.6 2 2.4 2.8

(c)

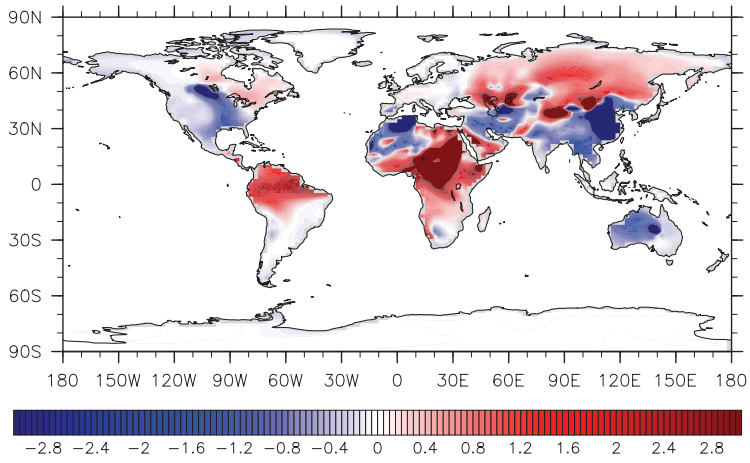
90N
60N
30N
0
30S
60S
90S
180 150W 120W 90W 60W 30W 0 30E 60E 90E 120E 150E 180
−2.8 −2.4 −2 −1.6 −1.2 −0.8 −0.4 0 0.4 0.8 1.2 1.6 2 2.4 2.8

(d)

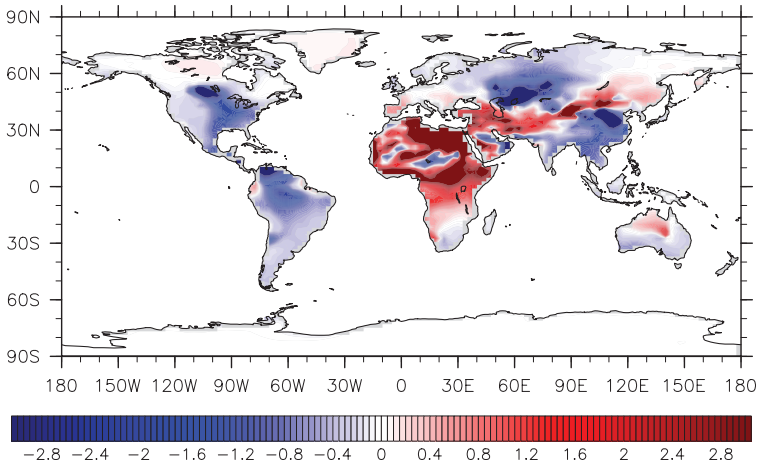
90N
60N
30N
0
30S
60S
90S
180 150W 120W 90W 60W 30W 0 30E 60E 90E 120E 150E 180
−2.8 −2.4 −2 −1.6 −1.2 −0.8 −0.4 0 0.4 0.8 1.2 1.6 2 2.4 2.8

(e)

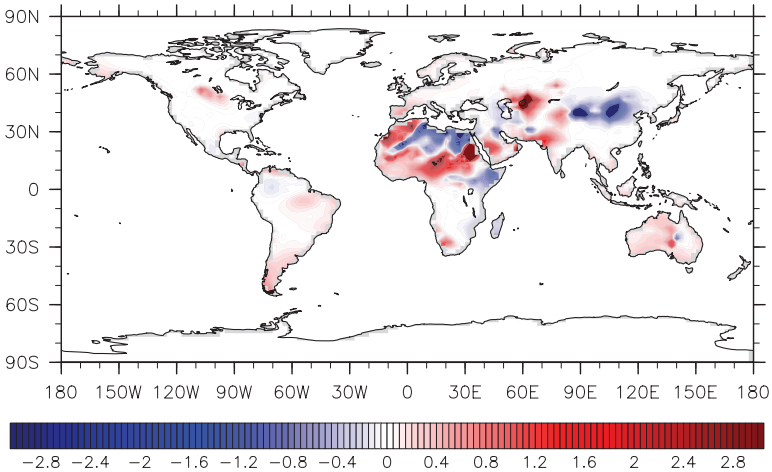
90N
60N
30N
0
30S
60S
90S
180 150W 120W 90W 60W 30W 0 30E 60E 90E 120E 150E 180
−2.8 −2.4 −2 −1.6 −1.2 −0.8 −0.4 0 0.4 0.8 1.2 1.6 2 2.4 2.8

(f)

Figure 2.6 The $PM_{2.5}$ response difference ($DPM_{2.5}$ estimated as the sum of species minus actual $DPM_{2.5}$) for a) GFDL-AM3, b) MIROC-CHEM, c) GISS-E2-R, d) NCAR-CAM3.5, e) CAM4, and f) CAM5. GFDL-AM3 and GISS-E2-R are based on 8 species (BC + OA + SO_4 + SOA + 0.25*SS + 0.1*Dust + NO_3 + NH_4); the other models are based on 6 species (no NO_3/NH_4), except CAM4 which is based on 5 species (no NO_3/NH_4/SOA). For each model, approximating $PM_{2.5}$ as the sum of species yields discrepancies in the $PM_{2.5}$ response, relative to actual $PM_{2.5}$, in most regions. HadGEM2 results are not shown, since archived $PM_{2.5}$ does not exist for this model.

A more like for like comparison is obtained by approximating $PM_{2.5}$ with Eq. [1] using the exact same aerosol species that constitute archived $PM_{2.5}$ (i.e., 8 species for GFDL-AM3 and GISS-E2-R and 6 species for the other models, except CAM4 which is based on 5 species). When $PM_{2.5}$ is approximated as the sum of individual aerosol species, most regions yield discrepancies in the $PM_{2.5}$ response, relative to actual $PM_{2.5}$ (Figure 2.6).

I note that *Silva et al.* [2017] also attempts to quantify the effect of approximating $PM_{2.5}$ as the sum of species relative to actual $PM_{2.5}$, and they too find some differences. For example, global premature mortality appears to decrease slightly in most models when $PM_{2.5}$ is approximated, especially in MIROC-CHEM, which is consistent with a smaller increase in approximated $PM_{2.5}$ (weighted by exposed future population), relative to actual $PM_{2.5}$. I obtain qualitatively similar results (Figure 2.6b). Despite these differences, however, our results are very similar to *Silva et al.* [2017]—the majority of models yield a $PM_{2.5}$ increase in all world regions except Africa.

2.3.2 Effects of $PM_{2.5}$ changes on premature mortality

Estimated premature mortality due to lung cancer (LC) and cardiopulmonary disease (CPD) associated with the change in $PM_{2.5}$ indicates a robust increase. The majority of models (four of the seven) indicate elevated premature mortality in nine of the ten world regions (Figure 2.7; Table 2.4). Moreover, stronger inter-model agreement (at least five models) occurs over eight of the ten regions (Africa and Australia are the exceptions).

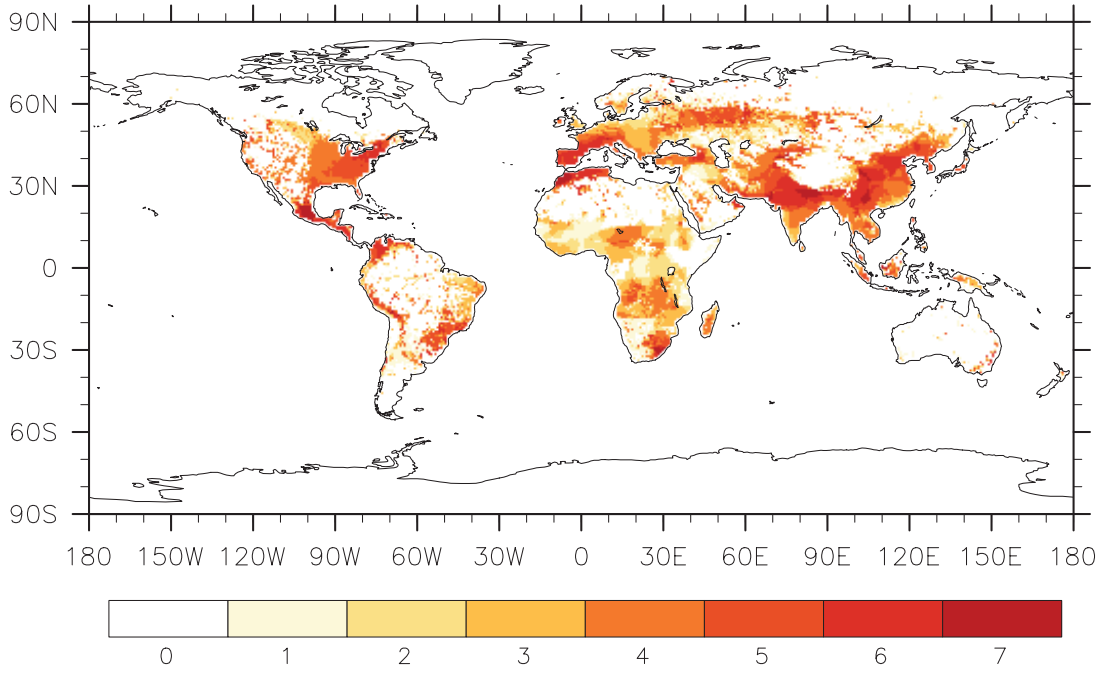

Figure 2.7 Number of models that yield an increase in premature mortality at the end of the 21st century (SSP5 scenario).

These results are consistent with the strong inter-model agreement that surface $PM_{2.5}$ concentrations will increase in these regions (Table 2.3). On the contrary, all models indicate a decrease in premature deaths over Africa across all future population scenarios (Table 2.4). Figure 2.8 shows the spatial distribution of premature mortality for each of the seven models. The majority of models yield a decrease in premature deaths over central and western Africa, and increases in premature deaths over the eastern United States, southwestern Europe, northern India, Australia, and east China.

Table 2.4 Annual mean premature mortality (deaths/10000 km^2) for both lung cancer (LC) and cardiopulmonary disease (CPD) by region, model, and future-population scenario. Over Australia, <1 indicates a small increase in premature mortality (0 < deaths/10000 km^2 < 1) and <0 indicates a small decrease in premature mortality (-1 < deaths/10000 km^2 < 0).

Regions / Models		North America	South America	Europe	Africa	Middle East	Former Soviet Union	India	East Asia	South East Asia	Australia
	NAI_{PM}	5	5	5	0	5	5	6	5	5	4
GFDL-AM3	SSP1	17	2	35	-2	43	2	537	61	43	<1
	SSP2	17	3	35	-4	54	2	649	64	47	<1
	SSP3	12	3	22	-6	71	2	835	71	54	<1
	SSP4	14	2	29	-6	64	2	515	50	37	<1
	SSP5	23	2	47	-2	41	2	535	61	42	<1
	Mean	17	3	34	-4	54	2	614	62	45	<1
MIROC-CHEM	SSP1	10	6	16	-30	261	6	1689	10	42	<1
	SSP2	10	8	16	-39	336	7	2040	11	47	<1
	SSP3	8	9	10	-51	448	8	2622	11	54	<1
	SSP4	8	6	14	-50	427	5	1607	8	37	<1
	SSP5	12	6	21	-29	247	6	1681	10	41	<1
	Mean	10	7	15	-40	344	6	1928	10	44	<1
GISS-E2-R	SSP1	1	2	-20	-193	165	16	526	-37	-11	<1
	SSP2	1	2	-19	-225	217	18	636	-39	-13	<1
	SSP3	2	2	-12	-270	291	25	819	-44	-16	<1
	SSP4	1	1	-15	-265	281	14	503	-31	-10	<1
	SSP5	0	2	-26	-189	154	13	525	-37	-10	<1
	Mean	1	2	-18	-229	222	17	602	-38	-12	<1

NCAR-CAM3.5	SSP1	13	-3	20	-82	12	-0.10	503	160	74	0
	SSP2	13	-4	20	-95	14	-0.06	607	168	82	<0
	SSP3	9	-5	13	-111	21	0.67	780	185	94	<0
	SSP4	11	-3	17	-110	19	-0.04	478	131	65	<0
	SSP5	18	-3	26	-81	11	-0.61	500	160	73	<1
	Mean	13	-4	19	-96	15	-0.03	574	161	77	<0
HadGEM2	SSP1	-3	2	25	-37	-59	-3	-315	42	23	<1
	SSP2	-2	3	25	-44	-76	-4	-380	44	25	<1
	SSP3	0	3	17	-57	-107	-5	-486	49	28	<1
	SSP4	-2	2	21	-55	-112	-3	-286	34	20	<1
	SSP5	-4	2	33	-35	-61	-3	-314	42	23	<1
	Mean	-2	2	24	-46	-83	-3	-356	42	24	<1
CAM4	SSP1	12	4	-18	-56	-100	2	191	46	18	<0
	SSP2	12	5	-18	-65	-122	2	230	49	20	<0
	SSP3	9	6	-12	-77	-159	2	295	54	23	<0
	SSP4	10	4	-15	-75	-123	1	181	38	16	<0
	SSP5	15	4	-24	-54	-95	2	189	47	18	<0
	Mean	11	5	-18	-65	-120	2	217	47	19	<0
CAM5	SSP1	-3	0	21	-19	16	3	108	-12	-30	<0
	SSP2	-2	0	21	-21	22	4	131	-13	-34	<0
	SSP3	-1	0	12	-25	29	5	170	-14	-40	0
	SSP4	-2	0	17	-24	31	3	106	-10	-28	<0
	SSP5	-4	0	29	-18	15	3	108	-13	-30	<0
	Mean	-2	0	20	-21	22	4	125	-13	-32	<0

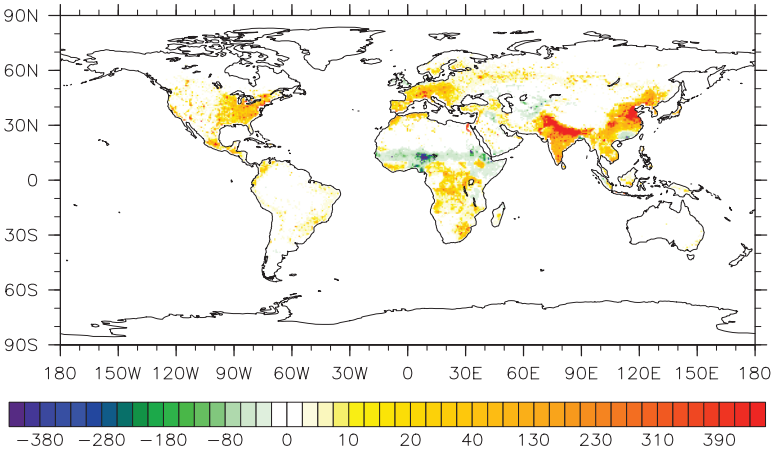
90N
60N
30N
0
30S
60S
90S
180 150W 120W 90W 60W 30W 0 30E 60E 90E 120E 150E 180
−380 −280 −180 −80 0 10 20 40 130 230 310 390

(a)

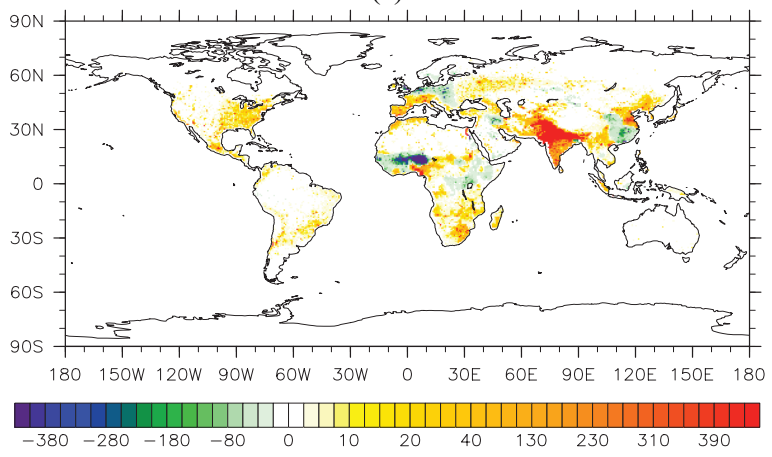
90N
60N
30N
0
30S
60S
90S
180 150W 120W 90W 60W 30W 0 30E 60E 90E 120E 150E 180
−380 −280 −180 −80 0 10 20 40 130 230 310 390

(b)

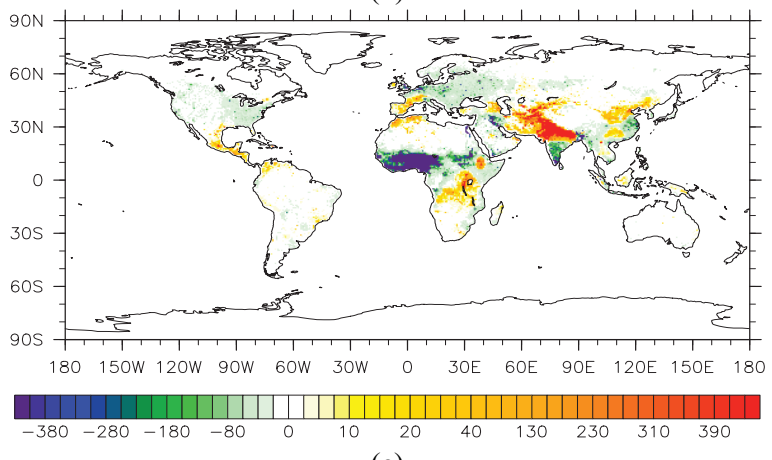
90N
60N
30N
0
30S
60S
90S
180 150W 120W 90W 60W 30W 0 30E 60E 90E 120E 150E 180
−380 −280 −180 −80 0 10 20 40 130 230 310 390

(c)

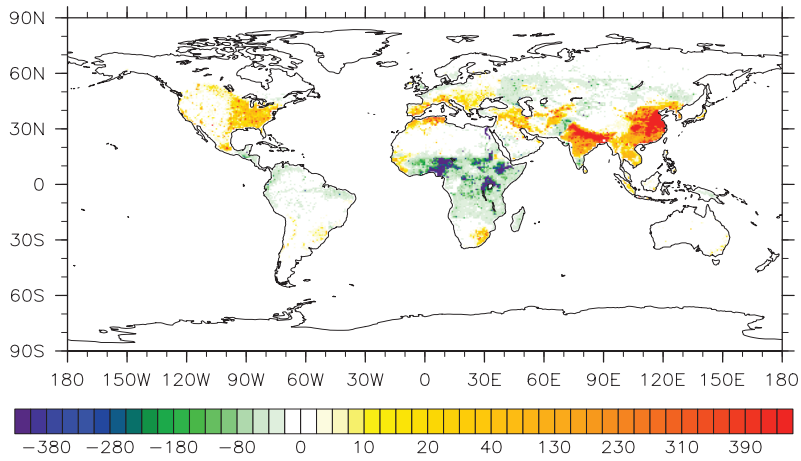
90N
60N
30N
0
30S
60S
90S
180 150W 120W 90W 60W 30W 0 30E 60E 90E 120E 150E 180
−380 −280 −180 −80 0 10 20 40 130 230 310 390

(d)

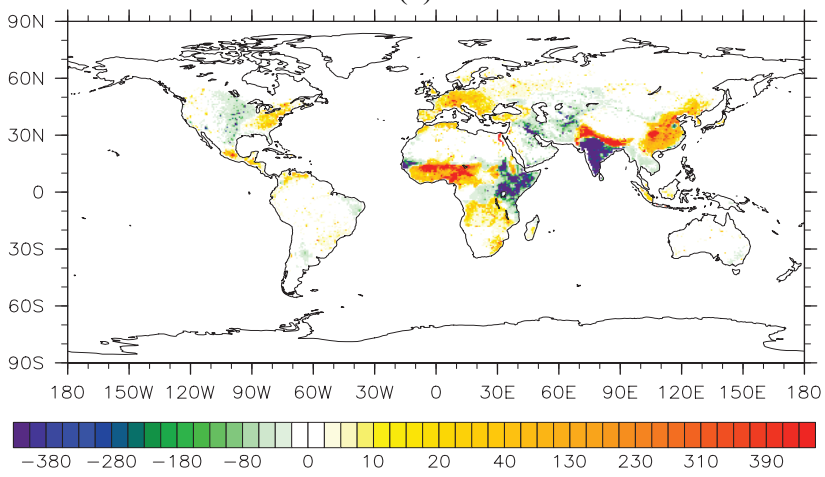
90N
60N
30N
0
30S
60S
90S
180 150W 120W 90W 60W 30W 0 30E 60E 90E 120E 150E 180
−380 −280 −180 −80 0 10 20 40 130 230 310 390

(e)

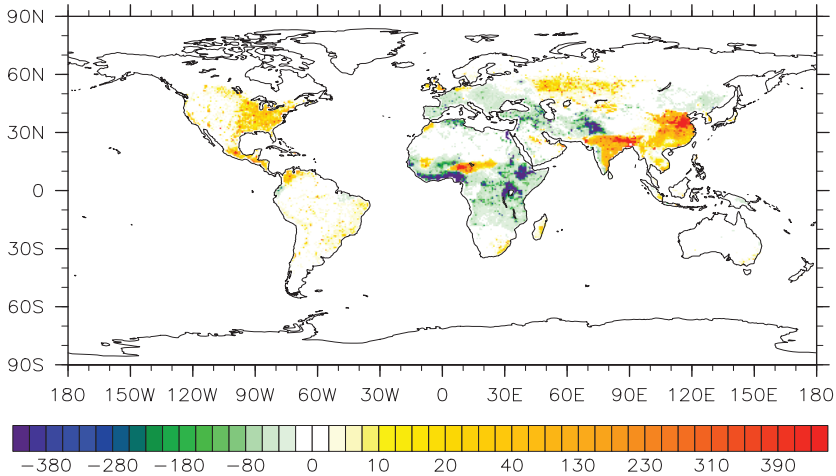
90N
60N
30N
0
30S
60S
90S
180 150W 120W 90W 60W 30W 0 30E 60E 90E 120E 150E 180
−380 −280 −180 −80 0 10 20 40 130 230 310 390

(f)

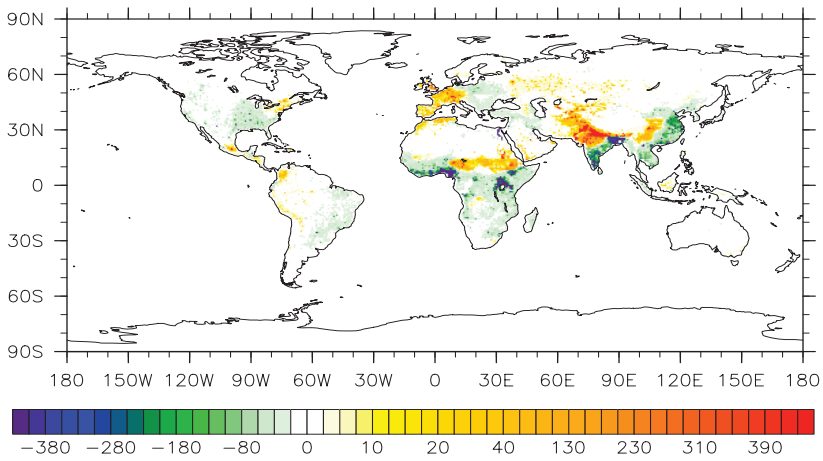

(g)

Figure 2.8 Annual premature mortality (SSP5 scenario) due to both LC and CPD in the year 2100 due to changes in $PM_{2.5}$ concentration from a) GFDL-AM3, b) MIROC-CHEM, c) GISS-E2-R, d) NCAR-CAM3.5, e) HadGEM2, f) CAM4, and g) CAM5 (units: deaths/10000 km^2). The other SSPs yield a similar spatial mortality distribution, but with different magnitudes (Table 2.4 and 2.5). White land areas indicate no exposed population.

Averaged over the seven models, the global average premature mortality increases in all future-population scenarios, with a model mean increase of 194,448 deaths/year. However, the magnitude varies depending on the SSP, ranging by a factor of ~2: from 143,704 deaths/year in SSP4 to 265,112 deaths/year in SSP3 (Figure 2.9). This range of future premature mortality due to GHG-induced changes in $PM_{2.5}$ covers the corresponding estimate of 215,000 deaths/year (based on four diseases) using projected future-population from the International Futures (IFs) integrated modeling system [*Silva et al.* 2017]. I note that model uncertainty, relative to future population uncertainty, is the dominant source of ambiguity in premature deaths. Compared to the factor of ~2 uncertainty due to SSP (143,704 versus 265,112 global deaths/year), the uncertainty due to the model ranges from -249,976 deaths/year in HadGEM2 to 1,043,850 million deaths/year in MIROC-CHEM (averaged over SSP for each model). This is qualitatively similar to *Silva et al.* [2017], although they find a smaller range in model uncertainty for global premature deaths (based on four diseases and IF future population) at -76,100 to 595,000.

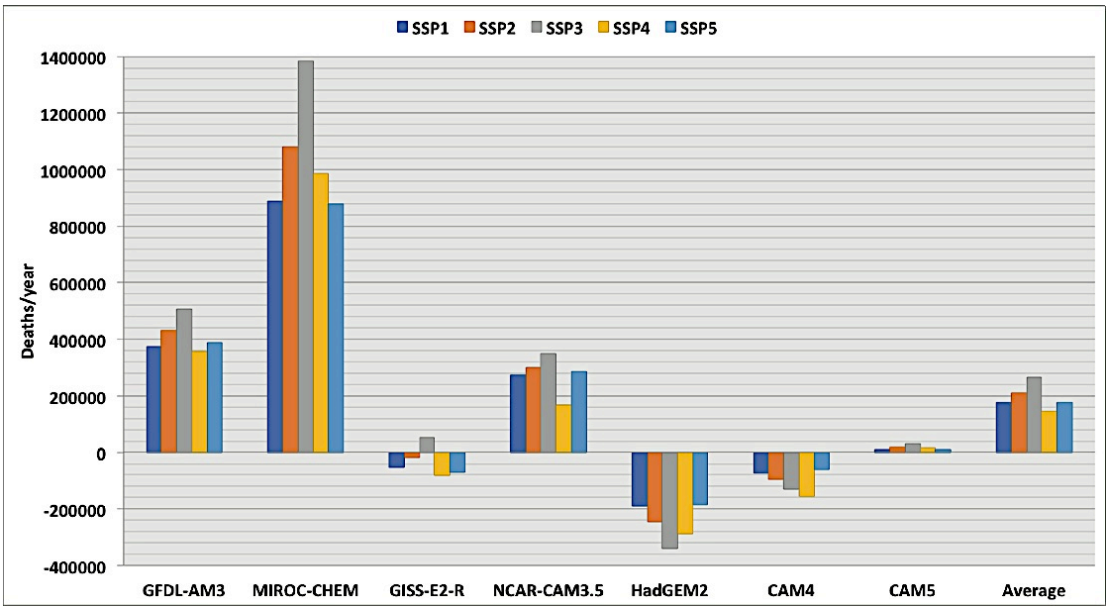

Figure 2.9 Global premature mortality based on future projected population (SSPs) by seven models.

Similar conclusions exist for regional annual mean premature mortality, which spans a large range across the SSPs and in particular, the models (Figure 2.10; Table 2.5). In many regions, including Africa, India, East Asia, and the Middle East, the magnitude of premature mortality is heavily modulated by the model, as opposed to the SSP. For example, except for HadGEM2, models show a large increase in premature deaths over India with SSP3, with a range from 60,176 (CAM5) to 931,800 (MIROC-CHEM) death/year. HadGEM2 yields a decrease of -172,866 deaths/year. In contrast, the range of premature deaths due to SSP, for a given region and model, is generally much smaller, but can still be factor of ~2. In MIROC-CHEM, for example, premature mortality over India ranges from 571,016 in SSP4 to 931,800 in SSP3. These results imply that much of the uncertainty in future premature deaths due to GHG-induced climate change is due to uncertainty in model physics and the representation of aerosol processes. However,

although future population is a smaller component of the uncertainty, it still contributes a factor of ~2 to the uncertainty in future premature deaths.

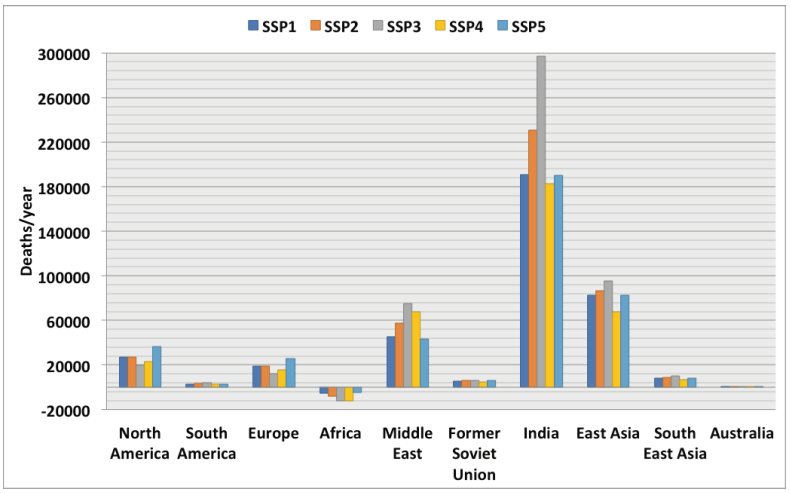
SSP1
SSP2
SSP3
SSP4
SSP5
Deaths/year
300000
260000
220000
180000
140000
100000
60000
20000
-20000
North America
South America
Europe
Africa
Middle East
Former Soviet Union
India
East Asia
South East Asia
Australia

(a)

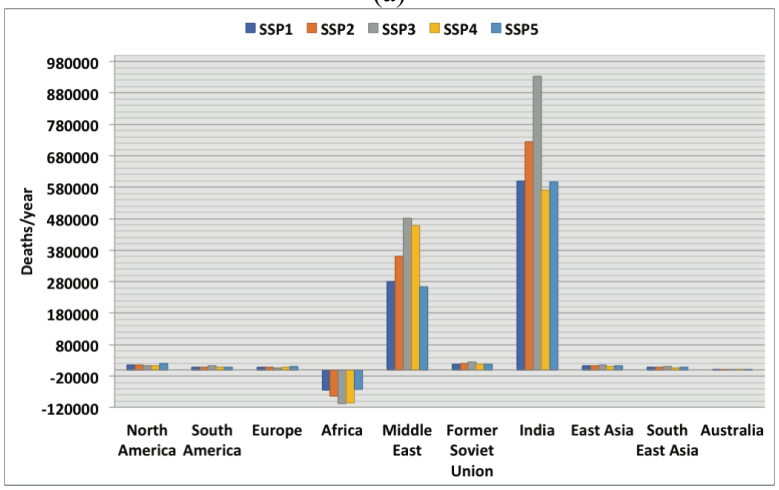
SSP1
SSP2
SSP3
SSP4
SSP5
Deaths/year
980000
880000
780000
680000
580000
480000
380000
280000
180000
80000
-20000
-120000
North America
South America
Europe
Africa
Middle East
Former Soviet Union
India
East Asia
South East Asia
Australia

(b)

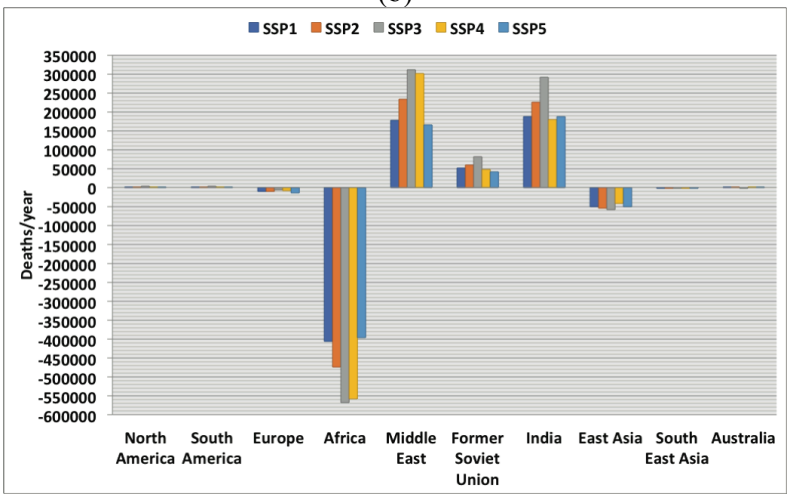
SSP1
SSP2
SSP3
SSP4
SSP5
Deaths/year
350000
300000
250000
200000
150000
100000
50000
0
-50000
-100000
-150000
-200000
-250000
-300000
-350000
-400000
-450000
-500000
-550000
-600000
North America
South America
Europe
Africa
Middle East
Former Soviet Union
India
East Asia
South East Asia
Australia

(c)

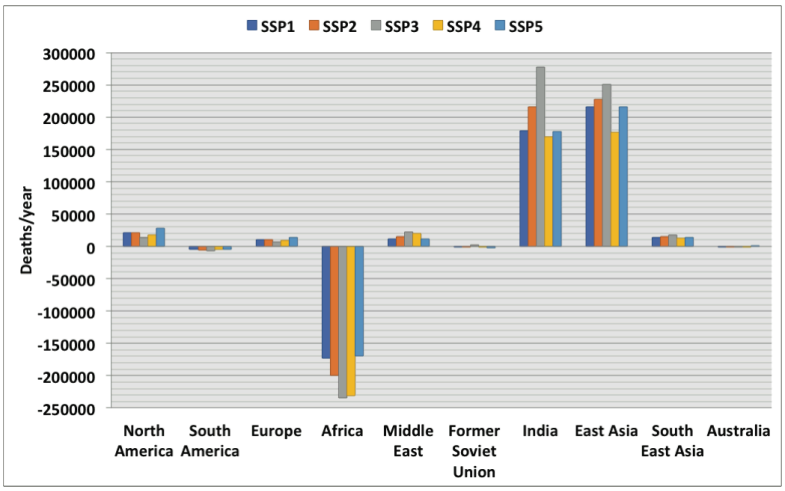
SSP1
SSP2
SSP3
SSP4
SSP5
Deaths/year
300000
250000
200000
150000
100000
50000
0
-50000
-100000
-150000
-200000
-250000
North America
South America
Europe
Africa
Middle East
Former Soviet Union
India
East Asia
South East Asia
Australia

(d)

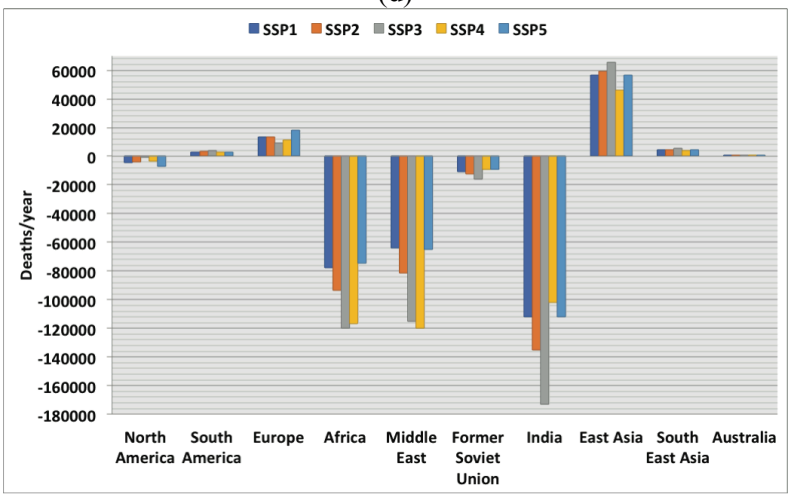
SSP1
SSP2
SSP3
SSP4
SSP5
Deaths/year
60000
40000
20000
0
-20000
-40000
-60000
-80000
-100000
-120000
-140000
-160000
-180000
North America
South America
Europe
Africa
Middle East
Former Soviet Union
India
East Asia
South East Asia
Australia

(e)

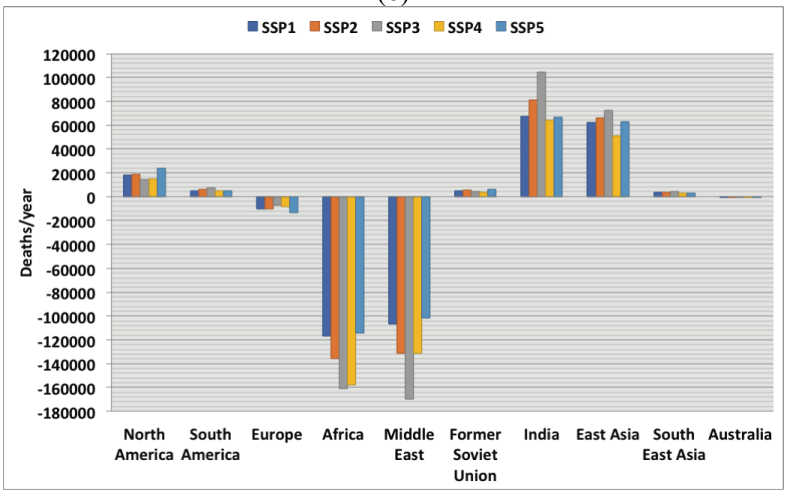
SSP1
SSP2
SSP3
SSP4
SSP5
Deaths/year
120000
100000
80000
60000
40000
20000
0
-20000
-40000
-60000
-80000
-100000
-120000
-140000
-160000
-180000
North America
South America
Europe
Africa
Middle East
Former Soviet Union
India
East Asia
South East Asia
Australia

(f)

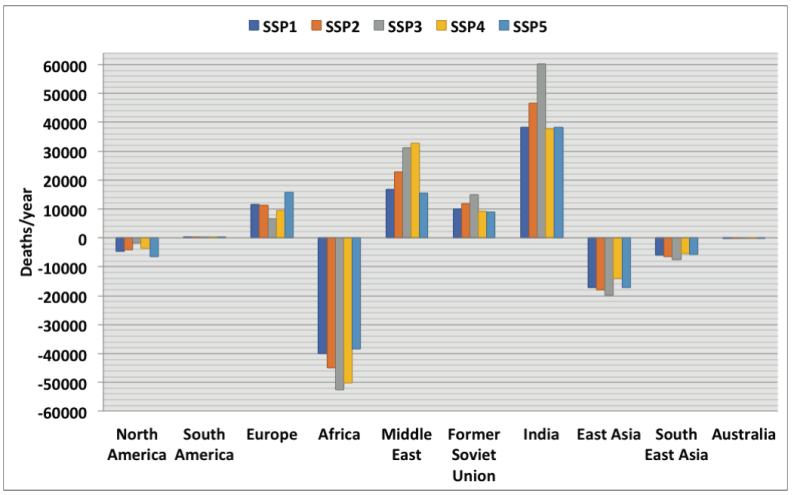

(g)

Figure 2.10 Premature mortality based on future projected population (SSPs) over 10 world regions from a) GFDL-AM3, b) MIROC-CHEM, c) GISS-E2-R, d) NCAR-CAM3.5, e) HadGEM2, f) CAM4, and g) CAM5.

Table 2.5 Total, minimum, and maximum premature mortality (deaths/year) for both lung cancer (LC) and cardiopulmonary diseases (CPD) for a) GFDL-AM3, b) MIROC-CHEM, c) GISS-E2-R, d) NCAR-CAM3.5, e) HadGEM2, f) CAM4, and g) CAM5 by ten regions and five future-population scenarios (SSPs).

a)	GFDL-AM3														
	SSP1			SSP2			SSP3			SSP4			SSP5		
	Min	Max	Total	Min	Max	Total	Min	Max	Total	Min	Max	Total	Min	Max	Total
North America	-1	565	27415	-1	705	27356	0	954	19667	-1	554	22794	-1	501	36362
South America	-8	436	2647	-10	521	3252	-13	652	4256	-8	418	2725	-8	428	2548
Europe	-23	3787	19215	-23	3730	18965	-14	2388	12067	-18	3095	15849	-31	5055	25648
Africa	-712	2909	-5288	-786	3098	-8228	-920	3345	-12195	-906	3280	-12426	-701	2889	-4945
Middle East	-647	1923	45411	-819	2455	57205	-1223	3286	75451	-1176	3174	67915	-618	1831	43227
Former Soviet Union	-154	513	5367	-180	588	6266	-240	593	5882	-136	465	4770	-129	565	6338
India	-312	11755	190765	-376	14200	230511	-483	18226	296693	-293	11054	182771	-310	11711	189822
East Asia	-225	2053	82346	-237	2162	86660	-263	2392	95388	-185	1683	67382	-226	2055	82735
South East Asia	0	508	8043	0	535	8826	0	592	10163	0	417	6939	0	509	7918
Australia	0	13	35	0	16	42	0	19	43	0	19	46	0	13	40

b)	MIROC-CHEM														
	SSP1			SSP2			SSP3			SSP4			SSP5		
	Min	Max	Total	Min	Max	Total	Min	Max	Total	Min	Max	Total	Min	Max	Total
North America	-12	496	15357	-15	619	15855	-20	837	13044	-11	486	13017	-11	440	19510
South America	-5	1215	7958	-6	1469	9685	-8	1696	12174	-5	1196	8091	-4	1239	7786
Europe	-568	5640	8442	-556	5556	8714	-340	3556	5376	-451	4610	7582	-772	7529	11755
Africa	-3524	1189	-63587	-3891	1470	-82682	-4553	1758	-107681	-4485	1772	-104915	-3469	1197	-61232
Middle East	-1112	9787	279688	-1303	12496	360051	-1611	16728	480235	-1033	16155	457745	-1074	9321	264479
Former Soviet Union	-51	747	18313	-57	855	21388	-64	862	25576	-43	676	16895	-51	823	17529
India	-115	20777	600099	-139	25098	724868	-178	32215	931800	-108	19537	571016	-114	20699	597359
East Asia	-479	368	13190	-504	388	13854	-558	429	14986	-393	302	10666	-479	368	13449
South East Asia	-7	511	7950	-8	576	8833	-8	667	10249	-6	457	6914	-7	496	7763
Australia	0	6	17	0	9	22	0	10	23	0	10	24	0	6	20

c)	GISS-E2-R														
	SSP1			SSP2			SSP3			SSP4			SSP5		
	Min	Max	Total	Min	Max	Total	Min	Max	Total	Min	Max	Total	Min	Max	Total
North America	-88	394	1168	-84	492	1934	-51	665	3801	-72	386	1386	-121	350	277
South America	-28	191	1866	-34	227	2264	-47	283	2834	-38	183	1722	-26	192	1869
Europe	-635	4236	-11046	-625	4173	-10605	-400	2671	-6789	-519	3462	-8693	-847	5655	-14426
Africa	-18168	224	-406602	-19350	239	-473995	-20890	258	-568523	-20486	253	-558312	-18041	223	-396828
Middle East	-7238	7068	176704	-8484	9024	232740	-10491	12081	311600	-6392	11667	300869	-6990	6731	164500
Former Soviet Union	-969	3202	50653	-1109	3745	59502	-1118	4998	80669	-877	2842	46839	-1067	2695	41686
India	-20610	18681	186876	-24896	22566	226083	-31955	28964	290995	-19380	17566	178712	-20532	18610	186404
East Asia	-854	332	-50886	-899	350	-53570	-995	387	-59204	-700	272	-41772	-855	332	-50935
South East Asia	-289	332	-2140	-326	350	-2515	-378	387	-3054	-259	272	-2023	-281	332	-2022
Australia	-1	10	2	-1	10	2	-2	5	-4	-2	9	1	-1	15	5

d)	NCAR-CAM3.5														
	SSP1			SSP2			SSP3			SSP4			SSP5		
	Min	Max	Total	Min	Max	Total	Min	Max	Total	Min	Max	Total	Min	Max	Total
North America	-20	373	20956	-24	438	20636	-33	593	14025	-19	344	17222	-18	513	28264
South America	-373	28	-4577	-445	34	-5379	-557	40	-6678	-357	28	-4300	-366	29	-4467
Europe	-95	3491	10646	-94	3438	10693	-57	2201	7107	-76	2853	9014	-130	4660	14129
Africa	-10334	113	-172919	-11006	143	-199501	-11882	197	-234249	-11652	193	-230510	-10261	122	-169667
Middle East	-3661	1394	12018	-4291	1764	15159	-5307	2632	21817	-3234	2531	19630	-3536	1330	11136
Former Soviet Union	-238	519	-569	-273	607	-437	-301	811	1933	-216	461	-350	-263	437	-2218
India	-84	10597	178653	-102	12801	215542	-131	16430	276970	-79	9965	169733	-84	10557	177410
East Asia	-221	1933	215711	-261	2036	227011	-326	2252	250524	-200	1585	176719	-221	1935	216231
South East Asia	0	669	14106	0	704	15521	0	779	17844	0	548	12265	0	669	13872
Australia	-9	6	-9	-11	6	-14	-13	4	-27	-13	6	-21	-9	11	3

e)	HadGEM2														
	SSP1			SSP2			SSP3			SSP4			SSP5		
	Min	Max	Total	Min	Max	Total	Min	Max	Total	Min	Max	Total	Min	Max	Total
North America	-436	829	-4575	-544	1034	-3858	-737	1398	-708	-428	812	-3494	-499	735	-7079
South America	-417	678	2729	-504	808	3287	-646	1005	4158	-404	650	2683	-401	683	2749
Europe	-11	1825	13668	-11	1797	13552	-7	1150	8974	-9	1491	11263	-15	2436	18056
Africa	-4592	4278	-77824	-5680	4556	-93393	-6793	4919	-119932	-6847	4824	-116628	-4624	4248	-74739
Middle East	-14739	4016	-63910	-18651	4707	-81160	-27837	5821	-114894	-26770	3547	-119831	-14068	3878	-65087
Former Soviet Union	-1920	113	-10632	-2246	130	-12314	-2997	131	-16099	-1704	103	-9464	-1616	125	-9128
India	-5128	11694	-111835	-6194	14126	-135195	-7950	18132	-172866	-4822	10996	-101848	-5108	11650	-111740
East Asia	-107	1022	56489	-112	1077	59500	-124	1191	65750	-87	838	46208	-107	1023	56613
South East Asia	-24	345	4405	-28	363	4718	-35	402	5297	-21	283	3731	-22	345	4373
Australia	-4	30	29	-5	30	30	-3	17	9	-4	26	23	-6	43	54

f)	CAM4														
	SSP1			SSP2			SSP3			SSP4			SSP5		
	Min	Max	Total	Min	Max	Total	Min	Max	Total	Min	Max	Total	Min	Max	Total
North America	0	679	18216	0	846	18478	0	1145	14194	0	665	15271	0	602	23728
South America	-99	701	4966	-120	837	6027	-167	1047	7653	-100	672	4940	-93	688	4871
Europe	-4961	77	-10285	-4887	75	-10210	-3128	46	-6956	-4055	61	-8569	-6623	104	-13445
Africa	-8756	1008	-117201	-9325	1113	-135994	-10067	1303	-161243	-9873	1283	-158201	-8694	993	-114256
Middle East	-11080	1321	-106901	-12987	1559	-131264	-16060	1762	-170004	-9786	2018	-131449	-10700	1496	-101818
Former Soviet Union	-266	514	4633	-305	588	5337	-307	593	4374	-241	465	3706	-293	565	5883
India	-1283	7741	67544	-1550	9351	81486	-1989	12002	104713	-1206	7279	63971	-1278	7712	66993
East Asia	-120	890	62547	-129	937	65842	-160	1037	72702	-98	730	51148	-120	891	62705
South East Asia	-3	162	3374	-3	170	3718	-3	189	4332	-2	133	2838	-3	162	3296
Australia	-7	4	-18	-9	4	-21	-10	2	-26	-10	3	-25	-7	5	-16

g)	CAM5														
	SSP1			SSP2			SSP3			SSP4			SSP5		
	Min	Max	Total	Min	Max	Total	Min	Max	Total	Min	Max	Total	Min	Max	Total
North America	-234	262	-4551	-223	327	-4101	-135	442	-1715	-190	257	-3580	-322	232	-6620
South America	-421	634	67	-508	758	166	-652	948	420	-407	608	226	-405	623	16
Europe	-39	2899	11428	-36	2856	11253	-23	1828	6654	-30	2369	9350	-49	3870	15710
Africa	-5440	1409	-39918	-5794	1743	-45082	-6255	2085	-52615	-6134	2101	-50329	-5402	1419	-38463
Middle East	-1615	619	16757	-1893	875	22823	-2340	1167	31194	-1426	1094	32762	-1559	542	15416
Former Soviet Union	-27	373	9946	-30	437	11711	-31	583	14825	-24	331	9076	-29	314	8978
India	-1498	1975	38279	-1810	2386	46492	-2323	3062	60176	-1409	1857	37687	-1493	1968	38308
East Asia	-583	393	-17108	-614	414	-17968	-679	458	-19740	-478	322	-14087	-583	394	-17181
South East Asia	-439	153	-5859	-495	161	-6590	-574	178	-7630	-393	125	-5380	-426	153	-5766
Australia	-1	3	-9	-1	3	-8	0	4	-4	-1	4	-7	-1	3	-15

References

Allen, R. J., Landuyt, W., and Rumbold, S. T. (2016), An increase in aerosol burden and radiative effects in a warmer world. *Nature Climate Change*, 6, 269-274. doi:10.1038/nclimate2827.

Anenberg, S. C., Horowitz, L. W., Tong., D. Q., and West, J. J. (2010), An estimate of the global burden of anthropogenic ozone and fine particulate matter on premature human mortality using atmospheric modeling. *Environ. Health. Perspect.* 118, 1189. doi: 10.1289/ehp.0901220.

Bhaduri, B., Bright, E., Coleman, P., and Urban., M. L. (2002) LandScan Geoinformatics. 5, 34-37.

Collins, W. J. et al. (2011), Development and evaluation of an Earth-system model–HadGEM2, *Geosci. Model Dev.* 4, 1051-1075. doi:10.5194/gmd-4-1051-2011.

Fang, Y., Fiore, A. M., Horowitz, L. W., Gnanadesikan, A., Held, I., Chen, G., Vecchi, G., and Levy., H. (2011), The impacts of changing transport and precipitation on pollutant distributions in a future climate, J. Geophys. Res., 116, D18303, doi:10.1029/2011JD015642.

Fang, Y., Mauzerall, D. L., Liu, J., Fiore, A. M.,Horowitz., L. W. (2013), Impacts of 21st century climate change on global air pollution-related premature mortality. *Climatic Change*. 121, 239-253. https://doi.org/10.1007/s10584-013-0847-8.

Jacob, D. J. and Winner, D. A. (2009) Effect of climate change on air quality. *Atmos. Environ.* 43, 51-63. https://doi.org/10.1016/j.atmosenv.2008.09.051.

Kloster, S., Dentener, F., Feichter, J., Raes, F., Lohmann, U., Roeckner., E, Fischer-Bruns, I. (2010), A GCM study of future climate response to aerosol pollution reductions. *Clim. Dynam*. 34, 1177-1194. https://doi.org/10.1007/s00382-009-0573-0.

Krewski, D., et al. (2009), Extended Follow-Up and Spatial Analysis of the American Cancer Society Study Linking Particulate Air Pollution and Mortality (HEI Research Report 140) (Boston, MA: Health Effects Institute).

Lamarque, J. F. *et al.* (2013), The Atmospheric Chemistry and Climate Model Intercomparison Project (ACCMIP): overview and description of models, simulations and climate diagnostics. *Geosci. Model Dev.* 6, 179-206. DOI: 10.5194/gmd-6-179-2013.

Lelieveld, J. Evans, J. S., Fnais, M., Giannadaki, D., and Pozzer., A. (2015), The contribution of outdoor air pollution sources to premature mortality on a global scale, *Nature,* 525, 367-371. doi:10.1038/nature15371.

Mickley, L. J., D. J. Jacob, B. D. Field, and D. Rind (2004), Effects of future climate change on regional air pollution episodes in the United States, Geophys. Res. Lett., 31, L24103, doi:10.1029/2004GL021216.

Nawahda, A., Yamashita, K., Ohara, T., Kurokawa, J., Yamaji, K. (2012), Evaluation of premature mortality caused by exposure to $PM_{2.5}$ and ozone in East Asia: 2000, 2005, 2020. *Water Air Soil Pollut.* 223, 3445-3459. https://doi.org/10.1007/s11270-012-1123-7.

O'Neill, B. C., Edmonds, J., Hallegatte., S, Ebi, K. L., Kram, T., Riahi, K., Winkler, H., van Vuuren., D. P. (2014), A new scenario framework for climate change research: the concept of shared socioeconomic pathways. *Climatic Change,* 122, 387-400. https://doi.org/10.1007/s10584-013-0905-2.

Post, E. S., *et al.* (2012), Variation in estimated ozone-related health impacts of climate change due to modeling choices and assumptions. *Environ. Health Perspect.* 120, 1559–64. doi: 10.1289/ehp.1104271.

Samir, K. C. and Wolfgang, Lutz. (2017), The human core of the shared socioeconomic pathways: Population scenarios by age, sex and level of education for all countries to 2100. *Global Environ. Change.* 42, 181-192. https://doi.org/10.1016/j.gloenvcha.2014.06.004.

Shen, L., Mickley, L. J. and Murray, L. T. (2016), Influence of 2000–2050 climate change on particulate matter in the United States: results from a new statistical model. *Atmos. Chem. Phys.* 17.6. 4355-4367. doi:10.5194/acp-17-4355-2017.

Silva, R. A. *et al.,* (2013), Global premature mortality due to anthropogenic outdoor air pollution and the contribution of past climate change. *Envir. Res. Lett.* 8, 034005. doi:10.1088/1748-9326/8/3/034005.

Silva, R. A. *et al.,* (2016), The effect of future ambient air pollution on human premature mortality to 2100 using output from the ACCMIP model ensemble. *Atmos. Chem. Phys. Discuss*. 2016, 1-24. doi:10.5194/acp-16-9847-2016.

Silva, R. A., *et al.,* (2017), Future global mortality from changes in air pollution attributable to climate change. *Nature Climate Change.* doi:10.1038/NCLIMATE3354.

United Nations, Department of Economic and Social Affairs, Population Division 2015 World Population Prospects: The 2015 Revision custom data acquired via website.

Westervelt, D. M., Horowitz, L.W., Naik, V., Tai, A.P.K., Fiore, A.M., Mauzerall, D.L. (2016) Quantifying $PM_{2.5}$-meteorology sensitivities in a global climate model. *Atmos. Environ.* 142, 43-56. https://doi.org/10.1016/j.atmosenv.2016.07.040.

Chapter 3 Investigation of future changes in drought risk over California under a business-as-usual scenario

Abstract

How climate change will impact future water resources is an important issue in many world regions, particularly California (CA). Future water availability depends on changes in many hydrological parameters, including precipitation, evaporation, runoff, and soil moisture. Many previous studies show that CA will experience more intense and frequent drought associated with a decrease in precipitation, and an increase in evaporation in the future. A recent study, however, showed consistent increase in precipitation under warming, particularly in models that are able to simulate the observed relationship between El-Nino and CA precipitation. Using several drought indicators, I investigate future CA drought risk under Representative Concentration Pathway 8.5 (RCP8.5) with the Community Earth System Model Large Ensemble Project (CESM-LENS), which is one of the models that simulates the observed relationship between El-Nino and CA precipitation. The model yields a non-significant increase in CA drought risk in warmer world.

3.1 Introduction

In recent years, many regions have experienced severe droughts, leading to significant stress on water resources [*AghaKouchak et al.,* 2014; *Griffin and Anchukaitis,* 2014; *Howitt et al.,* 2014; *Wang et al.,* 2014]. A poleward expansion of the subtropical dry zones and reduction in precipitation in the subtropics leads to dry and warm conditions [*Held and Soden.* 2006; *Meehl et al.,* 2007; *Seidel et al.,* 2008; *Allen et al.,* 2012; *Collins et al.,* 2013]. In addition, increases in evaporation and decreases in mountain snow mass, derived from warmer temperatures, raise the intensity of droughts [*Cayan et al.,* 2010; *Cook et al.,* 2014]. The combination of these responses leads to a decrease in surface water availability [*Seager et al.,* 2013] and likely enhanced drought conditions.

Many previous studies indicate an increase in the intensity and frequency of drought in a warmer world. This is associated with decreases in precipitation, increases in evaporation, and warm-dry conditions [*Dai.* 2011; *Dai.* 2013; *Diffenbaugh et al.,* 2015; *Mann and Gleick.* 2015; *Trenberth et al.,* 2014]. Recent studies, however, indicate contradictory results under warming [*Allen and Luptowitz.* 2017; *Cheng et al.,* 2016; Sheffield *et al.,* 2012]. *Sheffield et al*. [2012] indicate that the most commonly used drought assessment method (PDSI: Palmer Drought Severity Index) in previous studies may overestimate global drought due to too much emphasis on increase evaporation under warming.

Two studies, including *Cheng et al.* [2016] and *Allen and Luptowitz*. [2017], focus on California (CA) droughts. *Cheng et al.* [2016] investigate the effects of anthropogenic

climate change on CA drought risk associated with radiative forcing. The results show an increase in radiative forcing since preindustrial time leads to increases annual precipitation and surface temperature over CA. *Allen and Luptowitz* [2017] indicate that models which reproduce the observed relationship between El-Nino and CA precipitation yield larger and consistent increases in future CA precipitation. In addition, they illustrate that tropical Pacific sea surface temperature warming leads to the increase in CA precipitation.

Many components, including surface water availability, runoff, and soil moisture, are used [*Chen et al.,* 2016; *Otkin et al.,* 2014; *Saft et al.,* 2015] to quantify meteorological, agricultural, and hydrological droughts. In general, meteorological drought is quantified by the amount of precipitation, dry date, and intensity of drought [*Wilhite and Glantz*. 1985]. Agricultural drought is associated with impacts of meteorological drought on plant and crop growth. Therefore, soil moisture is a major metric to assess agricultural drought. Different from the previous two droughts, lack of water due to more water consumption or less water supplies, is defined as hydrological drought.

Precipitation is one of the important components of drought. In this study, CESM-LENS is used to investigate how future drought risk over CA will change under warming. I use CESM-LENS because it simulates the observed relationship between El-Nino and CA precipitation. *Allen and Luptowitz*. [2017] show more CA precipitation associated with warmer sea surface temperature using observed winter seasonal variation. Moreover, CESM-LENS yields a similar spatial pattern with 21st century winter precipitation and

sea surface temperature trends: larger increase in winter precipitation is associated with larger warming over central/eastern Pacific sea surface temperature. Their work suggests the importance of an El-Nino like-teleconnection in driving a future increase in CA precipitation. Section 2 describes the data and methods I employ, and Section 3 discusses our results. Conclusions are provided in Chapter 4.

3.2 Data and Methods

Monthly data of 40-realizations for precipitation, evaporation, runoff, and soil moisture, from CESM-LENS (Community Atmosphere Model, version 5 - Large Ensemble Community Project) [*Kay et al.,* 2015] are used to assess future CA drought risk under warming. Each realization carries different initial conditions for climate variability assessment. CESM-LENS provides high spatial resolution (approximately 1 degree) and consists of coupled atmosphere, ocean, land, and sea-ice component models. The CESM LENS simulations, with time-varying greenhouse gases, allows consideration of possible climate impacts in the real world. The experiment for the 21st century (2006-2100) is forced by RCP8.5: well-mixed greenhouse gases, short-lived gases, and aerosols [*Kay et al.,* 2015]. Historical forcing based on observed emissions reconstructions is used for the 20th century (1920-2005) [*Lamarque et al*. 2010].

To investigate future drought, I calculate annual means from monthly average data from each realization. Units of all hydrological variables are converted to millimeter. For the surface water availability, precipitation minus evaporation (P-E) is used. Moreover, I investigate the amount of soil moisture in two layers, shallow (~0-0.25m)

and deep (~1.5-3m), to quantify agricultural drought. Soil moisture in the top layer is primarily sensitive to temperature changes. Warmer temperatures evaporate more moisture from the soil top layer. Deep soil moisture controls moisture supply for most plants and crops. Moreover, this layer is strongly associated with changes in precipitation [*Cheng et al.* 2016].

A drought year is defined as one in which precipitation (or soil moisture/streamflow) falls below a 0.5 standard deviation (σ) departure from the 1950-1999 climatological mean. The change in drought risk under warming is defined as the difference in the probability of drought from 2050-2099 relative to 1950-1999. Probabilities are calculated for each of the 40 realizations, and then averaged to form the ensemble mean.

California is defined by three regions, representing southern (32.0-34.9° N: 239.4-245.6°E), central (34.9-38.6°N: 236.9-243.1°E), and northern (38.8-42.4°N: 235.6-240.6°E) California. Figure 3.1 indicates the three regions with black boxes.

3.3 Results

CESM-LENS yields a positive ensemble mean annual mean trend for all hydrological variables over CA, including precipitation, runoff, surface water availability, and shallow/deep soil moistures (Figure 3.1). The annual mean precipitation shows a positive trend that ranges from 0.03 to 0.44 mm day^{-1} $century^{-1}$, with a 40-realization ensemble mean trend of 0.23 mm day^{-1} $century^{-1}$. 100% of the realizations yield an increase in CA annual precipitation. This suggests natural variability, although the cause

of the spread of trends, does not lead to any negative precipitation trends.

Figure 3.1a shows ensemble mean annual mean precipitation trend in three CA regions: southern, central, and northern (black boxes). Over these three regions, the largest increase in precipitation occurs over northern CA (0.41 mm day^{-1} $century^{-1}$), followed by central CA (0.23 mm day^{-1} $century^{-1}$), with southern CA possessing the weakest increase (0.035 mm day^{-1} $century^{-1}$). 52% of the realizations yield a positive precipitation trend over southern CA. In contrast, 95% and 100% of the realizations yield a positive precipitation trend in central and northern CA, respectively (Figure 3.2a). Thus, the increase in precipitation is very robust in central and northern CA.

The annual mean surface water availability (P-E) yields trends that range from -0.25 to 0.89 mm day^{-1} $century^{-1}$, with a 40-realization ensemble mean trend of 0.31 mm day^{-1} $century^{-1}$. 85% of the realizations agree on an increase in P-E (Figure 3.2b). The ensemble mean annual mean runoff trend is 0.14 mm day^{-1} $century^{-1}$, which ranges from -0.02 to 0.29 mm day^{-1} $century^{-1}$ (Figure 3.1c). Nearly all (98%) of the realizations yield an increase in runoff (Figure 3.2c).

P-E over central and northern CA indicate a positive trend at 0.09 and 0.29 mm day^{-1} $century^{-1}$. However, southern CA features a negative P-E trend at -0.07 mm day^{-1} $century^{-1}$ (Figure 3.1b) with 82% realization agreement. Similar to P-E, runoff generally features positive trends at 0.3 and 0.13 mm day^{-1} $century^{-1}$ for northern and central CA. However, runoff over southern CA also yields a positive (but weak) trend at 0.01 mm day^{-1} $century^{-1}$. Nearly all of the realizations agree on a positive trend over northern and central CA for both P-E (98% and 85%) and runoff (95% and 98%) (Figure 3.2b and c).

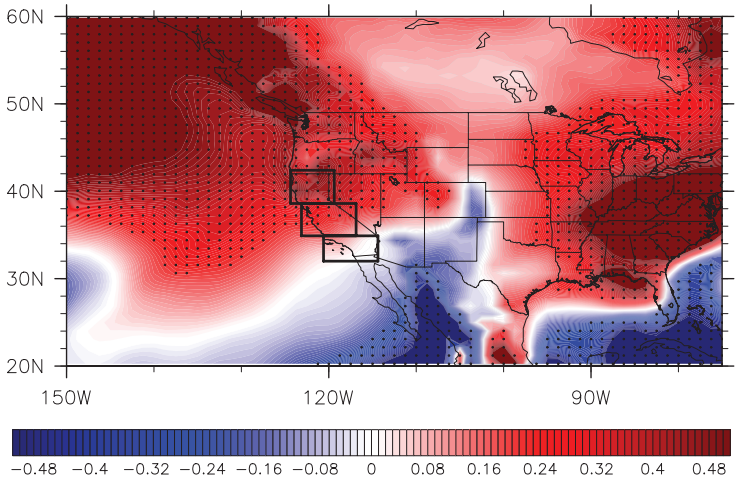
60N
50N
40N
30N
20N
150W
120W
90W
−0.48 −0.4 −0.32 −0.24 −0.16 −0.08 0 0.08 0.16 0.24 0.32 0.4 0.48

(a)

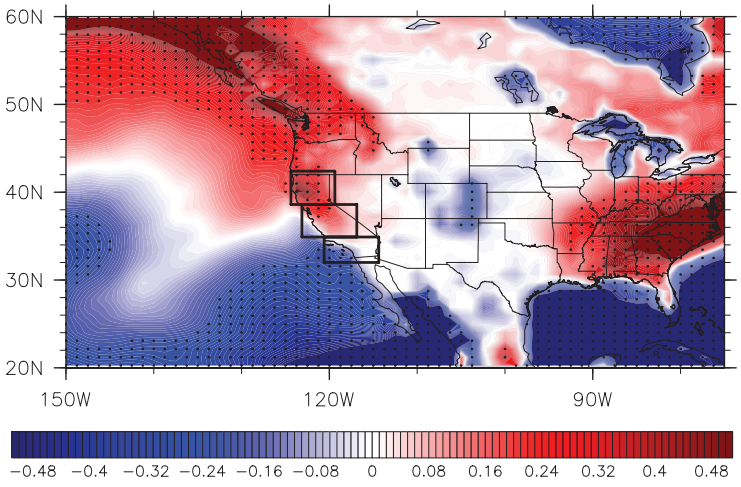
60N
50N
40N
30N
20N
150W
120W
90W
−0.48 −0.4 −0.32 −0.24 −0.16 −0.08 0 0.08 0.16 0.24 0.32 0.4 0.48

(b)

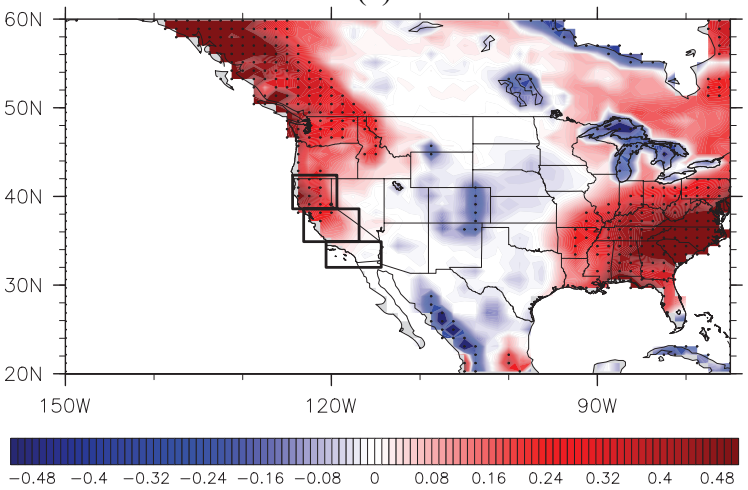
60N
50N
40N
30N
20N
150W
120W
90W
−0.48 −0.4 −0.32 −0.24 −0.16 −0.08 0 0.08 0.16 0.24 0.32 0.4 0.48

(c)

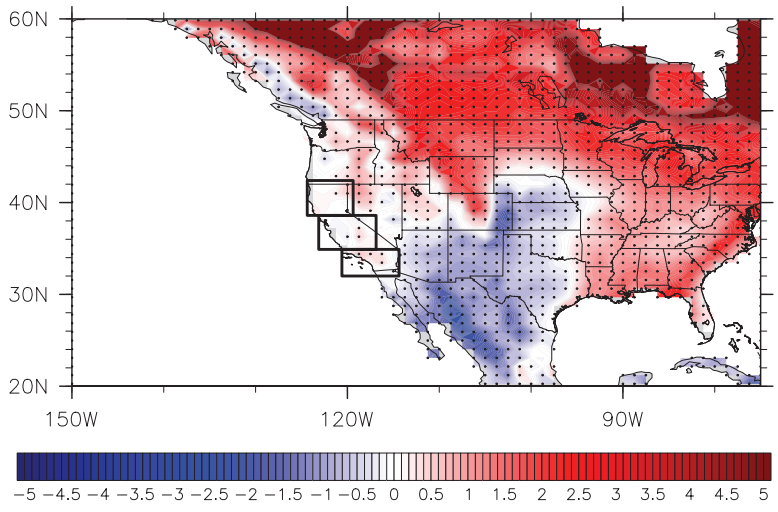

(d)

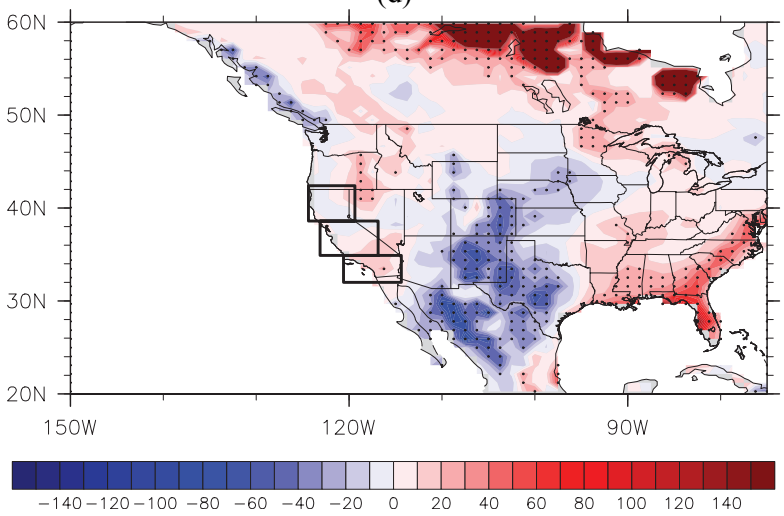

(e)

Figure 3.1 CESM-LENS 21st century (2006-2100) ensemble mean annual mean trend of a) precipitation, b) surface water availability (P-E), c) runoff, d) shallow soil moisture, and e) deep soil moisture. Units for precipitation, P-E and runoff is mm day^{-1}century^{-1} and mm century^{-1} for soil moisture. Red (Blue) colors indicates a positive (negative) trend. Boxes over CA represent three sub-regions: southern, central, and northern. Symbols represent trend significance at 95% confidence level.

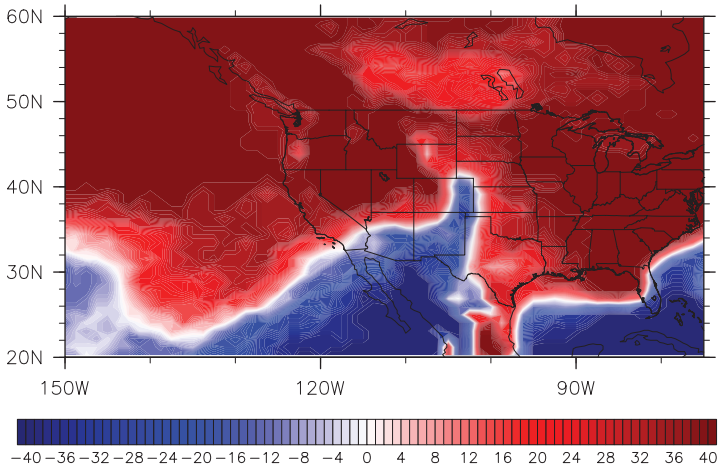
60N
50N
40N
30N
20N
150W
120W
90W
−40 −36 −32 −28 −24 −20 −16 −12 −8 −4 0 4 8 12 16 20 24 28 32 36 40

(a)

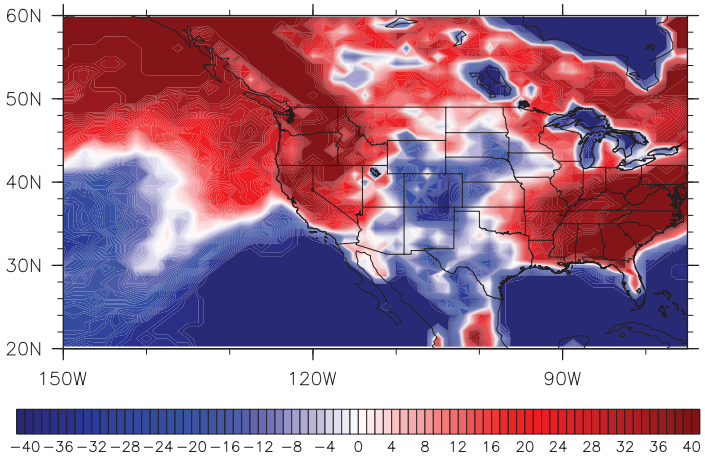
60N
50N
40N
30N
20N
150W
120W
90W
−40 −36 −32 −28 −24 −20 −16 −12 −8 −4 0 4 8 12 16 20 24 28 32 36 40

(b)

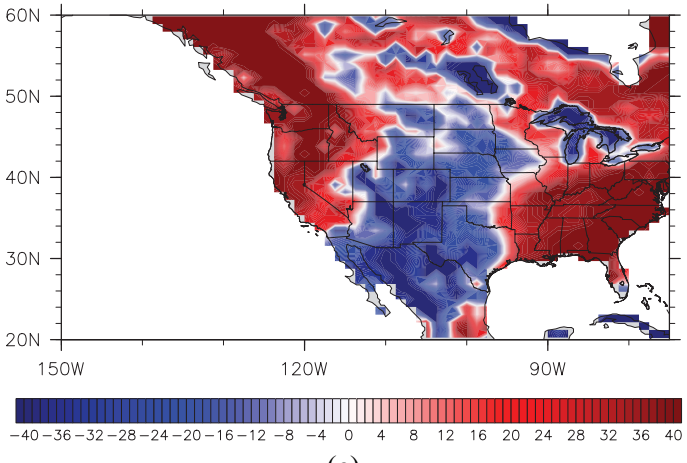
60N
50N
40N
30N
20N
150W
120W
90W
−40 −36 −32 −28 −24 −20 −16 −12 −8 −4 0 4 8 12 16 20 24 28 32 36 40

(c)

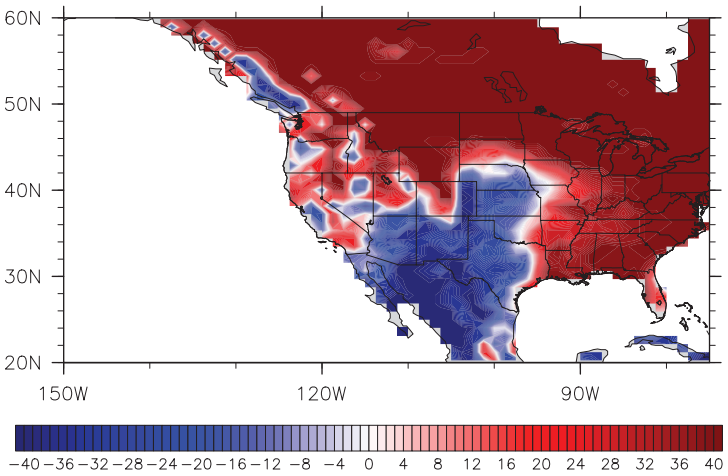

(d)

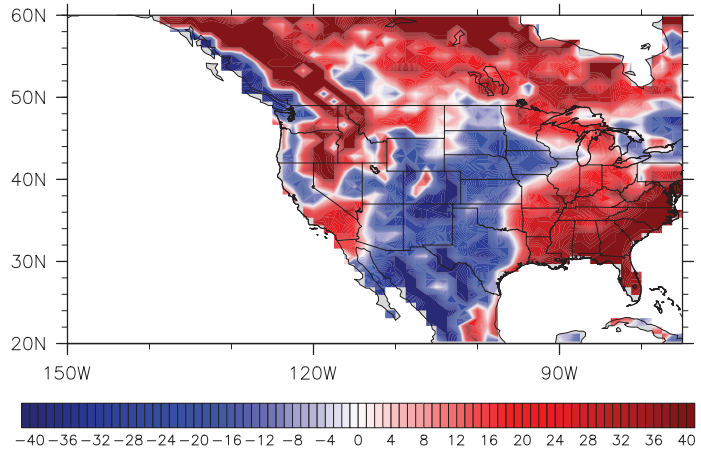

(e)

Figure 3.2 The number of CESM-LENS 21st century realizations that yield an increase (red) or decrease (blue) in annual mean a) precipitation, b) surface water availability (P-E), c) runoff, d) shallow soil moisture, and e) deep soil moisture.

Figure 3.1d and e show the ensemble mean annual mean shallow and deep soil moisture trend over the 21st century. Ensemble mean annual mean of both shallow and deep CA soil moisture are projected to increase at 0.04 (range: -0.45 to 0.52) and 5.73 (range: -7.75 to 20.5) mm century^{-1}. Moreover, the majority of realizations agree on an increase in shallow and deep soil moisture over the entire state, at 67.5% and 70% (Figure 3.2d and e), respectively. All three regions yield a positive trend in both shallow and deep soil moisture. A north to south gradient in the deep soil moisture trend exists, ranging from 1.8 mm century^{-1} in northern CA to 3.7 and 11.7 mm century^{-1} in central and southern CA, respectively. In contrast, shallow soil moisture shows the opposite gradient – an increase from south (0.09 mm century^{-1}) to north (0.16 mm century^{-1}) but with a relatively small increase in central CA (0.02 mm century^{-1}).

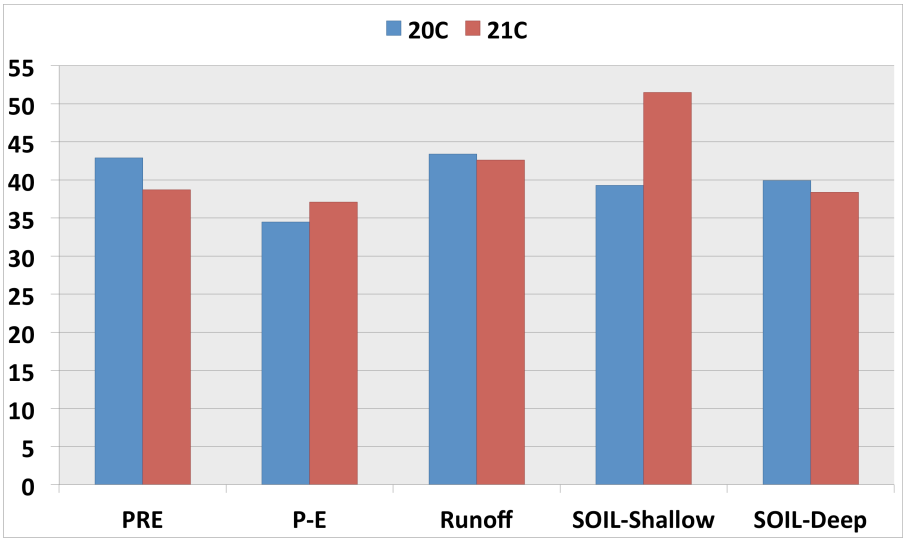

Figure 3.3 Estimated California drought risk (%) based on precipitation (PRE), surface water availability (P-E), Runoff, shallow soil moisture (SOIL-shallow) and deep soil moisture (SOIL-Deep). Blue and red colored bars represent the 20 and 21st century, respectively.

Figure 3.3 shows the CA drought risk for all hydrological variables, including precipitation (PRE), surface water availability (P-E), runoff, shallow soil moisture (SOIL-shallow) and deep soil moisture (SOIL-Deep). CESM-LENS indicates that drought risk related to precipitation, runoff, and deep soil moisture decrease in the 21st century, relative to 20 century, with decreases of 4.2, 0.8, and 1.5%, respectively (Table 3.1). Opposite results occur for P-E and shallow soil moisture, which yield an increase in drought risk in the future relative to present. A large increase in drought risk base on shallow soil moisture exists compared to the other variables (12.2% increase in drought risk) (Table 3.1).

Table 3.1 Estimated California drought risk (%) in the 20 and 21st century and differences (21st century minus 20th century) between the two centuries. Bold numbers represent significant changes at the 95% confidence level.

	20C	21C	Difference between 21C and 20C
Precipitation	42.9	38.7	**-4.2**
Precipitation-Evaporation (P-E)	34.5	37.1	**2.6**
Runoff	43.4	42.6	-0.8
Shallow Soil Moisture	39.3	51.5	**12.2**
Deep Soil Moisture	39.9	38.4	-1.5

References

AghaKouchak, A., L. Cheng, O. Mazdiyasni, and A. Farahmand. (2014) Global warming and changes in risk of concurrent climate extremes: Insights from the 2014 California drought, Geophys. Res. Lett., 41, 8847–8852, doi:10.1002/2014GL062308.

Allen, R. J. and Luptowitz R. (2017). El Niño-like teleconnection increases California precipitation in response to warming. Nature Communications. doi:10.1038/ncomms16055.

Allen, R. J., Sherwood, S. C., Norris, J. R. and Zender, C. S. (2012), Recent Northern Hemisphere tropical expansion primarily driven by black carbon and tropospheric ozone. Nature 485, 451 350–354.

Cayan, D. R. et al. Future dryness in the southwest US and the hydrology of the early 21st century drought. Proceedings of the National Academy of Sciences 107, 21271–21276, doi:435 10.1073/pnas.0912391107 (2010).

Chen, X., Y. Su, J. Liao, J. Shang, T. Dong, C. Wang, W. Liu, G. Zhou, and L. Liu (2016), Detecting significant decreasing trends of land surface soil moisture in eastern China during the past three decades (1979–2010), J. Geophys. Res. Atmos., 121, 5177–5192, doi:10.1002/2015JD024676.

Cheng, L., Hoerling, M., AghaKouchak, A., Livneh, B., Quan, X.W. and Eischeid, J., (2016), How has human-induced climate change affected California drought risk?. Journal of Climate, 29(1), 111-120, https://doi.org/10.1175/JCLI-D-15-0260.1.

Collins, M. et al. Long-term Climate Change: Projections, Commitments and Irreversibility. In: Climate Change 2013: The Physical Science Basis. Contribution of Working Group I to the Fifth Assessment Report of the Intergovernmental Panel on Climate Change (Cambridge University Press, 2013).

Cook, B. I., Smerdon, J. E., Seager, R., and Coats, S. (2014) Global warming and 21st century drying. Clim. Dyn. 43, 2607–2627, doi: 10.1007/s00382–014–2075–y.

Dai, A. (2011), Characteristics and trends in various forms of the Palmer Drought Severity Index during 1900–2008, J. Geophys. Res., 116, D12115, doi:10.1029/2010JD015541.

Dai, A. (2013), Increasing drought under global warming in observations and models, Nature Climate Change, 3, 52–58, doi:10.1038/nclimate1633.

Diffenbaugha, N. S., Swaina, D, L., and Toumaa, D. (2014), Anthropogenic warming has increased drought risk in California, PNAS, 112, 3931-3936, doi: 10.1073/pnas.1422385112.

Griffin, D., and K. J. Anchukaitis. (2014), How unusual is the 2012–2014 California drought?, Geophys. Res. Lett., 41, 9017–9023, doi:10.1002/2014GL062433.

Held, I. M. and Soden, B. J. (2006), Robust responses of the hydrological cycle to global warming. J. Climate 19, 5686–5699.

Howitt, R. E., J. Medellin-Azuara, D. MacEwan, J. R. Lund, and D. A. Summer, (2014) Economic analysis of the 2014 drought for California agriculture. Tech. Rep., Center for Watershed Sciences, University of California, Davis, 20 pp. [Available online at https://watershed.ucdavis.edu/files/content/news/Economic_Impact_of_the_2014_California_Water_Drought.pdf.]

Kay, J.E., Deser, C., Phillips, A., Mai, A., Hannay, C., Strand, G., Arblaster, J.M., Bates, S.C., Danabasoglu, G., Edwards, J. and Holland, M., (2015). The Community Earth System Model (CESM) large ensemble project: A community resource for studying climate change in the presence of internal climate variability. Bulletin of the American Meteorological Society, 96(8), 1333-1349, https://doi.org/10.1175/BAMS-D-13-00255.1.

Mann, E. M. and Gleick, P. H. (2015), Climate change and California drought in the 21st century, PNAS, 112, 3858-3859, doi: 10.1073/pnas.1503667112.

Meehl, G. A. et al. Global Climate Projections. In: Climate Change 2007: The Physical Science Basis. Contribution of Working Group I to the Fourth Assessment Report of the Intergovernmental Panel on Climate Change. (Cambridge University Press, 2007).

Otkin, J.A., Anderson, M.C., Hain, C., Svoboda, M., Johnson, D., Mueller, R., Tadesse, T., Wardlow, B. and Brown, J., (2016). Assessing the evolution of soil moisture and vegetation conditions during the 2012 United States flash drought. Agricultural and Forest Meteorology, 218, 230-242, https://doi.org/10.1016/j.agrformet.2015.12.065.

Saft, M., A. W. Western, L. Zhang, M. C. Peel, and N. J. Potter (2015), The influence of multiyear drought on the annual rainfall-runoff relationship: An Australian perspective, Water Resour. Res., 51, 2444–2463, doi:10.1002/2014WR015348.

Seidel, D. J., Fu, Q., Randel, W. J. and Reichler, T. J. (2008). Widening of the tropical belt in a changing climate. Nature Geosci. 1, 21–24, doi:10.1038/ngeo.2007.38.

Seager, R., Ting, M., Li, C., Naik, N., Cook, B., Nakamura, J. (2013). Projections of declining surface-water availability for the southwestern United States. Nature Clim.

Change 3, 482–486, doi: 10.1038/nclimate1787.

Sheffield, J., Wood, E.F. and Roderick, M.L., (2012). Little change in global drought over the past 60 years. Nature, 491(7424), 435-438, doi:10.1038/nature11575.

Trenberth, K.E., Dai, A., Van Der Schrier, G., Jones, P.D., Barichivich, J., Briffa, K.R. and Sheffield, J., (2014). Global warming and changes in drought. Nature Climate Change, 4(1), 17-22, doi:10.1038/nclimate2067.

Wang, S.-Y., L. Hipps, R. R. Gillies, and J.-H. Yoon. (2014) Probable causes of the abnormal ridge accompanying the 2013–2014 California drought: ENSO precursor and anthropogenic warming footprint. Geophys. Res. Lett., 41. 3220–3226, doi:10.1002/2014GL059748.

Wilhite, D.A. and M.H. Glantz. (1985) Understanding the Drought Phenomenon: The Role of Definitions. Water International 10(3):111–120

Chapter 4 Conclusion

4.1. Chapter 1: Understanding influences of convective transport and removal processes on aerosol vertical distribution

In order to improve our understanding of the important factors controlling the vertical aerosol profile, I investigate the relationships between CMF, precipitation, average extinction coefficient in lower and upper troposphere, and aerosol vertical dispersivity using seven years of monthly observational and reanalysis data. The results show that more CMF is significantly associated with more precipitation. In the tropics, more CMF/precipitation is also related to less aerosol in the lower troposphere, more aerosol above 500 hPa, and thus, enhanced aerosol vertical dispersivity.

Over the NH mid-latitude oceans, the relationships reverse—CMF and precipitation are negatively correlated with aerosol vertical dispersivity. However, when I investigate CMF/precipitation over the upwind emission sources (e.g., SE Asia), I recover the positive correlations with dispersivity over the NH mid-latitude oceans. In addition, I find that downward CMF over the NH mid-latitude oceans is important in controlling the aerosol vertical dispersivity, by transporting the relatively large amount of aerosol that has already been lofted to lower altitudes.

A key finding of this study is that convective mass flux is an important mechanism that influences the vertical distribution of aerosols. More CMF is associated with enhanced vertical dispersivity, including less aerosols below 500 hPa, but more aerosol aloft. These results highlight the need for further work, including assessment of

modeled vertical aerosol distributions and their ability to capture the observed relationships between CMF, precipitation, and the aerosol vertical dispersivity.

4.2 Chapter 2: A likely increase in fine particulate matter and premature mortality under future climate change

I assess how business-as-usual GHG-induced climate change influences $PM_{2.5}$ concentration at the end of the 21st century using seven models, including five ACCMIP models and in-house simulations with CAM4/5. Both lung cancer (LC) and cardiopulmonary disease (CPD) premature mortality due to future $PM_{2.5}$ concentration changes are also evaluated. The results indicate that climate change has a significant impact on surface $PM_{2.5}$ concentration. Globally, six of seven models yield an increase in annual mean $PM_{2.5,}$ with a model mean increase of 0.43 $\mu g/m^3$ (-0.25 to 1.71 $\mu g/m^3$). Furthermore, at least five of seven models yield a $PM_{2.5}$ increase in nine of ten world regions, with Africa the exception. These results are similar to those obtained by *Silva et al.* [2017], who focused on the ACCMIP models.

Consistent with the GHG-induced increase in $PM_{2.5}$, five of seven models indicate an increase in premature mortality based on LC and CPD in eight of the ten world regions (Australia and Africa the lone exceptions). Furthermore, the majority of models yield an increase in global mean premature mortality. Although the model mean global average premature mortality increases in all future-population scenarios, the magnitude varies by a factor of ~2 depending on the SSP, ranging from 143,704 deaths/year in SSP4 to 265,112 deaths/year in SSP3. This range of future premature mortality covers the

corresponding estimate of 215,000 deaths/year using projected future-population from the International Futures (IFs) integrated modeling system with four diseases [*Silva et al.,* 2017]. I also note that this increase in $PM_{2.5}$ and associated premature deaths likely represent an upper bound, since future projected decreases in aerosol emissions will counter the increase in $PM_{2.5}$ due to climate change alone [*Silva et al.,* 2016].

Although our analysis implies GHG-induced climate change is likely to yield an increase in $PM_{2.5}$ and associated premature mortality, uncertainty does exist. Much of this uncertainty is due to uncertainty in model physics and representation of aerosol processes. The model mean estimate of global premature deaths, averaged over five future population projections, is 194,448 deaths/year (-249,976 to 1,043,850 deaths/year). Thus, although future population projections contribute some uncertainty, differences in model physics lead to the large range of $PM_{2.5}$ associated premature deaths.

This study indicates that future increases in $PM_{2.5}$ due to GHG-induced warming is likely associated with human health risks, including premature mortality. Therefore, the need for strict reductions in air pollution emissions is warranted, to avoid the possible adverse health effects of elevated $PM_{2.5}$ concentration in a warmer world.

4.3 Chapter 3: Investigation of future changes in drought risk over California under a business-as-usual scenario

I investigate drought risk under 21st Century warming using 40 realizations from CESM-LENS, which simulates the observed relationship between CA precipitation and El-Nino. Moreover, five hydrological parameters are investigated, including

precipitation, surface water availability (P-E: precipitation minus evaporation), runoff and shallow/deep soil moisture. The results indicate a positive annual ensemble mean trend in each parameter. A stronger positive trend in precipitation, P-E and runoff over northern and central CA occurs, relative to that over southern CA. For soil moisture, a weak (strong) positive trend in the ensemble annual mean occurs for shallow (deep) soil moisture.

The majority of components, including, precipitation, runoff and deep soil moisture in the 21st century (2050-2099) indicate decreasing drought risk relative to 20 century (1950-1999), at 4.2, 0.8 and 1.5%, respectively. In contrast, a large increase in drought risk occurs in shallow soil moisture, at 12.2%. Moreover, surface water availability also indicates an increase in drought risk at 2.6%. Increases in temperature and evaporative demand in warmer world results in increase in evaporation, which yield less surface water, particularly in the upper soil layer. However, increasing precipitation and runoff leads to increases in deep soil moisture [*Cheng et al*., 2016], implying more water for plants and crops. These results suggest that drought risk in the 21st century is similar to that in the 20th century, in particular agricultural drought. Moreover, warming in the future may not lead to a significant increase in drought risk for California.

This study contains limitations because only one model is used to assess drought risk. Using a single model may yield significant uncertainty. Different models carry various physics, dynamical cores, land surface models, and resolution. Moreover, there are other factors that may be important for future CA drought risk. Atmospheric rivers, for instance, are phenomenon associated with high moisture transport, and are

responsible for 30-50% of all precipitation on the US West Coast [*Laver and Villarini.* 2013; *Dettinger.* 2013]. Hence, in future work, multiple models are required to evaluate drought risk with less uncertainty using diverse variables.

References

Dettinger, M.D., (2013). Atmospheric rivers as drought busters on the US West Coast. Journal of Hydrometeorology, 14(6), 1721-1732.

Lavers, D.A. and Villarini, G., (2013). Atmospheric rivers and flooding over the central United States. Journal of Climate, 26(20), 7829-7836.

Silva, R. A. *et al.,* (2016), The effect of future ambient air pollution on human premature mortality to 2100 using output from the ACCMIP model ensemble. *Atmos. Chem. Phys. Discuss*. 2016, 1-24. doi:10.5194/acp-16-9847-2016.

Silva, R. A., *et al.,* (2017), Future global mortality from changes in air pollution attributable to climate change. *Nature Climate Change.* doi:10.1038/NCLIMATE3354.

Chapter 5 Future Work

I have investigated how convective mass flux and precipitation are related to the aerosol vertical profile using observational and reanalysis datasets [*Park and Allen,* 2015]. Continuing from the Chapter 1 work, I will assess how atmospheric transport and removal processes are associated with the vertical aerosol distributions in General Circulation Models (GCMs), and determine of the models can reproduce the observed relationships between CMF and aerosol dispersivity. In addition, the sensitivity of simulated vertical aerosol profiles to vertical resolution and geophysical processes, including convective transport and wet removal, will be evaluated.

Previous studies show significant differences between observed and modeled vertical aerosol profiles, with models generally placing too much aerosol in the upper troposphere [e.g., *Koch et al.,* 2009; *Koffi et al.,* 2012]. *Allen and Landyut.* [2014] showed Coupled Model Intercomparison Project 5 (CMIP5; *Taylor et al.,* 2012) overestimate BC as compared to HIAPER Pole-to-Pole Observation (HIPPO), particularly in the tropics (20S-20N). *Koffi et al.* [2012] also found that several models overestimate the extinction coefficient in the upper troposphere compared to observations over industrial and maritime regions. On the other hand, model simulations underestimated the extinction coefficient over African and Chinese dust source regions.

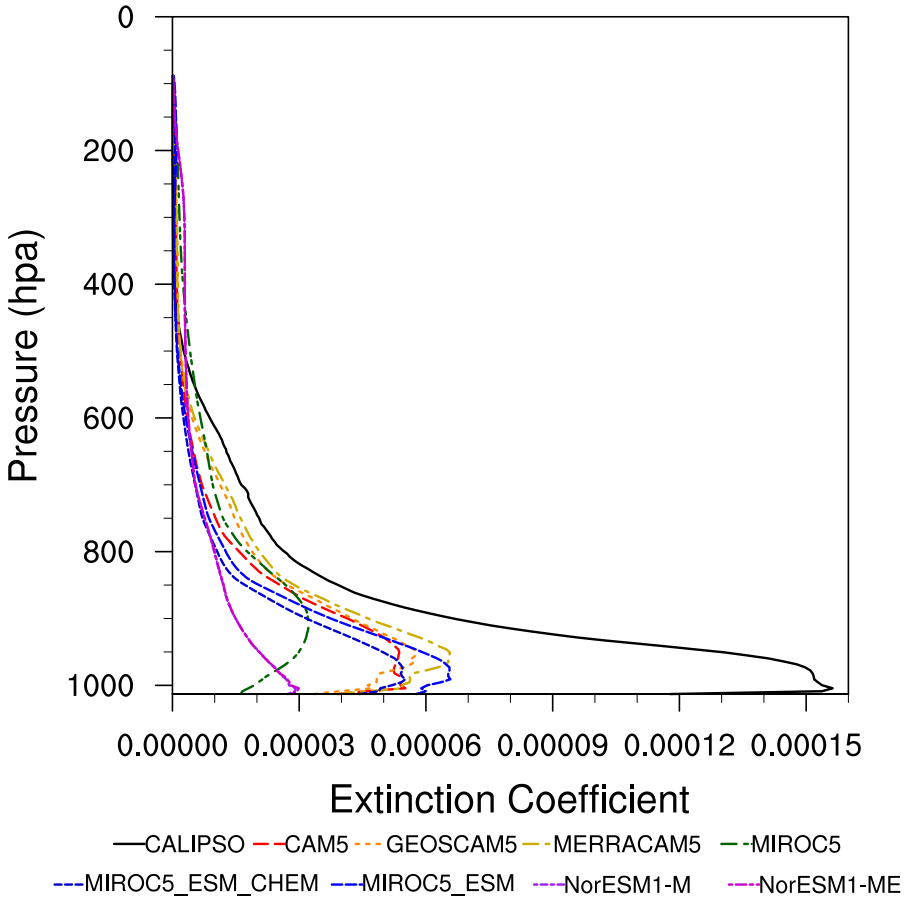

Figure 5.1 Global mean vertical profiles of extinction coefficient from CALIPSO (black) versus eight GCMs. GCMs include CAM5 (dashed red), GEOSCAM5 (dashed yellow), MERRACAM5 (dashed orange), MIROC5 (dashed green), MIROC5_ESM_CHEM (dashed dark blue), MIROC5_ESM (dashed blue), NorESM1-M (dashed purple), and NorESM1-ME (dashed pink).

Figure 5.1 shows a comparison of the vertical profile of global mean extinction coefficient from eight GCMs and the Cloud-Aerosol Lidar Infrared Pathfinder Satellite Observation (CALIPSO). All three models significantly underestimate extinction coefficient in the lower troposphere and overestimate in the upper troposphere. Relative to CALIPSO, models underestimate aerosol extinction below 500 hPa by 2-11%, but overestimate aerosol extinction by 3-14% above 500 hPa. Moreover, among models, the vertical aerosol profile exhibits large variations over the same region. The uncertainties of modeled vertical profiles are associated with aerosol sources and diverse processes, including wet and dry removal, and convective transport [*Allen and Landuyt.* 2014, *Ban-Weiss et al.,* 2012, *Vignati et al.,* 2010].

Allen and Landyut. [2014] shows that CMIP5 models exhibit a strong correlation between black carbon (BC) burden and wet deposition. Models with more global annual mean wet deposition are associated with less BC burden, with a significant anti-correlation of -0.74 in the year 2010. Total BC removal is dominated by wet deposition, which comprises 75% of the total removal. Moreover, BC burden spans a large range (from 100 Gg to 300 Gg), which is related to model differences in the rate of wet removal.

Their results also show that over half of the inter-model spread of BC above 500hPa is accounted for by model differences in convective mass flux (MC) above 500hPa. Models with more convective mass flux above 500 hPa are associated with more BC aloft, and vice versa. This also implies that the large range in simulated BC aloft may be due to the large range in convection aloft, which ranges from ~20 to 100 kg/m^2/day in

CMIP5 models. Model-specific year-to-year variations in BC and convective mass flux aloft are also significantly correlated in most CMIP5 models, with CAM5 yielding a corresponding correlation of 0.61.

Furthermore, compared to NASA's Modern-Era Retrospective Analysis for Research and Applications [MERRA; *Rienecker et al.,* 2011], nearly all CMIP5 models overestimate global annual mean convective mass flux, with CAM5 yielding the worst overestimation (by nearly a factor of 3). This implies models may overestimate BC aloft—and perhaps other aerosols—due to excessive convective mass flux. Excessive MC may also lead to more wet removal by enhanced convective precipitation, which may also help to account for model underestimation of aerosols in the lower troposphere.

To improve our understanding of the aerosol vertical profile and its influence on radiative forcing, global climate model simulations need to be evaluated by observational data, and model shortcomings identified by idealized experiments. The CMIP5 models represent the latest advancements in GCM development and are an important component of the Intergovernmental Panel on Climate Change's (IPCC) assessment of climate science. In particular, these models are used to estimate future climate change. Therefore, it is important to assess their simulation of the vertical aerosol profile and to look at those relationships in observations to assess model simulations.

I have three principal research tasks related to this research. I will use simulated aerosol vertical profile from CMIP5 models and compare them to CALIPSO to identify possible model versus observation discrepancies. I will perform sensitivity experiments with CMIP5 models to investigate the role of convection and wet removal in the

simulated vertical aerosol distributions. In addition, land/sea contrasts and regional (tropical versus extratropical) variations in the relationships between convective mass flux, precipitation and aerosol vertical dispersivity will be evaluated. For the last step, I will evaluate the sensitivity of aerosol aloft to convective mass flux in models versus observations.

References

Allen, R. J., and W. Landuyt. (2014), The vertical distribution of black carbon in CMIP5 models: Comparison to observations and the importance of convective transport, J. Geophys. Res. Atmos., 119, 4808–4835, doi:10.1002/2014JD021595.

Ban-Weiss, G. A., Cao, L., Bala, G., and Caldeira, K. (2012), Dependence of climate forcing and response on the altitude of black carbon aerosols. Clim. Dyn. 38, 897-911, doi: 10.1007/s00382-011-1052-y.

Koch, D., Schulz, M., Kinne, S., et al. (2009), Evaluation of black carbon estimations in global aerosol models, Atmos. Chem. Phys., 9, 9001-9026, doi:10.5194/acp-9-9001-2009.

Koffi, B., Schulz, M., Breon, F.-M., et al. (2012), Application of the CALIOP layer product to evaluate the vertical distribution of aerosols estimated by global models: AeroCom phase I results. J. Geophys. Res, 117, D10201, doi: 10.1029/2011JD016858.

Park, S., and Allen, R. J. (2015), Understanding influences of convective transport and removal processes on aerosol vertical distribution. Geophys. Res. Lett. 42, 10,438-10,444. doi: doi:10.1002/2015GL066175.

Rienecker, M. M., Suarez, M. J., Gelaro, R., et al. (2011), MERRA: NASA's Modern-Era Retrospective Analysis for Research and Applications. J. Climate, 24, 3624–3648, doi: http://dx.doi.org/10.1175/JCLI-D-11-00015.1.

Taylor, K. E., Stouffer, R. J., and Meehl, G. A. (2012), An Overview of CMIP5 and the Experiment Design. Bull. Amer. Meteor. Soc., 93, 485–498, doi: http://dx.doi.org/10.1175/BAMS-D-11-00094.1.

Vignati, E., Karl, M., Krol, M., et al. (2010), Sources of uncertainties in modelling black carbon at the global scale. Atmos. Chem. Phys., 10, 2595-2611, doi:10.5194/acp-10-2595-2010.